Dissertation
zur Erlangung des Doktorgrades der Naturwissenschaften
(Dr. rer. nat.) der Fakultät für Physik der Universität
Regensburg

Thermal Transport across Atomic and Molecular Junctions

vorgelegt von
Nico Mosso

2018

Promotionsgesuch eingereicht am 28. Mai 2018.
Die Arbeit wurde angeleitet von
Dr. Bernd Gotsmann und Prof. Dr. Jascha Repp.

Prüfungsausschuss
Vorsitzender: Prof. Dr. Tilo Wettig
1. Gutachter: Prof. Dr. Jascha Repp
2. Gutachter: Prof. Dr. Christoph Strunk
Weiterer Prüfer: PD. Dr. Andreas Hüttel

Termin Promotionskolloquium: 26. Oktober 2018

When you can measure what you are speaking about... you know something about it.

- Lord Kelvin, 1883

Table of Contents

Chapter 1

Introduction

Heat dissipation has been widely recognized as one of the main limiting factors of the performances of nanoscale electronics devices [1, 2]. Apart from these challenges, engineering the thermal transport properties of materials is highly desirable for thermoelectric, cooling [3] and more in general thermal management applications. Heat transport in molecular junctions is very rich in terms of physics phenomena and offers novel opportunities by tailoring the chemical structure to obtain the desired properties. For instance an experimental study performed recently in our group showed that the length dependence of the thermal conductance of short alkane chains (from 2 to 18 carbon atoms) does not follow either pure ballistic or diffusive transport exhibiting a non-monotonic behavior with a maximum at 4 carbon atoms [4]. This trend may result from a combination between the number of modes available in the molecule (which might change significantly with length especially for short molecules) and the degree of localization of some of the vibrational modes [5, 6]. The concept of localization (which can be thought as the extension of a mode on the molecule) and its effects on transport has still been largely unexplored.

Another interesting concept that was proposed recently is based on phonon quantum interference [7]. Attaching side chains with different lengths to the molecular backbone forming a sort of ”Christmas tree” structure was suggested as a strategy to reduce the phonon contribution to thermal conductance. Indeed, the interaction of such side chains with the molecule, generates Fano-like resonances in the phonon transmission function of the molecular junction, depleting the number of modes available for transport. By tuning the length of the side groups, it is then possible to change the frequency of the Fano resonance. The interplay between the phonon density of states in the electrodes, the coupling to the molecule, the molecular vibrational spectra, the degree of localization offer a wide range of tunability that needs to be systematically investigated.

The measurement of heat conduction in molecular junctions has remained elusive, mainly because of the lack of suitable experimental techniques. Measuring thermal resistances is in many ways more challenging than the electrical counterpart from the experimental point of view. The main reason lies in the fact that the range of thermal conductivities of available materials spans over only 6 orders of magnitudes, compared to more than 26 for electrical conductivity. This means, that the only good thermal insulator is vacuum, if one neglects the contribution of radiation and that simple techniques like the electrical 4-probe measurement of resistance are not possible in thermal transport.

The experimental investigation of the thermal properties of molecular systems has been focused on self assembled monolayers (SAMs) of alkane chains, because of their property of assembling in high quality films. Typical techniques include optical pump/probe methods like Time Domain Thermoreflectance (TDTR) [8] and Frequency Domain Thermoreflectance (FDTR) [9], Scanning Thermal Microscopy (SThM) [4] and 3-ω resistance measurement [10]. All of these methods require the formation of SAMs of good quality in order to avoid measurement artifacts and compare with the theoretical predictions. Even for the case of alkane-dithiols on gold surfaces (which is probably the most understood system in terms of assembly properties [11]), big uncertainties in the number of investigated molecules during the experiment remain, because of the surface roughness of the electrodes, defects in the SAMs etc. Moreover, the choice of molecules forming nice films on surfaces is quite small, limiting the range of phenomena that can be studied with these approaches.

For these reasons, we developed a novel experimental technique based on single molecule measurements that, similar to what has been done for charge transport, can provide a better route to explore the structure-property relationship in these systems and understand the basic concepts underlying phonon transport at the molecular and atomic scale.

Even if experimental data have been lacking so far, numerous theoretical studies have been published, predicting effects from quantum phonon interference [12, 7] to thermal rectification [13] and high thermoelectric conversion efficiencies [14], which need verification. Experimental data is needed also to verify the underlying assumptions of the models used for transport. The theoretical problem of heat transfer in molecular junctions presents many challenges related to the many-body interactions and quantum effects occurring in an intrinsic non-equilibrium situation [6]. Common theoretical frameworks include classical Molecular Dynamics (MD) and quantum ab-initio methods based on Equilibrium or Non-Equilibrium Green's Function approach. In the linear regime (small ΔT), harmonic approximation of the force fields is typically assumed and phonon transport is described within the single particle picture of ballistic and elastic phonon transport. Many questions about the type of transport regime, the role of many-body interactions, the conditions to obtain thermal rectifications or transport beyond the linear regime still remain open. With the technique developed in this work, we would like to provide further insights into these research questions and to spur new theoretical investigations to support for instance unexpected experimental data.

As the title suggests, this thesis presents the measurement of the thermal transport properties of atomic and molecular junctions, from development of the experimental setup and methods to the results.

1.1 Outline

This thesis is organized in 4 main chapters. In chapter 2, we briefly review the theoretical background to support the experimental data and the conclusions drawn from them. In particular, we discuss charge transport in metallic atomic contacts and molecular junctions, presenting as well the experimental break junction technique employed in this thesis to measure the electrical conductance of these systems. We turn to with thermal and thermoelectric properties of electrons in the Landauer formalism. Finally, we introduce phonon transport in molecular junctions.

In chapter 3, we present the experimental setup and technique developed during this PhD project, starting from the working principle to the description of the setup and measurement method. We then describe in detail the Micro Electro Mechanical Systems at the heart of the measurement technique, which have been used to measure the thermal conductance of atomic and molecular junctions. Finally, the procedure to clean and functionalize the MEMS surface and the tip preparation is described.

Chapter 4 describes the measurements of heat transport across atomic contacts, from the main results to the details of the experiments and variants with respect to the basic system of gold-gold junctions.

In chapter 5, we show the results obtained for heat transport in single molecule junctions. In particular, we start from the development of the experimental method and we then discussed the measurements on the thermal conductance of two model systems in molecular electronics, namely dithiol-oligo(phenylene ethynylene) (OPE3) and octane dithiol (ODT).

The final chapter includes a summary of the main measurements results and an outlook for future works.

Chapter 2

Background

In this chapter, the theoretical principles related to charge and phonon transport in atomic and molecular junctions are presented. First, charge transport in atomically sized metal-metal contacts and molecular junctions is explained, in connection to the break-junction technique. Then phonon transport in these nanoscopic systems is described within the Landauer formalism, presenting the concepts of thermal conductance quantization and phonon transmission.

2.1 Charge Transport

According to the system size, different charge transport regimes take place. In a macroscopic conductor, the electrical conductance can be calculated from the well-known Ohm's law and it is linked to its physical properties through the relation:

$$G = \sigma \cdot \frac{A}{L} \tag{2.1}$$

where A represents the cross-section area of the conductor perpendicular to the current direction, L the conductor length parallel to the current direction and σ its conductivity, dependent only on the material properties. This formula assumes diffusive transport and is valid when the current density inside the conductor is homogeneous. When the sizes of the conductor shrunk below certain limits, Ohm's law is no longer valid, and the wave-character of electrons can come into play.

To discriminate between the different conduction regimes, three main characteristic lengths can be identified:

1. Electron mean free path λ_m: average distance which an electron travels before losing its initial momentum. In most cases, it measures the distance between two successive scattering events.

2. Phase coherence length λ_ϕ: average distance in which the electron preserves its initial phase and comes into play in electron interference phenomena.

3. Fermi wavelength λ_F: De Broglie wavelength of the electrons at the Fermi energy, namely the electrons participating to the conduction.

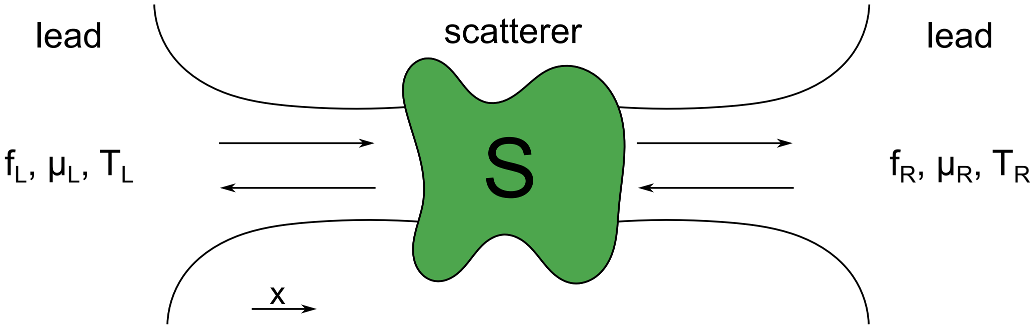

Figure 2.1: Schematic of the Landauer scattering approach. The leads represent two electron reservoirs connected by a 1D conductor, in which a scatterer (S) has been inserted. Transport across the system is ballistic and electrons can be elastically scattered at S. f indicates the Fermi distribution, μ = chemical potential and T the temperature of the leads.

The relation connecting the Fermi wavelength λ_F to the Fermi energy E_F for an electron in crystalline solids is:

$$\lambda_F = \frac{h}{\sqrt{2m^* E_F}} \tag{2.2}$$

where h is the Planck constant and m^* is the effective mass of the electron. Both E_F and m^* are parameters characteristic of the material. If the size of the system is lower than the electron mean free path, charge transport is ballistic. Moreover, if one of system's dimensions is comparable to the Fermi wavelength λ_F, confinement effects take place. Atomic junctions are quantum one dimensional ballistic systems as the typical transversal size of about few atoms is on the order of the Fermi wavelength of the electrodes ($\lambda_F \sim 0.5$ nm in metals [15]) and the length (up to few nm) is well below the electron mean free path (10-100 nm) at room temperature [15, 16]. In this regime, charge transport is usually described within the Landauer-Büttiker formalism, introduced in 1957 [17], which connects the electrical properties of a mesoscopic conductor with the quantum mechanical transmission and reflection probabilities of the propagation modes (electron wavefunctions). Let's consider a 1D ballistic channel, connected to macroscopic leads acting as electron reservoirs, that contains a scatterer S, Figure 2.1. Since the electrons are transversally confined in the conductor, the associated energy spectrum is quantized. The corresponding dispersion relation is:

$$E_n(k_x) = \epsilon_n + \frac{\hbar^2 k_x^2}{2m^*} \tag{2.3}$$

where $\hbar$ is the reduced Planck constant, m^* the effective mass of the electron and the integer n accounts for the mode number. This means that in the reciprocal space, several parabolic sub-bands are formed, with vertices placed respectively at ϵ_n for integer values of n. The corresponding electron wave-functions Ψ_n are constituted by the product of a propagating plane-wave in the x-direction times a transverse wave-function $\chi_n(y,z)$, calculated by solving the Shcrödinger equation in the confining potential introduced by the 1D wire:

$$\Psi_n \propto \mathrm{e}^{\pm i k_x x} \chi_n(y,z) \tag{2.4}$$

In other words, these are the only propagating modes that can travel into the 1D conductor, namely the only conduction channels available. Depending on the position of the Fermi energy[1], one or more sub-bands can be filled with electrons. The number of accessible sub-bands is equivalent to the number of conduction channel at disposal.

If a positive voltage is applied to the right reservoir (with $\mathrm{T_L} = \mathrm{T_R}$), the electrons from the left contact will be attracted to the right one, since $\mu_R < \mu_L$. The current contribution I, for one conductive channel, can be written as:

$$I = -\frac{e}{\pi} \int_{-\infty}^{+\infty} \tau(k)\rho(k)v(k)(f(E_k, \mu_L) - f(E_k, \mu_R))\mathrm{d}k \tag{2.5}$$

where $\tau(k)$ is the transmission probability describing the scattering at S, $\rho(k)$ represents the density of states in 1D, $v(k)$ the velocity and $f(E_k, \mu)$ the Fermi distribution[2]. In 1D it can be demonstrated that the electron density of states is equal to:

$$\rho(E) = \frac{4}{h} \cdot \frac{1}{v(E)} \tag{2.6}$$

Therefore, by passing to the energy domain, equation 2.5 can be rewritten as:

$$I = -\frac{2e}{h} \int_{0}^{+\infty} \tau(E)(f(E, \mu_L) - f(E, \mu_R))\mathrm{d}E \tag{2.7}$$

We would like to stress that this equation is very general and typically used to simulate charge transport in both atomic and molecular junctions. Indeed, the properties of the system under study (our scatterer) are all included in the transmission function $\tau(E)$, which can be calculated with ab-initio methods based on Density Functional Theory (DFT) in combination with Green's function scattering theory or simple tight-binding models [18, 19].

Let's now assume to have a perfect 1D conductor with $\tau(\mathrm{E}) = 1$. At T = 0 K, the Fermi distribution is a step function equal to 1 for $\mathrm{E} < \mu$ and 0 for $\mathrm{E} > \mu$. Thus the difference $(f(E, \mu_L) - f(E, \mu_R))$ is equal to 1 for energy values $\mu_r < E < \mu_l$ and it is null outside this window. The integral of equation 2.7 simplifies to:

$$I = -\frac{2e}{h} \int_{\mu_R}^{\mu_L} \mathrm{d}E = -\frac{2e}{h} \cdot (\mu_L - \mu_R) \tag{2.8}$$

The chemical potential difference is linked to the voltage difference by the electron charge, i.e. $(\mu_L - \mu_R) = -e(V_R - V_L)$. The current contribution of a single channel is equal to:

$$I = \frac{2e^2}{h} \cdot (V_R - V_L) = G \cdot (V_R - V_L) \tag{2.9}$$

This shows that the conductance of a single electron channel in the ballistic regime is constant and equal to the conductance quantum $\mathrm{G_0} = \frac{2e^2}{h} \approx 77.5$ µS corresponding to a resistance quantum $\mathrm{R_0} = \frac{h}{2e^2} = 12.9$ kΩ.

---

[1] In this work, the Fermi energy will be used as synonym of chemical potential, even though this is formally true only at T = 0 K. For the purposes of the thesis, this distinction is not relevant.

[2] The difference between the Fermi distribution in the integral derives from the fact that only the net flow of electrons contributes to the current. At equilibrium there is a continuous electron flow from left to right and vice versa and the resulting current is zero. Indeed, at equilibrium $\mu_R = \mu_L$ and the difference of the Fermi distributions in the integral would be null.

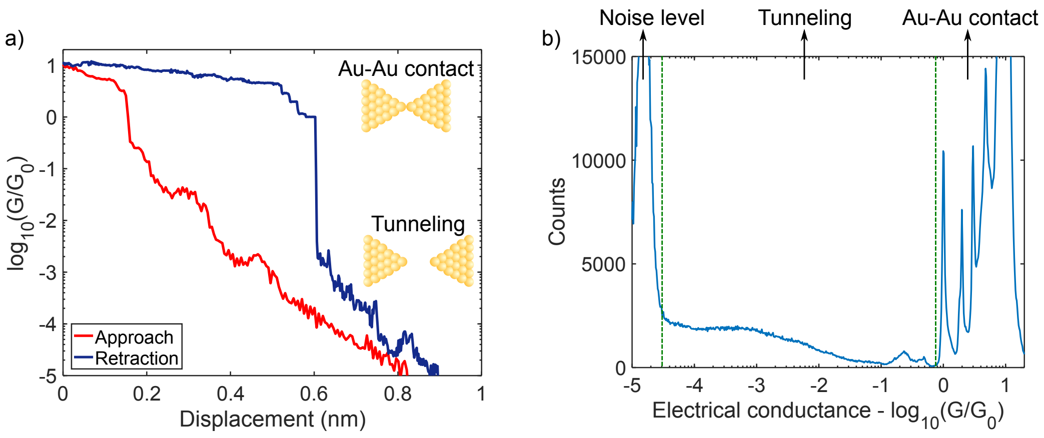

Figure 2.2: Charge transport through gold atomic contacts. a) Single opening/closing trace. b) 1D electrical histograms showing peaks at multiples of the electrical conductance quantum G_0.

If more than one channel is available, all with transmission probability equal to unity, the overall conductance will be given by adding the contributions of each channel, namely G_0:

$$G = \frac{2e^2}{h} \cdot N = N \cdot G_0 \tag{2.10}$$

where N is the number of conducting modes. Therefore, the conductance of a perfect ballistic conductor is quantized in multiples of G_0. This represents a simplified version of the Landauer-Büttiker formula, because it assumes that all the conductive channels have perfect transmission. A more general formulation is found by inserting the scatterer in the 1D conductor, i.e. by supposing that some electrons can be backscattered or lose energy:

$$G = \frac{2e^2}{h} \sum_{i,j}^{N} T_{ij} \tag{2.11}$$

where T_{ij} represents the probability that an electron passes from the i_{th} mode of the left reservoir to the j_{th} mode of the right reservoir [15].

2.1.1 Conductance Quantization in Metallic Quantum Point Contacts

Conductance quantization can be measured by controlling the number of channels available for the electrical conduction in a 1D system. This can be achieved by shifting the Fermi level E_F of the system with the help of a gate voltage, or by tuning the system size, in order to change the energy spacing between the sub-bands. Experimental demonstrations of conductance quantization have been reported on several systems from 2D electron gases in semiconductor heterostructures [20], InAs nanowires [21] and metallic quantum point contacts.

The energy splitting between the channels is linked to the Fermi wavelength by the following relation:

$$\Delta E = \frac{\pi^2 \hbar^2}{2m^* \lambda_F} \tag{2.12}$$

Since, in semiconductors λ_F can be of several tens of nanometers, the energy difference between the modes is on the order of few meV and conductance quantization is not observable at room temperature[3]. Therefore, cryogenic temperatures are usually needed to visualize the effects of quantum confinement in 2D electron gases. On the other hand, for metals λ_F is much smaller (< 1 nm) and ΔE can be of the order of 1 eV. Thus, conductance quantization can be measured also at room temperature in atom-size metallic contacts [22, 23].

Charge transport in metallic quantum point contacts has been mainly studied via the so called break junction techniques, namely Mechanically Controlled Break Junction (MCBJ) and Scanning Tunneling Microscope-Break Junction (STM-BJ) [15, 24]. The latter will be briefly introduced in this section, as one of the main building blocks of the experimental technique developed during the PhD project and described in chapter 3.

The STM-Break Junction method consists in the repeated formation and breaking of contacts between the tip of a STM microscope and a metallic surface. The electrical conductance of atom sized contacts of many different metals has been studied since the nineties with this technique [25, 22, 15], with gold being the most characterized and understood material. Also for this reason, gold was selected as the material of choice in most of the experiments reported in this work, 5 and 4.

Figure 2.2a shows a typical closing and opening trace obtained by moving the gold STM tip into contact with a gold surface while measuring the electrical current at a small fixed bias ($V \sim 100$ mV)[4]. During the approaching cycle (red curve), when the tip is few Å away from the surface, tunneling of electrons is recorded showing a typical exponential decay. For convenience, the electrical conductance has been plotted on a logarithmic scale and normalized with the conductance quantum G_0. The tip is then approached until a Au-Au contact is formed. While opening of the junction (blue curve) the electrical conductance decreases in a step-like fashion because of conductance quantization. Right before going into the tunneling regime, a plateau at 1 G_0 is typically observed, indicating the formation of a single atom contact. In fact, a single gold atom provides one electron channel for conduction with perfect transmission ($T = 1$). This phenomenon is very well established and it has been confirmed both experimentally and theoretically by several independent groups [15]. Especially at low temperature, long (> 0.3 nm) plateaus at G_0 can be measured, corresponding to the formation of monoatomic chains [26, 27]. As the dynamics of the breaking process is not under experimental control, it is common practice to build one dimensional (1D) electrical histograms of few thousands opening traces[5] to obtain statistically relevant information about the charge transport properties, as shown in Figure 2.2b. In the contact regime ($G > 1$ G_0), sharp peaks at multiples of the quantum of conductance appear, indicating the availability of an integer number of electronic channels and confirming that conductance quantization comes into play. In fact, the measurement of plateaus or peaks in the histograms may be related to the plastic stages of deformation of the atomic contacts and not to conductance quantization. In gold contacts, conductance quantization typically occurs up to 3

---

[3] At $T = 300$ K, the average thermal energy K_BT is about 26 meV, larger than the energy distance between the modes.

[4] Note that similar traces can be measured both at room and cryogenic temperatures.

[5] Closing traces are rarely used, because the high diffusivity of gold at room temperature typically hinders the formation of stable single atom contacts; typically a jump to contact is observed, as shown in Figure 2.2a.

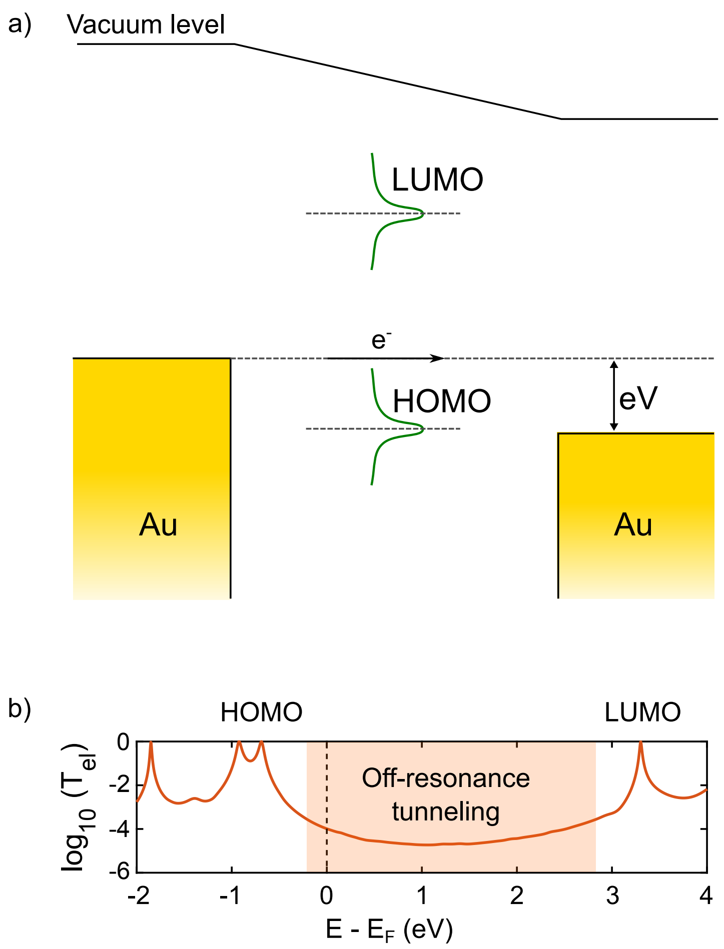

Figure 2.3: Charge transport through a single molecule. a) Energy diagram of a molecule between two metal leads, in which a positive voltage V has been applied to the right electrode. The molecular energy levels (HOMO and LUMO) are broadened because of the coupling with the metals electrodes. b) Example of electronic transmission function of HOMO dominated charge transport through a single molecule. As a common practice, the origin of the energy scale is placed at the predicted Fermi energy E_F of the junction.

G_0. At larger contact sizes, multiple channels with transmissions lower than one participate to transport, breaking the quantization regime [28].

One interesting feature of the electrical conductance of atomic contacts is that the number of available channels for transport depends on the outer chemical orbitals [29]. For instance, monovalent metals like Au exhibit a single electronic channel with perfect transmission, while 5d metals like Pt feature up to 5 channels in single atom contacts, with transmission than unity giving a total electrical conductance between 1.5 and 2 G_0 [30].

2.1.2 Molecular Junctions

Charge transport through molecular junctions has been widely studied in the past 20 years in the field of molecular electronics. In this section, we would like to briefly review the main concepts of charge transport which serves to understand the experiments presented in chapter 5. To get more insights into the topic, one can refer to the many books and reviews available in the literature [31, 32, 24, 33, 34].

An isolated molecule can be thought as a quantum dot, characterized by discrete energy levels and a certain HOMO-LUMO gap (representing respectively the Highest Occupied Molecular Orbital and the Lowest Unoccupied Molecular Orbital)[6]. When the metal-molecule-metal junction is formed, the energy levels of the molecule are broadened by the coupling with the metal electrodes, as schematically shown in Figure 2.3a. This coupling derives from the hybridization of the molecular orbitals with the continuous energy bands of the metal electrode [32]. The higher the coupling, the larger the broadening of the energy levels, and so the ability to inject charges into the molecule. Moreover, to reach the equilibrium state (constant Fermi level throughout the junction), charge transfer from the molecule to the metal electrodes or vice versa occurs, introducing a shift in the energy levels because of the additional charging energy.

The electrical conductance of the molecular junctions can be calculated from the Landauer current formula 2.7 dependent on the transmission function $\tau(\mathrm{E})$. A typical electronic transmission curve is presented in Figure 2.3b. This can be obtained with Non Equilibrium Green's Function (NEGF) methods applied to the hamiltonian of the junction, which is previously relaxed with Density Functional Theory (DFT) [18]. The peaks in the transmission are located at the energies of the molecular orbitals and their width is proportional to the coupling to the electrodes. If electrons in the contacts have energies corresponding to one of the molecular orbitals, then resonant tunneling takes place with $\tau = 1$. This condition is hard to achieve in experiments without electrical gating of the molecular junction. Typically, the Fermi energy of the system lies in the HOMO-LUMO gap and off-resonant elastic tunneling is the main transport mechanism in short molecules ($<$ 3 nm). For longer molecular chains instead, the tunneling contribution becomes negligible and inelastic hopping, in which electron transport is mediated via thermal vibrations, takes over [35].

As one can see from the transmission function in Figure 2.3b, the position of the Fermi energy determines the charge transport properties of the molecular junction. In fact, in the case T = 0 K, from equation 2.7 we can calculate the electrical conductance

$$G = \frac{2e^2}{h}\tau(E_F) \tag{2.13}$$

where $\tau(E_F)$ represents the value of the transmission function at the Fermi energy. This stems from the fact that at T = 0 K and at small voltages the difference between the Fermi distributions of the leads can be approximated as a delta function. However, the position of the Fermi energy in the junction is typically unknown and cannot be precisely predicted with DFT methods. This results in general in bad agreement between theory and experiments on the exact value of the electrical conductance of the molecule and it is a well-known limitation of DFT. Moreover, good agreement is usually achieved in the inter-comparison between similar molecular systems. Finally, we would like to point out that the anchoring group of the molecule (atomic group binding to the metal electrodes) usually determines if the junction is HOMO or LUMO conducting ($\mathrm{E_F}$ closer to the HOMO

---

[6] The HOMO can be thought as the maximum of the valence band and the LUMO as the minimum of the conduction band of an equivalent semiconductor.

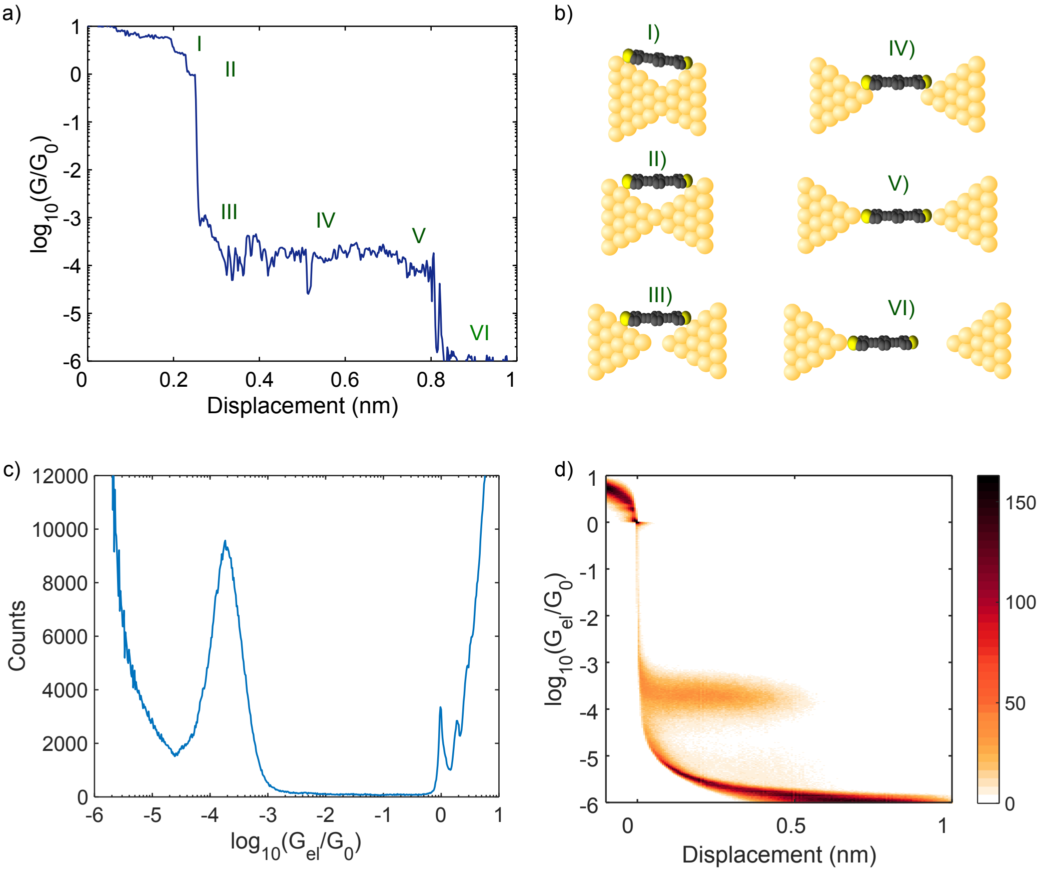

Figure 2.4: Charge transport through a single molecule with the BJ technique. a) Example of single opening trace, showing a conductance plateau at about 10^-4 G_0, indicating the formation of a molecular junction. b) Elongation stages of a molecular junctions. c) 1D electrical histogram built with 5000 traces showing a clear molecular peak at $2{\times}10^{-4}$ G_0. d) 2D histogram of the electrical versus distance curves, showing that most of the opening traces exhibit molecular conductance plateaus of about 0.5 nm in the conductance region between 10^{-3} and 10^{-4} G_0.

or LUMO respectively). For instance S based binding groups generally show a HOMO conducting character, corresponding to hole transport, while pyridine anchors are LUMO conducting [36, 37]. As we shall see, this determines the sign of the Seebeck coefficient of the molecular junction.

Break-Junction technique

Similar to what described for the case of gold atomic contacts in 2.1.1, charge transport in single molecule junctions has been largely studied with break-junction techniques [24]. The main advantage of this technique is that experimentally is relatively simple (in case of STM-BJ, it basically only requires a piezoelectric scanner to move the tip perpendicularly to the substrate) and it can be adapted to almost any environment from solvents [38] to UHV at cryogenic temperatures [39].

In a typical STM-BJ measurement, molecules are deposited on a metallic surface (usually gold) to form a sparse monolayer. The STM tip is then used to form and break metallic contacts with the substrate repeatedly to collect statistics. While opening the metallic junction decorated with molecules, there is a certain probability that tunneling through the molecule is measured, giving a very different signature with respect to tunneling through the empty gap. Figure 2.4a-b show a typical opening trace of the electrical conductance versus tip displacement exhibiting a plateau in correspondence to the sliding motion of the molecule in between the two gold electrodes [40]. After collecting few thousands opening traces, 1D electrical histograms can be built to extract the most probable conductance of the molecule as indicated by the peak at $\mathrm{G} < 1\ \mathrm{G}_0$, Figure 2.4c. Note that in the case of bare Au-Au junctions, the histogram shown in Figure 2.2b did not show any particular feature in the tunneling regime[7]. Another important tool, is the 2D histogram of the electrical conductance versus displacement, Figure 2.4d. To build this graphs, every opening trace is rescaled according to the breaking point of the Au-Au contacts (end of the $1\ \mathrm{G}_0$ plateau), so that traces with different lengths can be analyzed. Therefore, the Au-Au contact and molecular regimes will appear at respectively negative and positive displacements. The results plotted in the 2D histograms are generally more robust against unexpected variations of the tip-surface contact. In fact, peaks in the 1D electrical histograms can also arise from contaminated opening traces (continuous traces showing long range instabilities), which could hide the characteristic signature of the molecule. Typically, the size of the accumulation region in the 2D histogram is proportional to the length of the molecule, but usually shorter because of the so called snap-back of the electrodes (plastic relaxation of the tip-shaped electrodes after breaking the Au-Au contact).

2.1.3 Electronic thermal transport and thermoelectric effects

The electronic contribution to the thermal conductance in atomic and molecular junctions can also be described within the Landauer formalism [18]. In particular, if a temperature difference $\Delta\mathrm{T}$ is imposed to the leads ($\mathrm{T_L} > \mathrm{T_R}$ in Figure 2.1), thermal transport and thermoelectric effects come into play. In the linear regime, the current I and heat flux $\dot{Q}$ are related to the temperature difference $\Delta\mathrm{T}$ and the voltage difference $\Delta\mathrm{V}$ by the following relation [41, 42]:

$$\begin{pmatrix} I \\ \dot{Q} \end{pmatrix} = \begin{pmatrix} G & L \\ M & K \end{pmatrix} \begin{pmatrix} \Delta V \\ \Delta T \end{pmatrix} \tag{2.14}$$

One can then define the Seebeck coefficient S as

$$S = \left(\frac{\Delta V}{\Delta T}\right)_{I=0} = -L/G \tag{2.15}$$

and the thermal conductance k

$$k = -\left(\frac{\dot{Q}}{\Delta T}\right)_{I=0} = -K - S^2 G T \tag{2.16}$$

where the minus sign in the definition of the thermal conductance takes into account the heat flux direction. Within the Landauer-Büttiker formalism, these coefficients depend on the transmission function $\tau(E)$ in the form:

---

[7] As the histograms are built with logarithmically sized bins, one expects a flat distribution for pure exponential tunneling decay

$$G = -\frac{2e^2}{h}\int_0^{+\infty} \mathrm{d}E \frac{\partial f}{\partial E}\tau(E) \tag{2.17}$$

$$L = -\frac{2e^2}{h}\frac{k_B}{e}\int_0^{+\infty} \mathrm{d}E \frac{\partial f}{\partial E}\tau(E)(E - E_F)/k_B T \tag{2.18}$$

$$\frac{K}{T} = \frac{2e^2}{h}\left(\frac{k_B}{e}\right)^2\int_0^{+\infty} \mathrm{d}E \frac{\partial f}{\partial E}\tau(E)[(E - E_F)/k_B T]^2 \tag{2.19}$$

where k_B is the Boltzmann constant. These integrals can be simplified with the Sommerfeld expansion if the transmission function $\tau(E)$ varies slowly on the scale of $k_B T$ around the Fermi energy E_F. In this case one finds

$$K \approx -\frac{2e^2}{h} T L_0 \tau(E_F) \tag{2.20}$$

and

$$G \approx \frac{2e^2}{h}\tau(E_F) \tag{2.21}$$

where T is the temperature of the system and $L_0 = \left(\frac{k_B}{e}\right)\frac{\pi^2}{3} = 2.44\ \mathrm{V}^2/\mathrm{K}^2$ the Lorenz number. Therefore, if $S^2 << L_0$ the electronic thermal conductance is proportional to the electrical conductance via the Wiedemann-Franz law

$$k \approx L_0 T G \tag{2.22}$$

Finally, the Seebeck coefficient S is proportional to the slope of the transmission function τ(E) with the relation

$$S \approx -L_0 e T \left(\frac{\mathrm{d}\ \ln\tau(E)}{\mathrm{d}E}\right) \tag{2.23}$$

From these equations, we can expect that in metallic contact, the electronic contribution to the thermal conductance will be proportional to the electrical conductance, since the transmission function τ(E) is usually flat for a wide energy range around E_F. This however does not take into account the phonon contribution, which in the case of coherent ballistic transport may increase its relative weight compared to the bulk metal. In the case of molecular junctions, we can expect the validity of the Wiedemann-Franz law, only if the Fermi energy sits far from resonances.

2.2 Phonon Transport

Thermal transport across molecular junctions is typically dominated by phonons because of their poor thermal conductance. To date, because of the lack of suitable experimental techniques, the heat transport properties of organic molecules have been mostly studied theoretically. The few experimental studies available have been focused on the properties of self assembled monolayers (SAMs) of alkane chains, because of the need of forming high quality films. A comparison between the theoretical results obtained with Molecular Dynamics (MD) simulations and ab-initio methods and the experimental results on SAMs is provided in section 5.5.

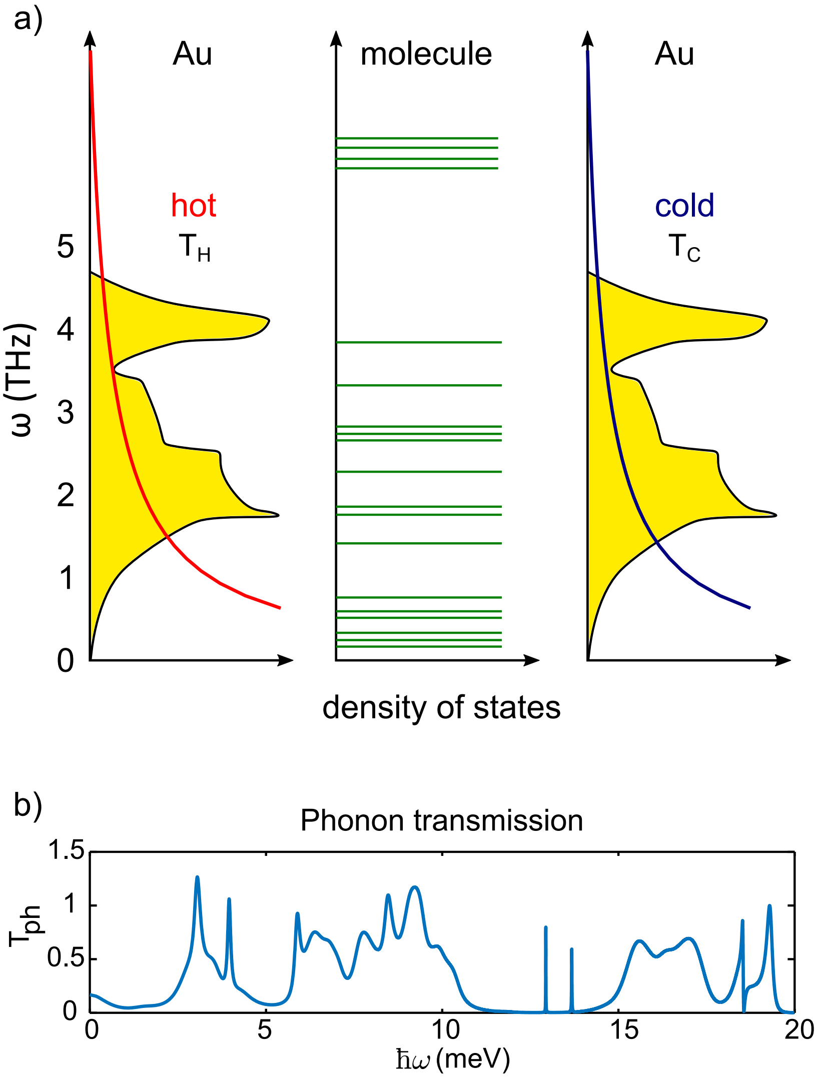

Figure 2.5: Phonon transport through a single molecule. a) Schematic diagram of the vibrational modes of a molecule in between two gold electrodes at different temperatures, characterized by their respective phonon density of states and Bose-Einstein distribution at temperature $\mathrm{T_{L,R}}$. b) Phononic transmission function. The energy is cut off at about 20 meV, in correspondence with the Debye frequency of the gold electrodes.

The discussion about the phonon contribution to the thermal conductance of gold atomic contacts can be found in section 4.1.1. Here, we would like to outline the main features of phonon transport across single molecule junctions within the Landauer formalism.

Figure 2.5 depicts the transport model for a molecule in contact with two electrodes at different temperatures. The thermal conductance k_{ph} of this junction can be expressed with a Landauer-type of formula

$$k_{ph}(T) = \frac{1}{2\pi}\int_0^\infty \hbar\omega\tau_{ph}(\omega)\,\frac{\partial f_{BE}(\omega,T)}{\partial T}d\omega \tag{2.24}$$

where $f_{BE}(\omega, T) = \left(e^{\hbar\omega/k_BT} - 1\right)^{-1}$ is Bose–Einstein distribution function, $\hbar$ is reduced Planck's constant, k_B is Boltzmann's constant and $\tau_{ph}(\omega)$ is the generalized phonon transmission function, containing also the coupling to the leads and the density of states of the leads. In analogy with the charge transport model presented above, the molecular junction can be viewed as a scatterer that filters the vibrational modes of the leads. The main difference from electron transport is set by the Bose-Einstein statistics: transport properties are not determined by the position of the Fermi energy (which does not exist for bosons), but all the occupied modes in the energy spectrum participate to transport and have to be considered in the calculation of the thermal conductance. Figure 2.5b shows an example of phonon transmission for a molecule between gold electrodes, calculated with a combination of DFT and Green's function scattering methods [14, 18]. The peaks in the transmission can go above unity because they consider the 3 phonon polarization in the 3D space. Moreover, the transmission goes to zero at about 20 meV, as this corresponds to the limit of phonon density of states in the gold electrodes. All the molecular modes at higher energies are filtered by the leads and cannot contribute to the transport properties. Therefore, the measured thermal conductance strongly depends on the choice of the leads. In general, the lighter the metal used, the higher the Debye frequency and hence the higher the thermal conductance of the junction. It is also possible to play with the mismatch in the phonon frequencies of the electrodes by using different metals to reduce the overall thermal conductance, as demonstrated in a recent experiment [9].

Another important factor influencing the heat transport properties of molecular junctions is the coupling strength to the electrodes. This is probably the most studied and understood phenomenon in these systems. By changing the binding chemistry of the molecule to the electrodes from covalent to van der Waals, reductions up to a factor of 2 have been reported [8, 43, 44]. These results stress even further the influence of interfaces in determining the heat transport properties of these nanoscale systems.

One of the most universal results that was obtained from the Landauer formula is thermal conductance quantization [45, 46, 47, 48]. In the linear regime with ΔT $\ll$ T and if we assume perfect coupling of the phonon modes in the electrodes with the 1D system, equation 2.24 simplifies to

$$k = \frac{\pi^2 k_B^2 T}{3h} \tag{2.25}$$

This quantum of thermal conductance represents the maximum energy that each phonon mode can carry and interestingly, it was demonstrated that it is not dependent on the particle statistics and it is valid for both bosons and fermions[49]. Quantization of thermal conductance for phonons was proved only once experimentally[50], mainly due to technical challenges involved in such heat transport measurements.

Chapter 3

Experimental Setup

In this chapter the experimental setup developed to measure the thermal properties of atomic and molecular junctions will be presented. The first section introduces the experimental technique and the basic measurement procedure. It continues with the description of the setup, the laboratory environment, the data acquisition system and the mathematical model used to calculate the thermal and electrical conductance of the junctions from the measured signals. The following section describes the design, fabrication and characterization of the MEMS sensors. Finally, the sample and tip preparation are presented in detail, starting from the surface cleaning methods of the MEMS to its surface functionalization with organic molecules and fabrication of STM tips by electrochemical etching. The fabrication of the MEMS structures is performed by our collaborator Ute Drechsler in the cleanroom at IBM Zürich.

3.1 Experimental Setup

3.1.1 Introduction

Since the invention of the Scanning Tunneling Microscope (STM) in 1981 by Gerd Binnig and Heinrich Rohrer (at IBM Zürich)[51], many research groups started investigating the physical properties of organic molecules on metallic and insulating surfaces. In addition to the imaging capabilities with atomic resolution, STM provided a way to probe charge transport in single molecules. In the late nineties, researchers started to explore systematically such charge transport phenomena, giving rise to the field of molecular electronics. The original idea of using a single molecule as electronic device is often attributed to Aviram and Ratner in 1974 [52], who proposed a molecular diode consisting of a donor and an acceptor π-system separated by a sigma-bonded tunneling bridge, predicting its rectifying characteristics. The experimental challenge of contacting a single molecule was solved by the introduction of two techniques, namely the STM-Break Junction (STM-BJ) and the Mechanically Controlled Break Junction (MCBJ)[24], see section 2.1. The basic idea of both techniques consists in dynamically forming a sub-nm gap between two metal electrodes on which the target molecules are previously deposited. While opening/closing the gap between the electrodes in the tunneling regime, there is a certain probability for one or few molecules to bridge this gap. Since the molecule can bind in many different configurations to

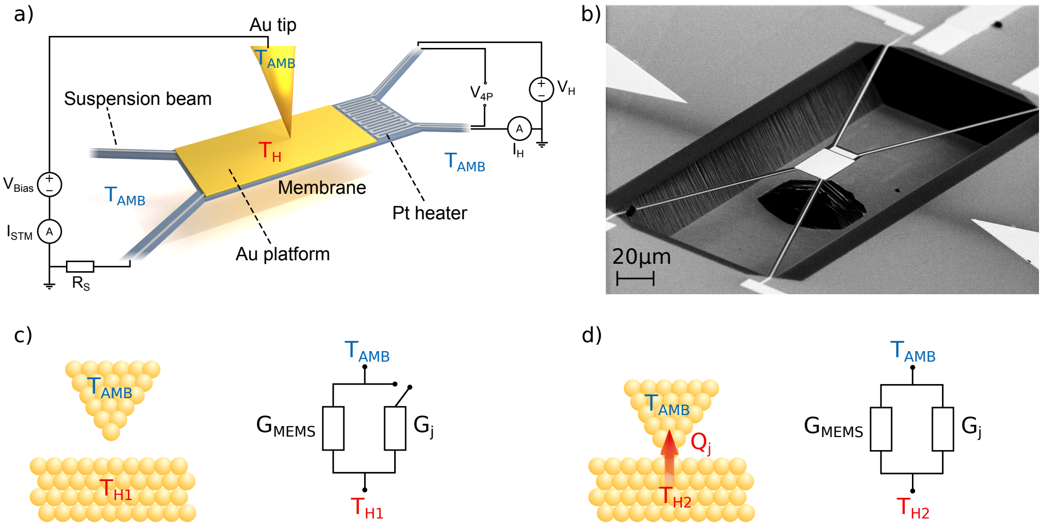

Figure 3.1: Working principle of the measurement technique. a) Schematic diagram of the experiment. To monitor the temperature T_H of the gold electrode, the four-probe voltage, V_{4P}, and the heater current, I_H, are measured. Simultaneous measurement of the tunneling current, I_{stm}, allows us to extract the electrical conductance of the junction. An external resistor R_s limits the current. b) Scanning electron micrograph of a typical MEMS used in this work. c) Prior to contact formation, the membrane is heated to T_{H1}. The total thermal conductance of the system is given only by the contribution of the suspension beams of the MEMS. d) After contact formation, the temperature of the membrane decreases to T_{H2}, because of the additional heat path. The total thermal conductance is now given by the sum of the thermal conductance of the MEMS (G_{mems}) and that of the tip-MEMS junction (G_j).

the metal electrodes, it is necessary to collect many of these conductance versus distance traces in order to get the most probable electrical conductance [53]. This break-junction method demonstrated to be very powerful to study charge transport in single molecule junctions and it was then further adapted to investigate the mechanical, optoelectronic and thermolectric properties [54]. However, heat transport in molecular systems has still been largely unexplored because of the lack of suitable experimental techniques [6]. In the following sections, I am going to explain how we combined the break junction technique with MEMS heat flux sensors to measure heat transport in single atomic and molecular junctions.

3.1.2 Working principle

In order to measure heat transport at the atomic and molecular scale, we combined the STM-BJ technique with highly thermally insulated heat flux sensors consisting of a suspended Micro-Electro Mechanical System (MEMS) with an integrated micro-heater, Figure 3.1. The experiments are performed in high vacuum (10^{-7} mbar) and at room temperature with a custom-built STM setup located in the IBM Noise Free Labs [55]. With the STM-BJ technique, we can measure the electrical conductance of the tip-MEMS contact and understand whether we have a single atom or a single molecule in the junction. The electrical conductance represents our reference signal, and thanks to the progress made in the molecular electronics field, we can use it to get information about the structure of the molecular/atomic junctions [56].

The MEMS consists of 4 SiNx suspension beams connected to a central part, which features a Pt micro-heater, to control and monitor the temperature, and a metallic platform, to form electrical contacts with the STM tip. Thermal equilibrium is assumed between the platform and the heater, due to larger thermal resistance of the suspension beams.The tip and the metallic platform are usually made out of gold, as one of the most commonly used metal in molecular electronics. To obtain the thermal conductance of the junction, we heat the MEMS to a temperature $\mathrm{T_H}$ by applying a constant voltage to the heater and then measure the heat flux to the tip, at room temperature, while forming and breaking contacts. Prior to contact formation, heat can be transported from the MEMS to the substrate only through the suspension beams[1]. We can then calculate the thermal conductance of the MEMS, defined as

$$G_{mems} = \frac{\dot{Q}}{\Delta T} \tag{3.1}$$

where $\dot{Q}$ is the total power provided by Joule dissipation and ΔT is the resulting temperature difference. Once a contact between the tip and the gold platform is formed, the ΔT decreases because of the additional heat path. In the electronic analogy, one can translate this scenario to the parallel of two conductances, as tip and substrate are at the same temperature. The thermal conductance of the junction is then obtained by subtracting the previously measured $\mathrm{G_{mems}}$. Typically, this procedure is repeated few 1000s times to collect statistics as in a standard break-junction measurement.

From this brief explanation, 2 important aspects of the measurement can already be understood:

1. To obtain the thermal conductance of the tip-MEMS contact we have to subtract a reference value, which, in the simplest case, corresponds to the thermal conductance of the MEMS, $\mathrm{G_{mems}}$. This means that the amplitude of the measured temperature change depends on the ratio between $\mathrm{G_{mems}}$ and $\mathrm{G_j}$; hence to have a good signal to noise ratio, the MEMS sensors should feature a thermal resistance as close as possible to $\mathrm{G_j}$.
2. To finely control the breaking process of the junction, the MEMS has to be mechanically stiff, setting a trade-off between mechanical stability and heat flux sensitivity.

In the following sections, these aspects will be addressed in some detail, as they provide the guidelines to design the experiment.

3.1.3 The setup

The development of the experimental setup, was initiated by Dr. Bernd Gotsmann. When I joined IBM in 2014, I started by optimizing, programming and developing the system further to reach the sensitivity needed for measuring the thermal conductance of single molecular junctions. The setup consists fundamentally of

---

[1] Note that in high vacuum there is no heat conduction through air. Moreover, the contribution of radiation to the thermal conductance of the MEMS is negligible for the temperature differences (<100 K) set during the experiment.

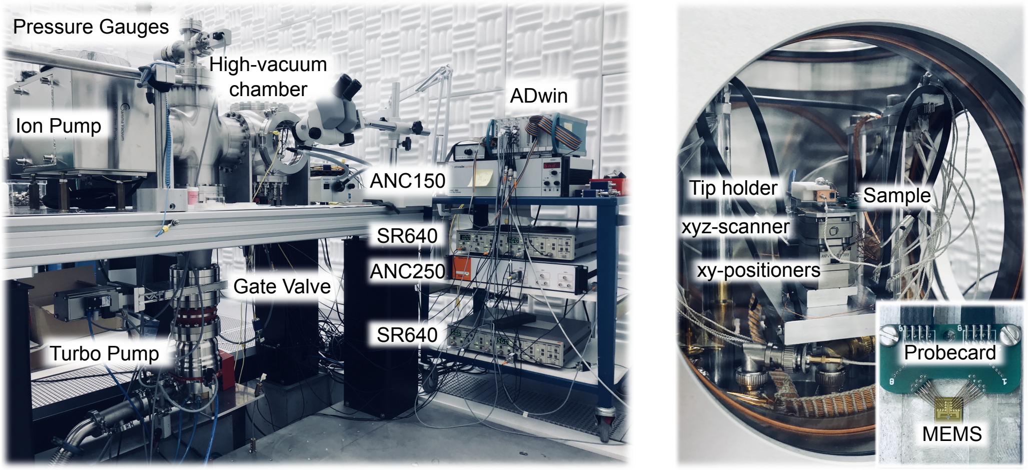

Figure 3.2: Picture of the experimental setup in the Noise Free Labs at IBM Zurich. On the left, one can see most of the setup and the sensitive electronic instruments. On the right, a view of the interior of the vacuum chamber with the piezo-scanner and positioners is shown. The inset displays a MEMS sensor (5 x 5 mm) electrically connected to the probecard on the sample holder.

a custom-built scanning tunneling microscope (STM) in high-vacuum, Figure 3.2. It is placed on an optical table, which is fixed on the concrete block of the anti-vibration system of the lab. The turbo pump (HiPace® 300 from Pfeiffer Vacuum) is connected to the main vacuum chamber from the bottom through a flexible hose to damp the vibrations generated by the rotation of the pump blades. The exhaust of the turbo pump is connected to the rotary pump located in the auxiliary room of the lab to reduce the noise. A pneumatic gate valve (VAT) can be used to isolate the vacuum chamber, so that the turbo pump can be switched-off. In this case, to maintain the low pressure inside the chamber, the ion pump (TiTan® from Gamma Vacuum) connected to the left side of the chamber is turned on. This combination allows us to minimize the mechanical vibrations induced on the setup while performing an experiment. We can reach a vacuum level below 10^{-6} mbar within an hour, if the chamber was not left to ambient pressure for more than a couple of hours. To increase the lifetime of the ion pump, we typically wait for the pressure to be around 10^{-7} mbar, which can take up to 12 hours. The chamber features 6 openings connected via CF160 flanges. A quick access door on the front allows us to load the sample and exchange tips. All the vacuum parts, apart from the door, are UHV compatible to allow more flexibility for the future developments of the setup. Inside the chamber (Figure 3.2), the sample holder is placed on a stack of piezoelectric elements consisting of 2 positioners (Attocube ANPx101) for the coarse motion in-plane and the open loop xyz-scanner (Attocube ANSxyz100) to perform STM-break junction measurements or STM imaging. The holder consists of a stainless steel base plate on top of which a probecard (from SQC AG) with pins arranged in a fixed layout is mounted. The MEMS samples are designed with the same contact layout, so that samples can be quickly exchanged without the need of wafer bonding. The holder is then magnetically fixed on the scanner thanks an intermediate plate screwed on the scanner itself which contains few strong permanent magnets. The tip holder is placed in front of the piezo-stack on the

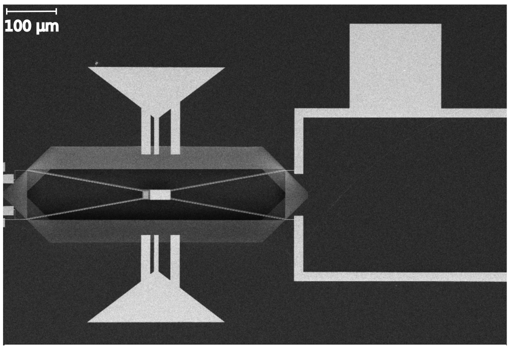

Figure 3.3: SEM image of a MEMS sample On the right side, the Au pad used to perform break junction tests is visible. On the left side, the MEMS is indicated by two arrow-like structures that serve for the optical positioning of the tip onto the gold platform.

positioner for the out-of-plane motion (Attocube ANPz101), which is used to coarse approach the tip to the sample surface. The lower piezoelectric elements are screwed on an aluminum base plate, which is suspended via 4 Viton® O-rings to damp the mechanical vibrations coming especially from the turbo pump. This simple solution is quite effective and it allows us to perform the break junction experiments with the pump running. In fact, it is very convenient to start measurements and perform preliminary tests on new samples while the turbo pump is still running, as one can save 5-10 hours of pumping time. The position of the aluminum plate inside the setup is adjusted at few cm distance from the front door, to enable optical access to the sample via the stereo-microscope. This is aspect is very important, because it allows us to reposition the tip on the MEMS anytime during the experiment or to move it to the substrate. It is in fact normal practice in the STM community to clean or reshape the tip, by gently crashing it onto a metallic surface with a high voltage applied (> 5 V). As this step cannot be performed directly on the MEMS, mainly because of induced overheating, we typically move the tip to the substrate and do such tests on a predefined gold pad, as shown in Figure 3.3.

One last important aspect of the setup is the cabling inside the vacuum chamber. To minimize the electronic noise level of the measured signals, it is better to use short coaxial cables directly from the probecard to the feedthroughs. At the same time, the cables mechanically link the piezo-scanner with the chamber, and thus their stiffness must be also minimized. Therefore, we decided to connect the probecard to an intermediate series of pins, which are fixed on the aluminum baseplate and connected to the feedthroughs via longer coaxial cables.

3.1.4 Noise Free Labs

The setup is located in the Binnig-Roher Nanotechnology center in Zurich inside one of the Noise Free Labs. These laboratories were devised in order to reduce the influence of external noise sources so that almost any kind of experiment would profit from such an environment. The laboratory consists of an experiment room where the setup and the sensitive electronic equipments are placed, one operator room, from where the researcher can control the setup and two additional side rooms, containing the noisy equipments like the scroll pump for the pre-vacuum and the PC

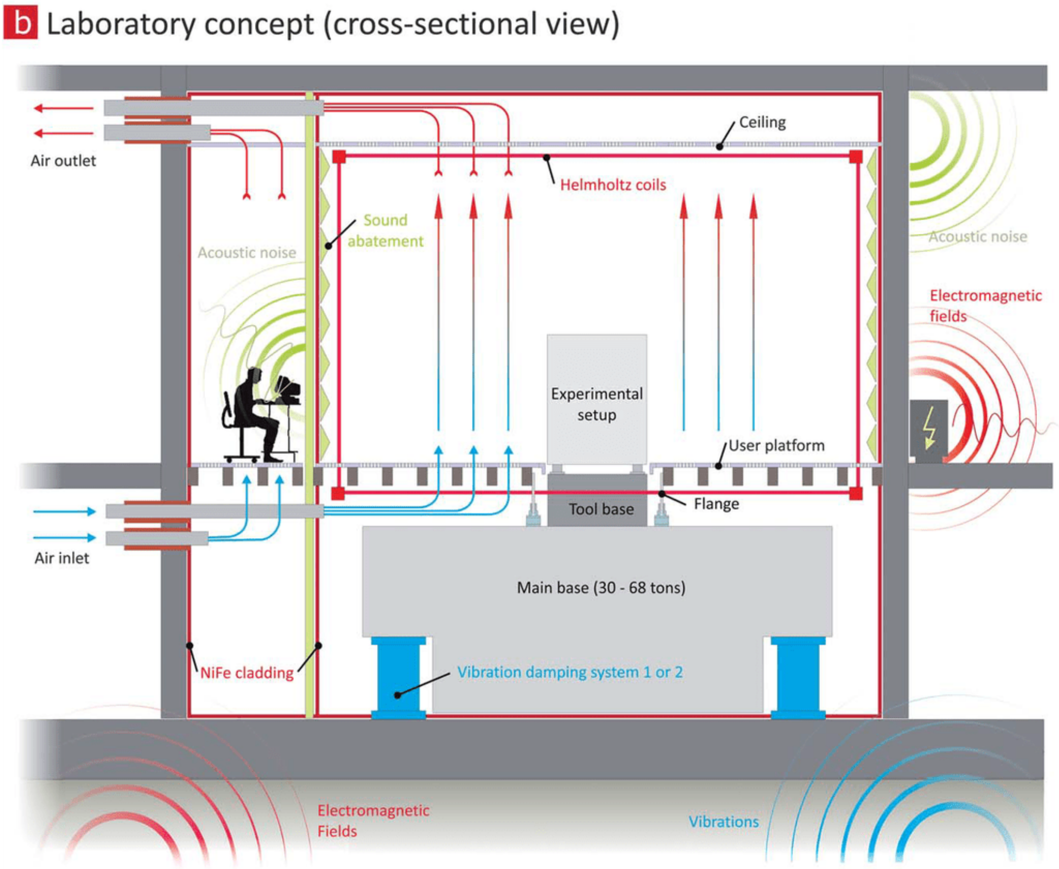

Figure 3.4: Schematic of the laboratory concept. The laboratory combines air conditioning system for the humidity and temperature control, shields and active compensation to screen external electromagnetic fields and vibration isolation, achieving unprecedented low levels for the main noise sources (reproduced from [57],[55]).

itself. Figure 3.4 shows a cross-section of the lab with the operator and experiment room. The setup is placed on a large concrete block of 30 to 68 tons to passively damp the high frequency mechanical vibrations (above 5 Hz). This main base is further suspended on a combination of air springs and air cushions to allow for active compensation of the remaining vibrations. With this implementation, vibrations of less than 300 nm/s at 1 Hz and less than 10 nm/s above 100 Hz were achieved. The air conditioning system was designed in a way that the air flow does not excite the concrete block. In this way, the temperature is kept constant within ±0.01 °C and the humidity within ±2%. Sound-absorbing panels cover the walls of the experiment room to absorb the acoustic noise generated inside and outside of the laboratory. Isotropically conducting NiFe sheets (80% Ni, 20% Fe) were used to coat the door, walls and ceiling, forming a magnetic cage that shields from mid and low frequency electro-magnetic fields (100 Hz – 100 kHz). An aluminum top layer was welded to the magnetic layer forming a Faraday cage. Moreover, three Helmholtz coils were installed inside the room to actively compensate for variations in the DC magnetic field. In terms of performances, electromagnetic fields with AC peaks of less than 0.3 nT at 50 Hz and 250 Hz and DC variations of less than ±15 nT were achieved. Working in such a special environment, particular care has to be taken in order to not

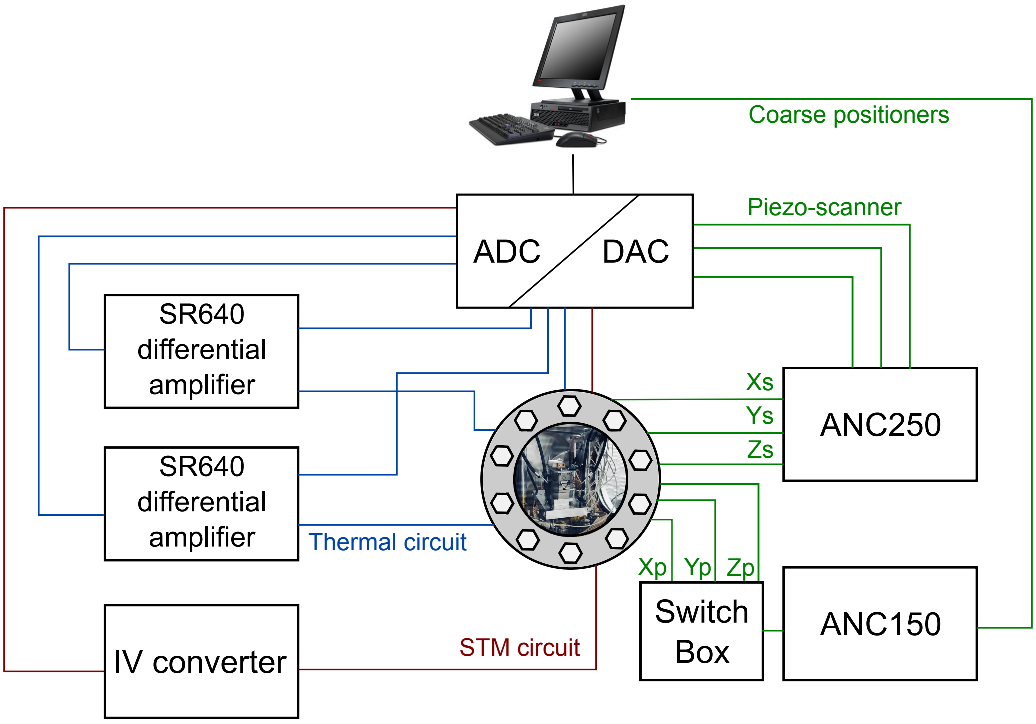

Figure 3.5: Schematic view of the data acquisition and control circuitry. The red circuit is used to measure the tunneling current between the STM tip and the MEMS platform. The green circuit controls the piezoelectric scanner through the high-voltage amplifier ANC250 and the coarse positioners through the ANC150 control unit. Finally, the blue circuit is used to measure the 4-probe resistance of the heater element integrated on the MEMS and the dissipated electrical power.

degrade the performances of the laboratory and profit the most from it. For instance, we tried to damp the vibrations coming from the vacuum pumps by using flexible vacuum connectors to the the main chamber. Despite of generating electric noise, we placed most of the electronic instruments (differential amplifiers and ADC/DAC cards) inside the laboratory close to the experiments, to minimize the pick-up noise induced in long coaxial cables and the input capacitances to the amplifiers. Even if we cannot directly measure the benefits of being in this controlled environment for our experiment, we definitely observe great advantages, compared to a standard laboratory. First of all, thanks to the vibration damping system and the temperature stabilization, mechanical drifts of the piezoelectric positioners/scanner are greatly minimized. Moreover, keeping continuously a constant temperature greatly reduces the variations in the electronic offsets and gains of the amplifiers. For instance the voltage offsets at open circuit that we measure before starting every experiment show very small variations from month to month.

3.1.5 Data acquisition and system control

The data acquisition system is depicted in Figure 3.5. The measurement unit is the ADwin Pro II, featuring an internal processing unit with 300 MHz clock rate, 768 kB local memory and 256 MB RAM which allows floating point operations with

40-bit resolution. It is a flexible system that can be personalized with different functional modules, e.g. Analog, Digital and Counter modules. In our case, we installed an analog input card with 8 differential channels, and ADC resolution of 18-bits and a conversion time of 2 µs, an analog output card, with 16-bit resolution and a settling time of 3 µs, and a digital card with 32 inputs/outputs. Both analog cards have a dynamic voltage range of ±10 V. The ADwin has its own programming environment (ADbasic) and, thanks to the internal processing unit, it can handle multiple programs at once with very precise timing, giving us high flexibility. We use the ADwin to control the open loop piezoscanner via a low noise, high voltage amplifier (ANC250 from Attocube) and as voltage source for the thermal and electrical circuits. The coarse positioning is instead performed with a separate control unit (ANC150 from Attocube) directly connected to the computer. The analog inputs of the ADwin are connected to the IV converter for the STM current and to the differential amplifiers (SR640 from Standford Research) for the heater resistance and current. In order to perform a measurement, we load a specific routine on the ADwin processor and read/write data by using a Matlab® interface. The main advantages of this approach are the precise and fast acquisition rates (independent of the computer load) and large flexibility in terms of functions that can be implemented with a combination of Matlab and ADbasic scripts. For instance, the speed of the main routine performing the STM-BJ measurements was optimized to 300 kHz. However, the ADwin system is designed to maximize the speed of operation and special care has to be taken to obtain low-noise levels. Providing a good ground to the experiment can be considered as an art.

3.1.6 The electrical circuits

In this section the details of the mathematical model used to calculate the thermal and electrical conductance of the junction are presented. Figure 3.6a shows a simplified schematic of the thermal circuit, to measure the 4-probe voltage $\mathrm{V_{4P}}$ and the heater current $\mathrm{I_h}$. From the measured signals $\mathrm{V_1}$ and $\mathrm{V_2}$ we can define

$$V_{4P} = \frac{1}{A_1}\frac{(V_2 - V_{2off})}{A_2} + V_{ref2} \tag{3.2}$$

$$I_h = \frac{V_s}{R_s} = \frac{1}{R_s}\frac{(V_1 - V_{1off})}{A_3} + V_{ref1} \tag{3.3}$$

where V_{1off} and V_{2off} are the offset measured at $\mathrm{V_{tot}} = 0$. From these values we can readily calculate the 4-probe resistance of the heater $R_{4P} = V_{4P}/I_h$ and extract its temperature T by using

$$T - T_{amb} = \frac{1}{\alpha}\frac{R_{4P} - R_{4Pamb}}{R_{4Pamb}} \tag{3.4}$$

where α is the temperature coefficient of resistance of the Pt-heater and R_{4Pamb} the electrical resistance of the heater at ambient temperature T_{amb}. The total power P provided to the MEMS central platform is defined as

$$P = R_h I_h^2 + r_u R_b I_h^2 \tag{3.5}$$

where first term represents the contribution of the heater and the second term the one of the suspended portion of two metal lines carrying the current (each metal

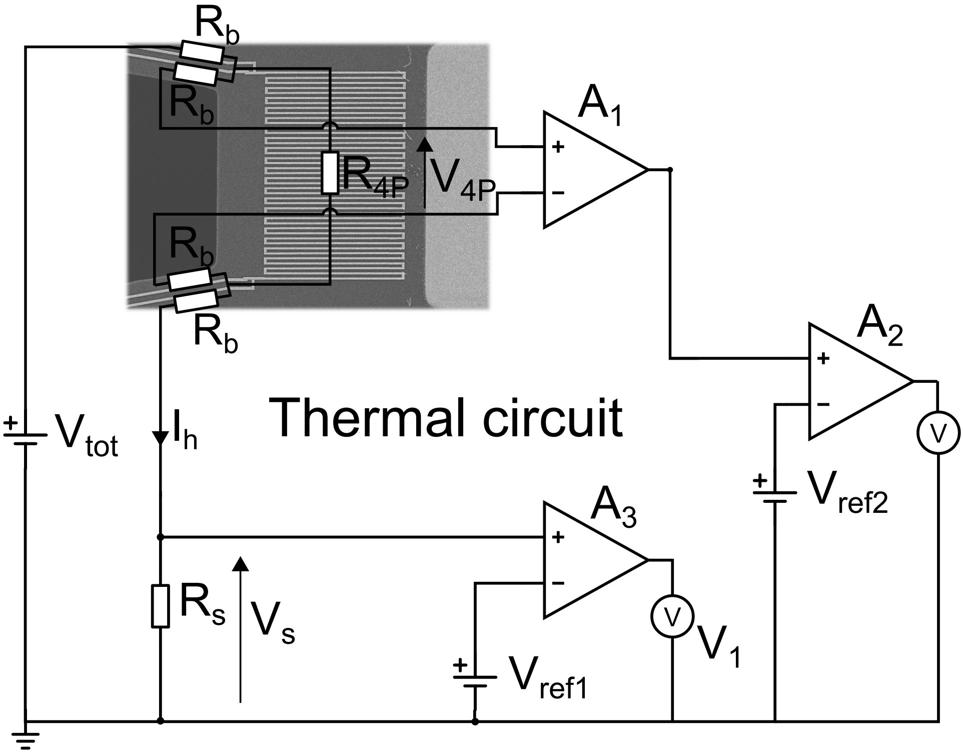

Figure 3.6: Schematic of the electric circuits used to measure the thermal conductance of the junction. R_{4P} is the 4-probe resistance of the heater, R_b the resistance of the metal line along the beam, R_s is the series resistance. V_{tot}, V_{ref1} and V_{ref2} are voltage outputs of the data acquisition system while V_1 and V_2 are the 2 signals measured. Differential amplifiers indicated with gains A_1, A_2 and A_3 are used to filter and amplify the 4-probe voltage V_{4P} and the voltage drop over the series resistance V_s.

line contributes with a power $0.5 \times r_u R_b I_h^2$). R_b is obtained from the value of the 2-probe resistance $R_{2P} = V_{tot}/I_h = R_{4P} + 2R_b$. It can be demonstrated that half of the total electrical power generated in the metallic line over the beam is effectively increasing the mems temperature whereas the other half is directly dissipated into the silicon substrate. Moreover, as only the portion of the line that is suspended has to be considered, we can introduce a correction factor r_u representing the fraction of electrical resistance of the underetched portion, Figure 3.7. $r_u \sim 85\%$ can be directly estimated from the design layout, as it depends only on geometrical factors. Note also that the heater current flows mostly in the outermost metal lines as the inner ones are connected to the high-input impedance of the differential amplifiers. At this point, we can use equation 3.1 to calculate the thermal conductance of the device. The advantage of using this configuration of differential amplifiers is that we can set high gains A_2 and A_3 (≥ 1000) by subtracting the reference voltages V_{ref1} and V_{ref2} and focus on the small resistance and current changes occurring during the STM-BJ measurement.

To measure the electrical resistance R_J of the junction we normally apply a small constant bias $V_b < 100$ mV to the tip and measure the current with an IV converter

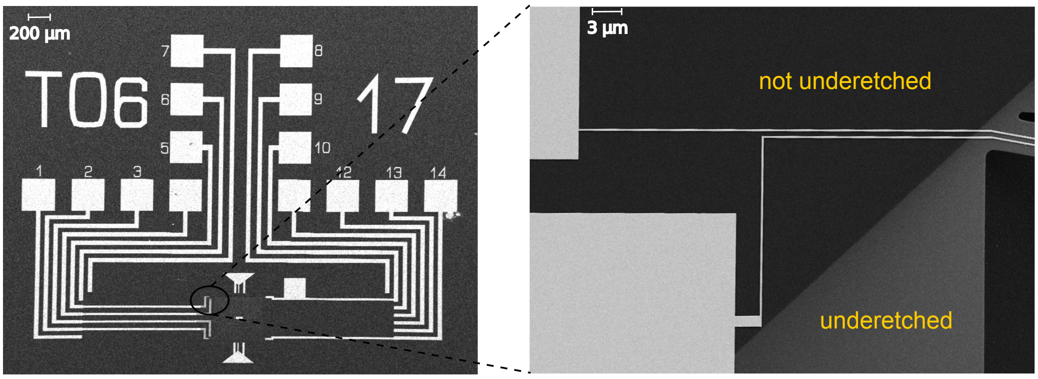

Figure 3.7: SEM image of the contact layout of the MEMS sample (a) showing the portion of the metal lines which is not underetched (b).

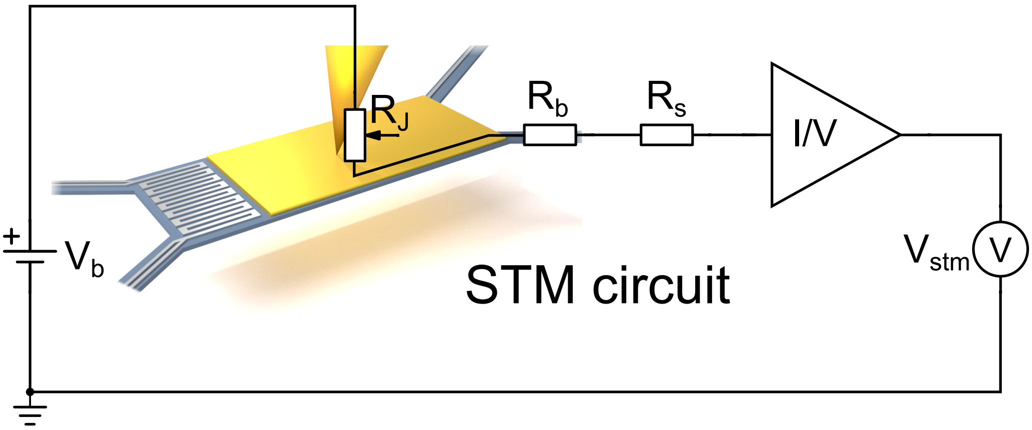

Figure 3.8: Schematic of the electric circuits used to measure the electrical conductance of the junction. R_J is the electrical resistance of the Tip-MEMS junction, R_b is the resistance of the electrical line along the beam and R_s the external series resistance used to limit the STM current. The amplifier is a current to voltage (IV) converter. V_b and V_{stm} are the voltage output and input of the data acquisition system, respectively.

connected to the metallic platform on the MEMS, Figure 3.8. Then we can use

$$R_J = \frac{V_b}{I_{stm}} = \frac{V_b \times A}{V_{stm} - V_{off}} - R_b - R_s \tag{3.6}$$

with V_{off} being the offset measured at open circuit and A the gain of the IV converter. R_b was obtained previously by connecting the bias voltage to the second metallic line going to the platform and measuring the 2-probe resistance. Typical values for the designs used in this project go from 30 to 4 kΩ depending on the width of the metal. The external series resistance R_s serves to limit the stm current and avoid damaging the MEMS when a large metal contact is formed with the tip. Moreover, without switching the gain of the IV converter, we can measure resistances with a larger dynamic range, as required for STM-BJ (from 1 kΩ to 10 GΩ). The value of the series resistance is usually set to 10-100 kΩ.

Corrections to the mathematical model

The model presented above collects the main parameters used in the analysis but it is not complete. In fact, to increase the accuracy of the measurement several corrections have to be taken in account for both the thermal and electrical circuit. In the first case, the 4-probe resistance measurement is not ideal, as the input impedance of the amplifiers (SR640 Stanford Research) is equal to 1 MΩ, which is only 25 times larger than the 2P-resistance of the heater ($\sim$ 40 kΩ). Therefore, if we modify the circuit in Figure 3.6 introducing the input impedance of the amplifiers, we can correct for this effect and compute also the values of the actual currents flowing in each beam. Without correction, the value of the heater and beam resistances is overestimated by roughly 1%. Another factor that has to be considered concerns the calculation of the power provided to the MEMS. When the STM current $I_{stm} \neq 0$, additional heat is generated at the junction resistance R_J and in the series resistance on the beam R_b. To correct for this effect, we can calculate the heat generated in the STM circuit

$$P_{stm} = \frac{1}{2} R_J I_{stm}^2 + \frac{1}{2} r_u R_b I_{stm}^2 \tag{3.7}$$

and add it to the power provided by the heater in equation 3.5. The second term is analogous to the formula used for the contribution of the heater lines. The first term instead, comes from the assumption that in atomic or molecular junctions the power is dissipated symmetrically in the electrodes, tip and MEMS. It was recently demonstrated that in systems that can be described with the Landauer formalism, it exists a direct relationship between the transmission function T(E) of the junction and the power dissipation [58, 59, 60]. Specifically, if T(E) varies slowly around the Fermi energy of the electrodes (E_F) then the power is dissipated symmetrically in the electrodes, as in the case of gold atomic contacts. However, if this is not the case, as it is usually for molecular junctions, then Peltier effects come into play and the dissipation is asymmetric. The degree of asymmetry is strictly related to the slope of T(E) at E_F and hence to the Seebeck coefficient. Thus, we can use equation 3.7 for the case of metallic contacts and for molecular junctions we can estimate the order of magnitude of the asymmetry from the reported values of Seebeck coefficients. Note that because of the high resistance of single molecule junctions and small voltage applied $V_b < 100$ mV, these effects are mostly negligible.

Further corrections are needed also for the calculation of the junction resistance. The first comes from the measurement configuration: when using an IV converter (i.e. feedback ammeter) the series resistance R_s should be higher than the gain of the amplifier A [61], as voltage offsets and noise sources at the input of the ammeter are amplified by A/R_s. In our case we usually set $A = 10^7$ and $R_s = 100$ kΩ. This means that for metallic contacts ($R_J \leq 12.9$ kΩ) we must introduce an additional correction factor V_c that takes into account the small errors in the voltage bias V_b and internal offsets of the IV-converter. We can then modify equation 3.6 to

$$R_J = \frac{(V_b - V_c) \times A}{V_{stm} - V_{off}} - R_b - R_s \tag{3.8}$$

For characterizing V_c, we substituted R_J with previously calibrated resistors spanning the target resistance range. Without this correction factor, the values measured can be off by 50% in the resistance range below R_s. Typical value for V_c is 0.9 mV and it is slightly dependent on the voltage bias applied V_b. After this calibration procedure, the junction resistance can be measured with an accuracy $\leq 2\%$ from 1 kΩ to 10 GΩ.

The second correction factor which has to be taken into account deals with the resistance of the metallic line along the beam R_b. While, in the case of the thermal circuit the beam resistances are continuously monitored, for the STM circuit, the value of R_b is taken only once before starting the STM-BJ measurement. The line is usually made out of platinum and varies with the average temperature of the beam, having the same temperature coefficient of resistance α of the heater. Therefore, the suspended part of R_b is temperature dependent and we can insert in equation 3.8

$$R_b = r_u R_{b,amb}\left(1+\alpha\frac{\Delta T}{2}\right) + (1-r_u)R_{b,amb} \tag{3.9}$$

with ΔT being the temperature difference measured with the heater and $R_{b,amb}$ the value of the resistance at ambient temperature. The magnitude of this correction depends on the value of $R_{b,amb}$ and it has a substantial influence only for metallic contacts. Combining equation 3.9 with 3.7, we can also be more accurate in the estimation of the power dissipated.

3.2 MEMS design, fabrication and characterization

Suspended micro-structures with integrated heaters have been widely used for many different thermal transport applications, from the characterization of the thermal properties of nanostructured materials [62, 63, 64, 65] to the measurement of the phononic thermal conductance quantum[50], near field heat transfer[66]. The main reason for this is the lack of very good thermal insulators. If we consider the range of electrical conductivities in standard materials, there is a difference of more than 26 orders of magnitude between fused quartz (one of the best insulators) and silver (one of the best conductors). On the other hand, if we look at the thermal conductivity range, there are only 5 orders of magnitude between the best thermal insulators (e.g. silica aerogels with k $\sim$ 0.01 W/(mK)) and the best conductor (diamond with k $\sim$ 2200 W/(mK)). This means that experimentally is very hard to control or to confine heat fluxes along guidelines, as one can do with charge. One ways of measuring the thermal conductivity at the micro- and nano-scale consists in using vacuum as thermal insulator by suspending the structure under test between two MEMS platforms and measure the temperature rise in one of them while the other one is heated. Usually, the only requirement for such applications is having MEMS characterized by high thermal resistance, so that small heat fluxes can induce a measurable temperature change. The stiffness of these MEMS platforms becomes really important in experiments probing near field radiation between two surfaces at nm distances, as the attraction forces between them tend to pull them together. In our case, we use a suspended MEMS with an integrated heater/sensor with a high thermal resistance ($\sim 2 \times 10^7$ K/W) as one reservoir and then we connect it to the STM tip by forming contacts composed of few metallic atoms or organic molecules. Similar to near field experiments, stiffness, thermal insulation and mechanical stability are fundamental aspects that have to be optimized.

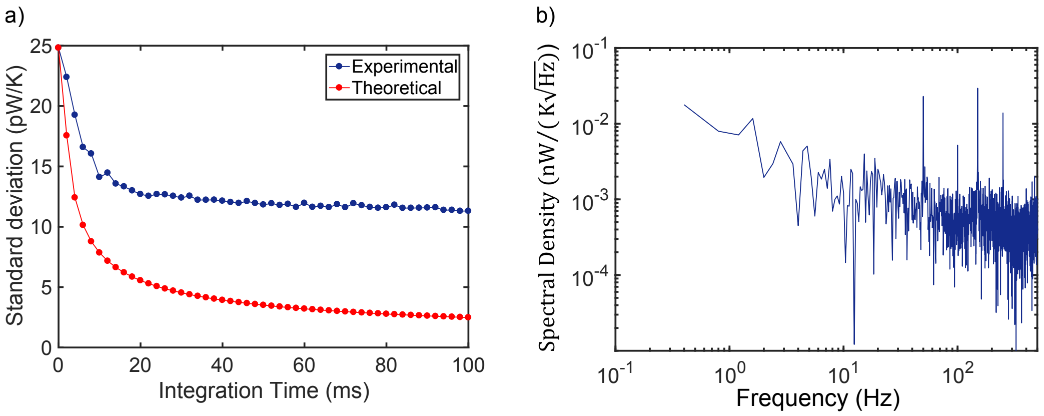

Figure 3.9: Standard deviation and spectral density of the thermal conductance measured at $\Delta T = 50$ K. a) Standard deviation of the thermal conductance at different integration times (blue) and expected trend for white noise only. b) Spectral density of the thermal conductance measured with a sampling time of 1 ms.

3.2.1 Noise performance

For the STM circuit several options were tested during the PhD project in order to minimize the noise level. In fact, STM-BJ measurements require large dynamic range (from pA to µA) and bandwidth (∼ 1 kHz). Several solutions were proposed in the field of molecular electronics from logarithmic amplifiers to combinations of 2 linear amplifiers with different gains [67]. By simply measuring the voltage drop over a 100 kΩ resistance in series with the junction, we could obtain a noise level of G$\sim 10^{-5}$ G_0 at $V_b = 50$ mV and a voltage amplifier (SR640) with gain ×100. With the transconductance amplifier DLPCA-200 (FEMTO) with gain $\times 10^6$ and an additional voltage amplifier stage with gain ×10 we decreased the noise to G$\sim 5 \times 10^{-6}$ G_0 with V =50 mV. The main drawback of the FEMTO amplifier is the limited dynamic output range of ±1V for a 50 Ω load, which is not matched with input range of the ADwin (± 10 V). The best results were obtained with the low-noise I-V converter from the University of Basel (SP 983), featuring an automatic offset compensation and and a dynamic range of ±10 V giving a noise level of G$\sim 10^{-6}$ G_0 at $V_b = 90$ mV. Most of the interesting molecules for molecular electronics applications have an electrical conductance above $\sim 10^{-6}$ G_0, within our measurement range. However, in the future, it might be interesting to extend this even further, to probe the thermal conductance of long molecular backbones [35] or bridges created through $\pi - \pi$ interaction [68].

The noise level of the thermal conductance signal was optimized by using the 2 differential amplifiers SR640 (Stanford Research). In particular, the 4-probe voltage drop over the heater and the heater current are amplified with a gain of ×1000 after the subtraction of a suitable voltage offset coming from the ADwin. In this configuration, we can easily compensate for the large changes in resistance occurring when setting a different temperature to the heater (∼ 2 kΩ) and increase the gain of the amplifier to measure the small variations induced by the heat flowing to the tip (∼ 1 Ω). Figure 3.9b shows the thermal conductance noise spectrum measured at $\Delta T = 50$ K. The peaks at multiples of 50 Hz appearing in the spectrum may

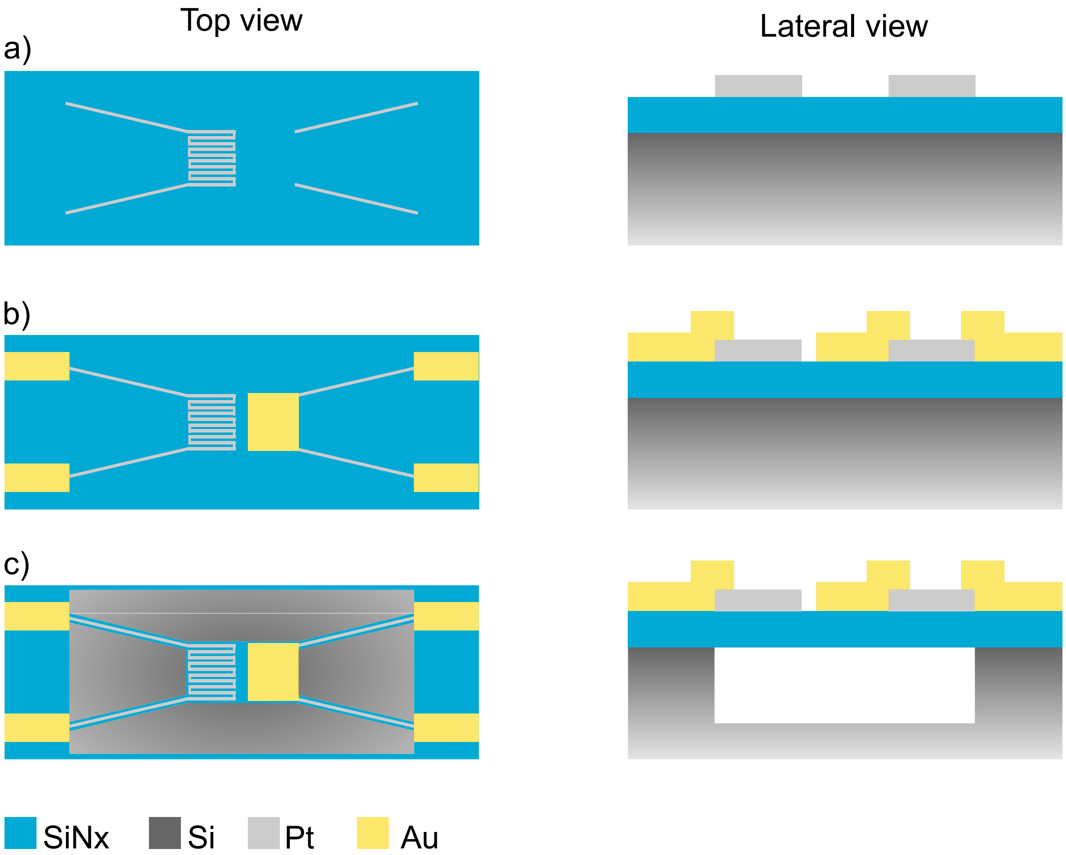

Figure 3.10: Fabrication process flow of the MEMS. a) The Pt heater and leads are patterned by e-beam lithography on the SiNx layer. b) Au is deposited and patterned by lift-off. c) SiNx is removed to define the shape of the MEMS, which is then released by etching the Si substrate underneath with TMAH.

come from several sources and it is very challenging to remove them completely. By integrating the signal for at least 20 ms the noise level reduces to 13 pW/K as shown in Figure 3.9a, which is the best resolution reported up to date in a bandwidth of 50 Hz[69, 70]. This corresponds to a sensitivity of $T = 20$ mK, $R = 0.6\ \Omega$ (over 25 kΩ) and heat flux $P = 650$ pW in the same bandwidth. We would like to stress that we don't employ any modulation scheme to measure the temperature of the heater, which would result in a higher sensitivity, well below 1 μK regime [71]. However, temperature fluctuations of the compliant MEMS structures would detrimentally affect the mechanical stability of the junction and strongly decrease the bandwidth, making the STM-BJ measurement very challenging. Future tests with AC techniques are planned to explore the resolution limits of the setup and investigate these experimental issues.

3.2.2 Fabrication Process

For the fabrication of the MEMS devices we follow a process similar to the one outlined by Karg et al.[62]. In the most simple version, it consists of 3 lithographic steps: 1 electron-beam lithography (EBL) and 2 optical lithographies. The whole fabrication process is carried out in the cleanroom at IBM in Rüschlikon by our colleague Ute Drechsler, apart from the initial wafer stack, which is bought from SiMat in Germany. We start from a 4-inch silicon wafer coated with 150 nm Low-Stress SiNx (SiMat, Germany). We then thermally evaporate 25 nm of Pt with 2 nm of Cr as adhesion layer. We pattern the Pt layer by e-beam lithography to fabricate the heater and the suspended metal lines, Fig. 3.10a. Afterwards, we sputter 50 nm of Au and we define the platform on the MEMS and the contact pads by using optical lithography in combination with a lift-off process, Fig. 3.10b. Finally, we perform an optical lithography step to define and release the MEMS by underetching the SiNx layer in tetramethylammonium hydroxide (25% concentration for 30 min at 80 °C) with subsequent replacement of solvent using isopropanol, which is then removed in a critical point dryer, Fig. 3.10c. The resulting MEMS structure consists of four SiNx beams of lengths ranging from 250 µm to 500 µm, according to the design, thickness t = 150 nm (as defined by the SiNx layer) and width w = 4 µm. Typically, the Pt lines connecting to the heater element have widths between 100 and 200 nm, while the lines to the Au platform are designed with a larger width of about 400 nm to minimize the electrical resistance. Several variations of this process were tested during the course of the PhD project. For instance, the lift-off process to pattern the gold layer, was substituted by chemical etching. Although increasing the edge roughness, this solution allowed to reduce the number of short-circuited devices because of lift-off residues peeling-off the borders of the gold lines. Another interesting approach that was tested, consisted in substituting the Pt-lines used to contact the the Au-platform on the MEMS with Au-lines patterned by e-beam lithography. This is particularly useful in experiments, as the Pt-Au junction on the MEMS contributes with a Seebeck voltage when the MEMS is heated that introduces uncertainty in determining the electrical resistance of the junction. The effect of not having a metallic heterojunction in the STM circuit was successfully tested, however, introducing two additional e-beam patterning steps (as one is needed to pattern the e-beam alignment marks, preferably made out of tungsten) makes the fabrication process more time consuming.

3.2.3 MEMS design

In order to probe heat transport through atomic and molecular junctions, we need to measure thermal conductance variations on the order of 10 pW/K while repeatedly forming and breaking of such junctions at room temperature. So in the ideal case, we would like to fabricate MEMS sensors featuring a low thermal conductance ($G_{th} \sim 10^{-8}$ W/K), high bending stiffness ($k > 100$ N/m) and fast response time ($\tau \sim 1$ ms). However, optimizing these parameters at the same time is very challenging, as the thermal and mechanical properties of the MEMS sensors are fundamentally linked together. The thermal conductance G_{th} of a beam is defined from Fourier's law for heat conduction as

$$G_{th} = k_{th} \frac{A}{L} \tag{3.10}$$

were $k_t h$ is the thermal conductivity, A and L are the cross-section and the length of the beam, respectively, Figure 3.11. According to this formula, we can readily see that in order to minimize G_{th} we must choose a material with low thermal conductivity and design long supporting beams with a small cross-section. The material of choice is silicon nitride with typical thermal conductivity of 3-4 W/mK[72, 73] and a Young modulus $E \sim 260$ GPa[74] in thin films. The low

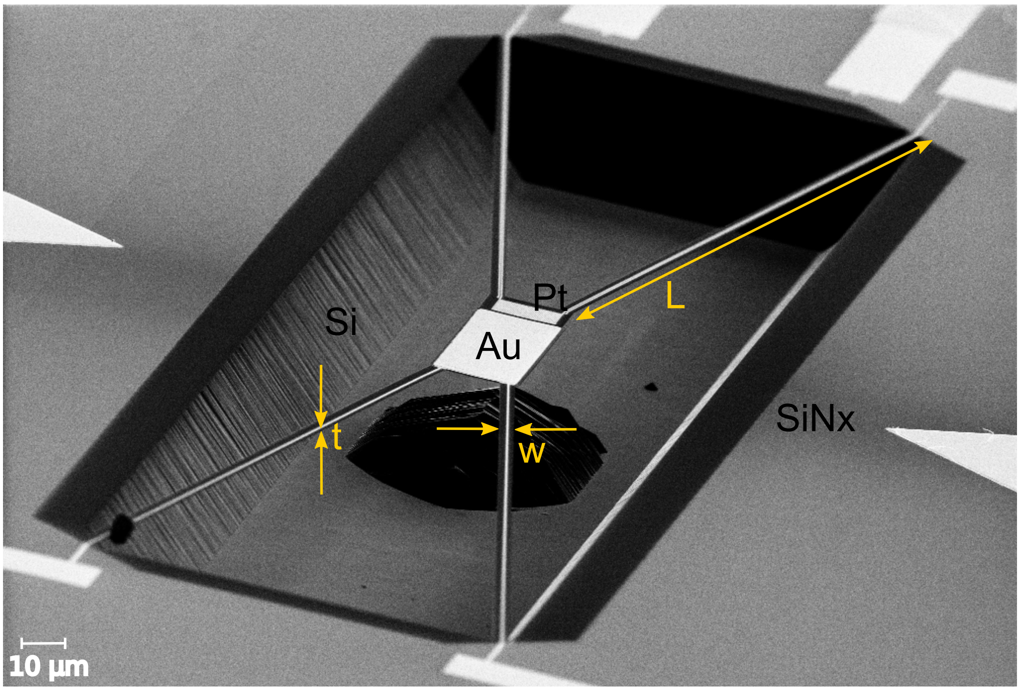

Figure 3.11: SEM picture of a typical MEMS design. The silicon nitride beams are characterized by a thickness t, width w and length L, as indicated in the figure.

thermal conductivity value together with a high Young modulus and established fabrication procedures to build suspended membranes on silicon makes it suitable for our application. In terms of geometry, we decided to focus on low-stress silicon nitride films on silicon with a thickness t =150 nm (purchased from SiMat in Germany). As the width w of the beams is constrained by the optical lithography resolution and alignment step to 2 µm, the length of the beams L remains the main design parameter. In practice, the usual width of the silicon nitride beams is 4 µm, to compensate for misalignments with respect to the metallic lines, see 3.2.2. An important contribution to the thermal conductance may come from the Pt lines used to contact the heater and the gold platform. Evaporated Pt thin films have a thermal conductivity of about 30 W/mK at room temperature. For this reason, we usually design lines with a thickness of 25 nm and width of 100 to 200 nm, so that their contribution to the overall thermal conductance stays below 10%. During the PhD project, we fabricated several MEMS structures having beams with different lengths from 250 µm to 500 µm and a measured thermal conductance $G_{mems} \approx$ 4 and $2{\times}10^{-8}$ W/K, respectively. However, because of the greater mechanical stability, the beams with $L \simeq 250\mu$m are usually preferred.

Modeling the mechanical stiffness of the MEMS is quite challenging, as it depends on many parameters that are not easily accessible, like the residual stress in the layers after fabrication, the torsional and flexural bending modes, the thermal stress induced during operation because of the thermal expansion of the SiNx and metallic layers. However, to give an estimate of the out-of-plane stiffness, we can use linear

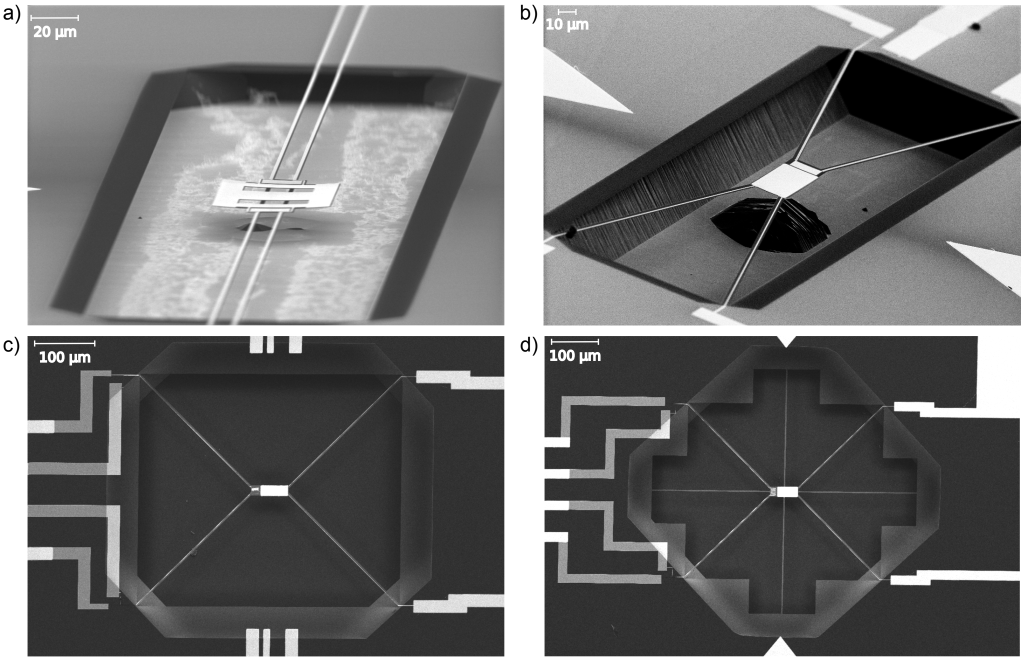

Figure 3.12: SEM pictures of several MEMS designs. a) One of the first MEMS designs. The central platform features some openings to facilitate the releasing process by exposing the silicon underneath to the etching solution. In the next generations, this feature was dropped as no issues during the release were observed. b) MEMS design with tilted beams with an angle of 10° with respect to the MEMS longitudinal axis. c) MEMS with beams at 45° with respect to the MEMS longitudinal axis. d) MEMS with 4 additional SiNx beams to improve the mechanical stability along every direction.

elastic continuum theory expressions for double-clamped beams under stress [75, 76],

$$k_\perp = 16\frac{Ewt^3}{L^3} + \frac{24\sigma wt}{5L} \tag{3.11}$$

where σ represents the tensile uniaxial stress along the silicon nitride beams. By modeling the MEMS as two SiNx beams of length $L = 600\mu$m (equal to the length of the two beams plus the central platform), thickness t = 150 nm, width w = 4 µm, Young's modulus E = 260 GPa and tensile stress $\sigma \sim$ 75 MPa, we obtain a stiffness of $\sim$ 0.7 N/m, strongly dominated by the stress term. Note that additional contributions to the stress may come from the deposition of Pt and Au and from the thermal stress induced upon heating of the MEMS. Compared to the stiffness of Au-Au contacts ($\sim$ 5N/m [77]), this is clearly not enough for achieving a controlled breaking process. From the fabrication point of view, we did not find many solutions to increase the bending stiffness without affecting the thermal conductance. One way, for instance, would be to design T-shaped beams [78] or reverse the entire geometry of the experiment by placing the sensor on the tip side [70, 69]. However, by performing the first experiments, we found out that by simply moving the STM tip at an angle with respect to the MEMS surface, we can take advantage of the larger in-plane stiffness and achieve a controlled breaking process, without changing the fabrication process. In particular, if the beams are designed at an angle β with respect to the axis of the MEMS, we can reduce the torsional degrees of freedom and exploit the uniaxial stiffness of the beams

$$k_{\parallel} = E\frac{wt}{L}\sin(\beta) \tag{3.12}$$

with values of about 135 N/m for a single beam. In fact, if the applied force is not perpendicular to the beam axis, we have to consider the contribution of the bending given by 3.11 and of the elongation along the axis with 3.12. We would like to point out that the estimations given here carry significant uncertainties since we consider only a very simplified model of the MEMS structure. Nevertheless, they serve to explain the empirical finding of a very different in-plane and out-of-plane stiffness resulting, for example, in different spring-loading distances in the two directions.

Figure 3.12 shows few examples of MEMS structures fabricated during the PhD project. Empirically, the best design (out of 20 basic structures) for the break junction experiment is the one with beams at 45° with respect to the longitudinal axis of the MEMS, Figure 3.12c. Other designs with additional supporting beams did not show particular improvements in the experiment, Figure 3.12d.

Another important aspect concerning the design of the beams, comes from the assumption that the temperature on the MEMS is homogeneous and corresponds to the one of the Pt heater. This assumption holds only if the thermal resistance of the beams is much larger than the one of the central platform. Indeed, going from the heater to the substrate, the MEMS can be modeled as the series of 2 thermal resistances $R_{th} = R_{plat} + 2R_{beam}$ (note that in the opposite direction $R_{th} = 2R_{beam}$). Therefore, the temperature difference over the platform can be calculated with $\Delta T_{plat} = R_{plat}/(R_{plat} + 2R_{beam}) \times \Delta T$, where ΔT is the temperature difference between the heater and the substrate. Using equation 3.10, with a thermal conductivity of Au $k_{Au} = 125$ W/mK (extracted from the electrical conductivity of the gold lines) and neglecting the interfacial thermal resistance between gold and silicon nitride, we obtain $R_{plat} = 3$ to 4.5×10^5 K/W for the different MEMS designs, corresponding to a maximum ratio $\Delta T_{plat}/\Delta T < 1\%$, with a typical beam thermal resistance $R_{beam} = 9 \times 10^7$ K/W. Thus, we can safely consider the central platform in thermal equilibrium with the heater.

Finally, the response time of the temperature measurement has to be fast enough to follow the dynamics of the breaking process. This is characterized by the thermal time constant $\tau = R_{mems}C_{mems}$, where R_{mems} is the thermal resistance of the MEMS and C_{mems} the effective heat capacity. To minimize τ, we designed MEMS platforms with different dimensions, reducing it to the minimum size required to optically align the tip onto the MEMS. The smaller fabricated MEMS platforms are 62 µm ×17 µm including heater and gold platform, with a calibrated time constant $\tau = 20$ ms.

On the materials selection

As already mentioned, we chose low-stress SiNx to fabricate the supporting structure of the MEMS, Pt for the heater/thermometer and Au as metallic electrode to perform the STM-BJ measurement. SiNx is one of the most popular materials to build thin film mechanical resonators and in general suspended membranes on silicon. In our case, the combination of a large Young modulus (260 GPa) and low thermal conductivity makes it ideal to optimize the trade-off between mechanical stiffness and thermal insulation.

Platinum is also the most used metal to make high-precision thermometers (like the commercial standards Pt-100 and Pt-1000), because of the linearity of the electrical resistance over a wide temperature range, its inertness and durability. Another important characteristic of Pt thin films is the ability to sustain large current density up to 10^7 A/cm^2 [79] before electromigration sets in, and show high temperature stability of the electrical R(T) characteristic. On the contrary Au interconnects start to suffer from electromigration at current densities between 10^5 and 10^6 A/cm^2 [80]. To achieve heater temperatures of about 100 °C, we work at current densities $\sim 2 \times 10^5$ A/cm^2, and thus Pt seemed the optimum choice.

Gold was selected as the starting material for the metallic platform on the MEMS for several reasons. It is one of the most understood and well studied material with the STM-BJ technique in terms of conductance quantization[27, 15], atomic chain manipulation [26, 15] and formation of molecular junctions [31], thanks to its high bonding affinity with many organic molecules and different anchoring groups. Moreover, it is also very common in the fabrication of metal leads for micro and nanostructures, as it does not readily oxidize and has one of the highest electrical conductivity. However, the gold layer on the MEMS can be easily replaced by other metals. MEMS structures with Pt platforms were fabricated and tested in preliminary experiments during the PhD project. Other metals like palladium[81], silver [82, 83], nickel [84, 85] or even graphene [86, 87] had been already studied as suitable electrode materials for molecular electronics applications. Thus, it will be very interesting in the future to study the heat transport properties of atomic contacts and molecular junctions formed with different metals.

3.2.4 MEMS characterization

Before starting an experiment, the thermal and electrical properties of the MEMS samples have to be carefully characterized. Important parameters are the heater resistance at ambient temperature R_{4Pamb} and thermal coefficient of resistivity of Pt, for the temperature measurement, and the resistance of the metal line connecting the gold platform, for the electrical conductance measurement. Other parameters like the thermal time constant and the thermal resistance are important features but they do not enter in the data analysis.[2].

The temperature coefficient of resistance for metallic thin films are generally lower than the value for bulk metals (e.g. for platinum $\alpha = 3.72 \times 10^{-3}$ K^{-1} in bulk and 1.7×10^{-3} K^{-1} in thin films [88, 65]). This stems from the fact that the electrical resistivity increases when the film thickness reduces because of the additional surface scattering, defect density, etc. It was shown that α varies as a function of the thickness to electron mean free path ratio t/λ and of the degree of specularity of the scattering at the surface [89, 90]. It also depends on the impurity level, defect density and grain size of the polycrystalline film [91]. For this reasons, we usually measure the temperature coefficient of resistance for at least one MEMS device for every fabricated wafer, as we expect the Pt-film quality to be very similar for MEMS devices on the same wafer. To characterize α, we measure the electrical resistance of the heater as a function of temperature with a temperature calibrated setup. For this purpose, we place the sample on a copper plate in good thermal contact

---

[2] The thermal resistance of the MEMS, enters in the analysis only if the tip and the substrate are at different temperatures.

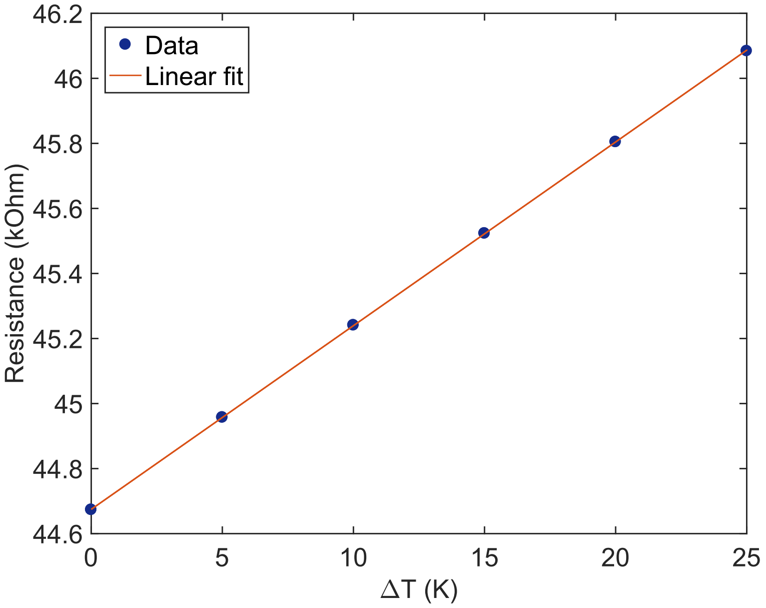

Figure 3.13: Calibration of the temperature coefficient of resistivity α of the Pt-heater. $\alpha = (1.26 \pm 0.01) \times 10^{-3}$ K^{-1} is determined from the slope of the resistance of the heater (in this case measured in a 2-probe configuration) versus temperature.

with a Peltier element, which is glued on a copper heat spreader. A silicone based thermal paste (HTSP, Electrolube) ensures a good thermal contact between the sample and the copper plate. A Pt100 (Class 1/3 B) is used as temperature sensor and it is glued on the copper plate holding the device. A temperature controller unit (Meerstetter TEC-1901) is then used to change and monitor the temperature of the sample, while measuring the electrical resistance of the heater with a 6 1/2 digits digital multimeter (Keithley2100). To reduce heating effects that may arise from the probing current of the multimeter, we perform the measurement at atmospheric pressure and use the 1 MΩ range of the multimeter with I = 5 μA. Figure 3.13 shows a typical resistance versus temperature curve between 25 °C and 50 °C. A waiting time of 5 min was used to let the temperature settle after the change in the PID controller and for every temperature the resistance was measured during both the heating and cooling cycle. Excellent match between the 2 curves is found ($\sim$ 0.1 Ω), confirming the accuracy in the temperature control. To extract the temperature coefficient of resistance we take a linear fit of the measured R(T) curve and use

$$\alpha = \frac{1}{R_0} \frac{\Delta R}{\Delta T} \tag{3.13}$$

where R_0 is the resistance intercept at $\Delta T = 0$ and the second term is the slope of the curve. In this way we obtain $\alpha = (1.26 \pm 0.01)$ K^{-1}. To calculate the uncertainty we used the script distributed by the Swiss Federal Institute of Metrology (METAS) [92] for the linear propagation of errors calculated from the datasheets of the instruments. However, because of variations from sample to sample we estimate an accuracy of about 1%. Among the different fabricated wafers, we observed variations of about 10%, by keeping the same nominal thickness and material quality. Interestingly, the ratio $\alpha_{bulk}/\alpha_{film}$ is usually very similar to the ratio in electrical resistivity

$\rho_{bulk}/\rho_{film} \approx 2.5$ to 3, as they are closely related [89].

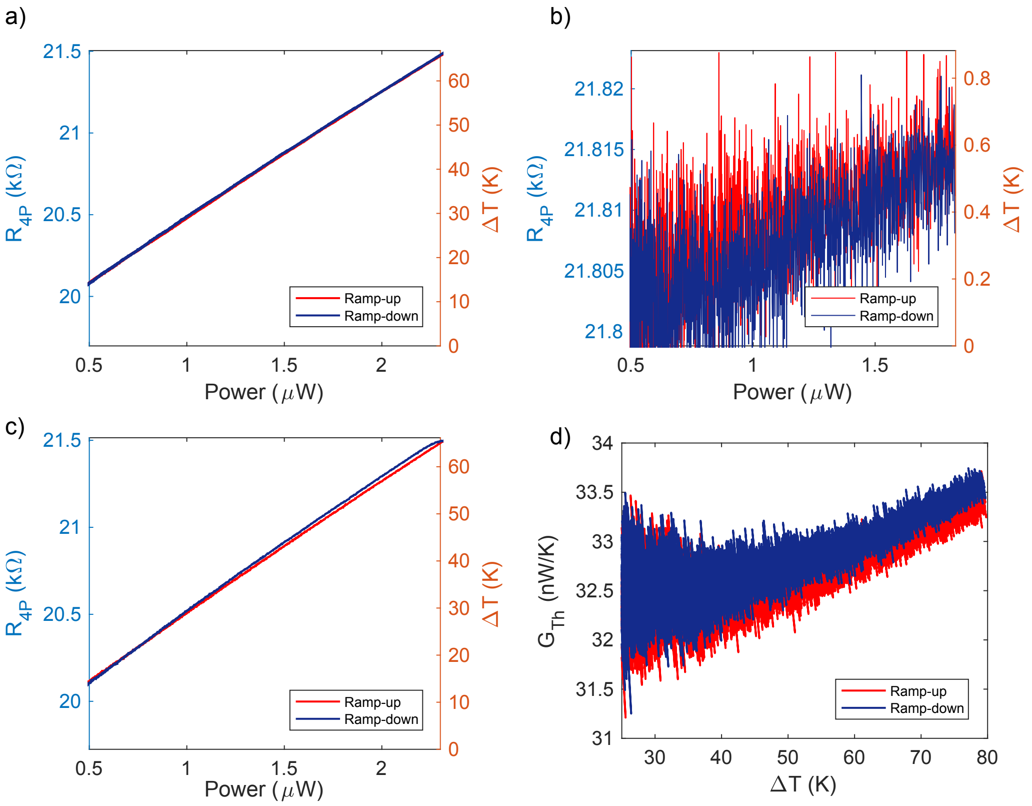

Figure 3.14: IV characteristics of several MEMS in different conditions. a) IV measured in high-vacuum (P $\sim 10^{-7}$ mbar) by ramping the voltage at 0.018V/s. From the linear fit we obtain a thermal resistance $R_{th} = 2.9 \times 10^7$ K/W. b) IV measured in air for a similar MEMS design. Because of air conduction, only negligible heating is observable over a power range similar to a). From the linear fit we obtain thermal resistance $R_{th} = 2.8 \times 10^5$ K/W. c) IV measured in vacuum. The speed of the voltage ramp is 0.18 V/s, 10 times faster with respect to a). Because of the thermal time constant, the MEMS cannot thermally equilibrate during the voltage ramp and a small hysteresis between ramp-up and ramp-down is visible. d) Thermal conductance of the MEMS versus ΔT measured with the heater.

Once the temperature coefficient of resistance is calibrated, we still need to measure the 4-probe resistance of the heater at room temperature R_{4Pamb} to obtain a functional thermometer. This can be readily achieved by measuring the IV characteristic of the heater in air or in vacuum. Figure 3.14. According to

$$R_{4P} - R_{4Pamb} = \alpha \times (T - T_{amb}) = \alpha \times R_{th} \times P \tag{3.14}$$

from the linear fit of the $R_{4P}(P)$ curve we can obtain R_{4Pamb} and R_{th} from the intercept at 0 and the slope, respectively. Many interesting features can be understood from this analysis. First, the thermal resistance of the MEMS drops by 2 orders of magnitude when measured in air, Figure 3.14b, showing the importance of performing the measurement in vacuum. Second, the thermal time constant of the MEMS sets a limit on the maximum speed of the voltage ramp. If the voltage ramp is too fast, the heater cannot thermally equilibrate, reaching a lower temperature with respect to equilibrium during ramp-up and a higher temperature during ramp-down, Figure 3.14c. By using equation 3.14, we assume that α and R_{th} are temperature independent. This holds well for α in the temperature range between 300 K and 380 K as confirmed with the independent calibration procedure. However, the thermal resistance presents a small temperature variation, which gives rise to a non-linearity of the IV characteristic. Figure 3.14d shows the thermal conductance calculated by dividing the power provided to the MEMS and the resulting ΔT, with a total increase of 1nW/K over a ΔT = 80 K. The thermal conductance of the MEMS $\mathrm{G_{mems}}$ is given by 3 main contributions: conduction through the silicon nitride beams, conduction through the Pt-lines on the beams and thermal radiation. The thermal conductivity of thin silicon nitride membranes depends on the deposition method used but it usually reaches a plateau around 300K [93, 94, 95], showing a very small temperature dependence. On the other hand, metals like platinum follow Wiedemann-Franz law [96], which states that electrical and thermal conductivity are proportional to each other

$$k_{th} = L_0 T \sigma \tag{3.15}$$

where L_0 is the Lorenz number and it is usually close to $2.44 \times 10^{-8}\ V^2/\Omega^2$ and σ is the electrical conductivity. From the measured electrical conductivity of the platinum lines at room temperature ($\sim 3.8\times10^6$ S) we can estimate the contribution of Pt to the thermal conductance of a single beam to be on the order of 1 nW/K and the one of SiNx around 7nW/K, with a corresponding thermal conductivity of 3.5 W/mK in agreement with previous reports [62, 73]. By assuming an average temperature of the beams $T_b = T_{amb} + \Delta T/2$ (strictly valid only for a linear temperature gradient) we can estimate an increase in thermal conductance of 13% at $\Delta T = 80$ K with respect to room temperature, corresponding to 0.5 nW/K. This does not explain the overall increase observed in Figure 3.14. Note also that a Lorenz number of $1.8\times10^{-8} V^2/\Omega^2$ was reported for Pt-nanowires [96] and that we did not consider the decrease in electrical conductivity with temperature; so an even lower value might be expected. As we will demonstrate in the next section, the contribution of the far field thermal radiation can be of a similar order of magnitude at $\Delta T = 80$K. Apart from the interpretation of the temperature dependence of $\mathrm{G_{mems}}$, it is noteworthy to mention that during the STM-BJ experiment on the MEMS, the total ΔT varies by only few degrees, from closed to open contact. Therefore, within a small temperature range we can safely consider that $\mathrm{G_{mems}}$ remains constant.

In practice, we perform these IV measurements regularly before and after the experiment. This allows us to keep track of the heater resistance at room temperature R_{4Pamb} and correct for small drifts that may appear by continuously heating the MEMS.

Radiation contribution

To estimate the net power P emitted by radiation when the MEMS is heated to a certain temperature T_H, we can use the Stefan-Boltzmann law valid in the far field limit [97, 98]

$$P = A\epsilon\sigma(T_H^4 - T_{amb}^4) \tag{3.16}$$

where $\sigma \simeq 5.67 \times 10^{-8}\ \mathrm{Wm^{-2}K^{-4}}$ is the Stefan-Boltzmann constant, A is the surface area of the MEMS, ϵ is the emissivity, which depends on the material and

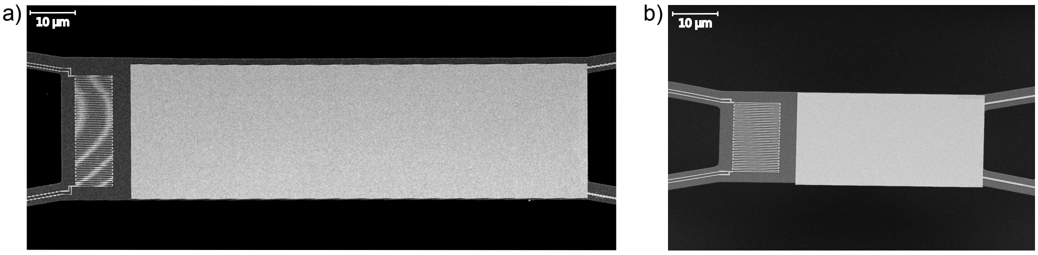

Figure 3.15: MEMS designs with different sizes. a) Area = $112 \times 32 \mu m^2$, with a measured thermal time constant $\tau = 43$ ms and a thermal resistance $R_{th} = 2.9 \times 10^7$ K/W. b) Area = $62 \times 22 \mu^2$, $\tau = 22 ms$, $R_{th} = 2.9 \times 10^7$ K/W.

wavelength radiation λ, and T_{amb} is room temperature. The emissivity of silicon nitride membranes decreases with thickness while for metals like gold the opposite trend is generally observed. In our case, for $\mathrm{t_{SiNx}} \approx 150$ nm and $\mathrm{t_{Au}} \approx 50$ nm, we can estimate the emissivity for both materials to be $\epsilon \approx 0.02$ [99]. Similar values can used for Pt [100], so that the MEMS can be treated as an homogeneous medium with emissivity $\epsilon \approx 0.02$. For an estimation of the order of magnitude, we can consider only the contribution of the central part of the MEMS, which is the one at a higher temperature, with an area $A = 2728$ µm^2 for the MEMS designs used in Figure 3.14. In this way we obtain an emitted power $P \approx 38$ nW for $T_H = 375$ K and $T_{amb} = 295$ K, corresponding to an increase in thermal conductance $G_{rad} = P/(T_H - T_{amb}) = 0.45 nW/K$. Compared to the total thermal conductance of the MEMS $G_{mems} \approx 33$ nW/K, we can conclude that, in the temperature range we are interested ($T_H \leq 400$K), heat conduction through the suspension beams dominates. However, G_{rad} contributes partially to the temperature dependence of G_{mems} observed in the IV-characteristics measured in vacuum. Note that the MEMS is suspended by at least 20 µm above the substrate after the underetching process, which is greater than the peak wavelength $\lambda_{max} \approx 10$ µm of a blackbody at T = 300 K. In fact, near field enhancement of heat transfer comes into play only at distances below λ_{max} [78]. For this reason, we can exclude near-field effects contributing to the thermal conductance of the MEMS.

Thermal time constant

The thermal time constant of the MEMS τ defines the minimum time required for the Pt thermometer to equilibrate. All the events occurring on a shorter time scale are low-pass filtered by the response of the heater. Using a lumped capacitance model, we can estimate $\tau = R_{th} C_{th}$, where C is the heat capacity of the MEMS platform. Following this criterion, we fabricated different designs reducing the size of the central platform and keeping the same thermal resistance, Figure 3.15. In order to characterize the thermal time constant, we apply a voltage step to the heater in vacuum, which translates in a fast transition of the input power, and measure the temperature/resistance transient. The time constant can then be extracted by fitting the resistance versus time curve with the low-pass filter response of an equivalent electrical RC-circuit

$$R(t) = Ae^{(-t/\tau)} + R_{\mathrm{inf}} \tag{3.17}$$

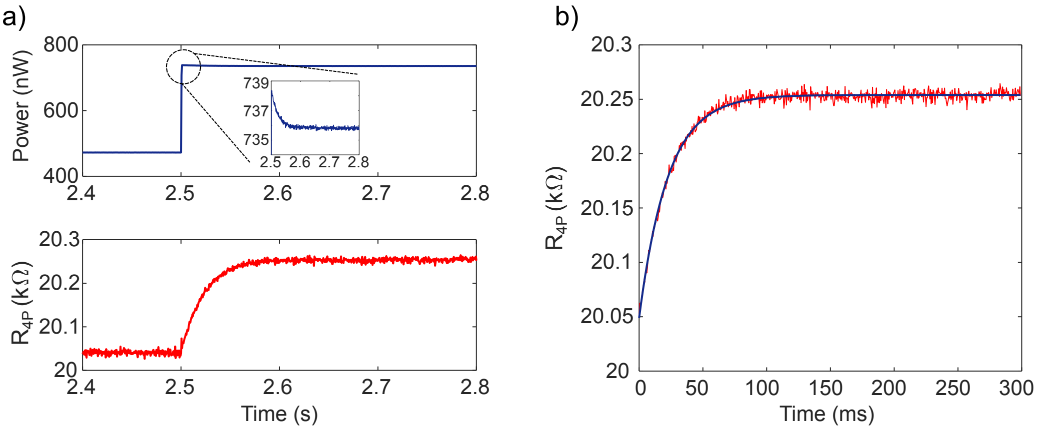

Figure 3.16: Measurement of the thermal time constant of the MEMS by applying a voltage step to the Pt-heater. a) Power step (blue) and resistance transient (red) versus time. The inset, shows the small transient in the power step because of the resistance change. b) Exponential fit of the resistance transient to extract the thermal time constant $\tau = 23$ ms.

where R_{inf} is the saturating value of the resistance after the transient, Figure 3.16. With this method we could experimentally verify that the time constant scales with the area of the MEMS platform with smaller steps with respect to the predictions of the simple lumped model. In particular, for size ratios of 2.6 and 3.4 we obtain a time constant ratio of 2 and 2.2, showing that at small dimensions (20×60 µm), the contribution of the supporting beams to the total heat capacity start to be relevant. The minimum size that we can actually use is limited by the optical access to the setup. At the moment, before starting the experiment we coarse align the tip to the MEMS by looking at a grazing angle with a stereo microscope placed outside of the vacuum chamber with a maximum magnification of 150. For this reason, the smallest MEMS that permits a fast and reliable tip alignment is 17×62 µm with a time constant $\tau = 19$ ms. The inset of Figure 3.15a shows a zoomed view of the power step applied. As the resistance of the heater changes with temperature, the power provided to the MEMS slightly adjusts with it. However, such overshoot is less than 1% of the power step applied and therefore negligible. The fact that the thermometer is not as fast as the electrical signal (limited only by the bandwidth of the transconductance amplifier) results in a time delay between the observed events in electrical conductance and the corresponding features in the thermal. More importantly, the atomic or molecular junction has to be kept stable for at least one time constant, in order to measure an accurate thermal conductance.

3.3 Sample preparation

Measuring the charge transport properties of single molecules with STM-BJ requires clean metal surfaces (usually gold), deposition of sub-monolayers of the target molecules and clean measurement environment. In this section, the tip and sample preparation procedures are explained, starting from the cleaning of the gold surface, to the deposition of organic molecules and electrochemical etching of metallic tips.

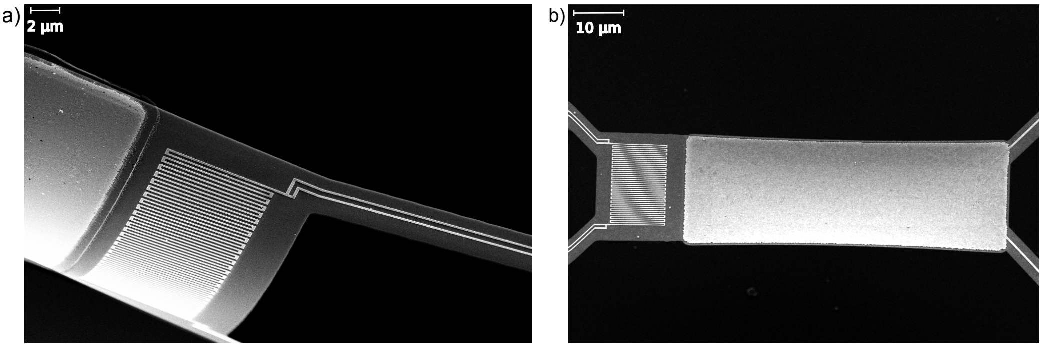

Figure 3.17: SEM pictures of MEMS devices damaged during the cleaning process. a) After flame annealing with butane flame. b) After strong H_2 plasma.

3.3.1 Cleanliness of the gold platform on the MEMS

The concept of ″clean surface″ can take several meanings depending on the research field. In surface science, single crystal metallic substrates are usually employed to perform imaging with sub-atomic resolution of organic molecules deposited on the surface. Moreover, experiments are carried out in UHV and at cryogenic temperatures to maintain the system in a controlled environment [101, 102]. A typical cleaning procedure consists of several sputtering cycles with noble gases followed by an annealing step at high temperature (600 °C) to form an atomically flat surface. After this preparation process, molecules are deposited in-situ by thermal evaporation or electro-spray deposition.

For break junction experiments such ultra-clean conditions are not strictly necessary. A large variety of different experimental conditions were used to study charge transport in single molecular junctions, from UHV [39, 103] to solution [37, 104] and even ambient conditions [105, 106]. However, the cleanliness of the metallic electrodes has to be optimized to enable the efficient deposition of molecules. Standard procedures involve the use of freshly deposited metallic thin films on different substrates (e.g. glass, mica, silicon), which can then be further cleaned by flame annealing with an hydrogen or butane flame before deposition [107].

In our case, the MEMS have undergone a series of patterning steps during fabrication in the cleanroom and resist residues and other forms of organic contaminants can be present on the gold platform. We were also looking for a cleaning process to use devices which have been stored in ambient conditions for several months, in order to maximize the number of available samples after each fabrication run. The cleaning of suspended MEMS structures is very challenging. Standard cleaning procedures cannot be readily applied as overheating and surface tension of solvents may irreversibly damage the samples. Figure 3.17 shows two MEMS devices that were overheated during flame annealing (a) and H_2 plasma (b) cleaning, presenting a deformed central platform.

Several cleaning procedures were tested during the PhD project. To test the efficacy of a cleaning step, we normally performed STM-BJ measurements on the MEMS and look at the thermal signal. In fact, adsorbates on the surface of the MEMS or of the tip provide an additional heat path which results in a thermal jump to contact when approaching the tip. Although, this is practically unavoidable in high vacuum and without in-situ sample preparation capabilities, the magnitude of the thermal conductance of such parasitic contact is directly connected to the cleanliness of the junction formed. As next step, we could then deposit the target molecules and perform standard STM-BJ to verify the occurrence of molecular plateaus in the electrical conductance traces.These tests were carried out on a patterned gold pad on the substrate close to the underetched region, to exclude the influence of the MEMS mechanics.

At the very beginning, we tried to improve the cleanliness of the gold platform by heating the MEMS under high-vacuum above 100 °C, but in most cases it was not effective. For measurements with Au-Au contacts, good cleanliness conditions were achieved with both UV-Ozone and O_2-plasma. In the first case, the samples were exposed to UV-Ozone for 5 to 30 minutes [108, 109]. The main advantage is that, being a dry process performed at atmospheric pressure, the problems of stiction and overheating can be avoided. UV excitation converts molecular oxygen to ozone and atomic oxygen. These are strong oxidizing agents and can decompose UV excited organic contaminants to volatile groups such as CO, CO_2,N_2, etc. that can desorb. O_2-plasma cleaning is another very common technique used in microfabrication to remove organic residues [110] or even covalently bonded self-assembled monolayers [111]. During the process, the chemical action of free radicals and metastable oxygen species (O_2^+, O_2^-, O_3, O, etc.) and the generated UV radiation adds to the physical ablation by energetic electrons and ion bombardment. Usually, it requires low pressure (1 mbar) and it can result in substantial heating of the substrate because of the absorbed power. During the tests carried out, we did not observe visible overheating effects of MEMS samples up to plasma powers of 600 W for several minutes. Indeed, thanks to the small size of the chip (5×5 mm) and the MEMS ($\sim$ few 1000 μm), only a negligible fraction of the plasma power is absorbed. Typically we set 400 W for 5 minutes as standard recipe.

It is well known that gold oxides form after the exposure to a strong oxidizing atmosphere like UV-Ozone [109] or O_2-plasma [112]. This can be easily observed by checking the hydrophilicity of the gold surface: aged gold is usually hydrophobic because of the carbon based contaminants, while gold oxide is hydrophilic. Gold oxide is intrinsically unstable and decomposes spontaneously under ambient conditions but it can also be reduced by ethanol oxidation. For Au-Au break junction measurements on the MEMS, we did not observe any particular influence of this rinsing step. However, these two simple methods were found to be insufficient for the self assembly of organic molecules, even with thiol anchoring groups. After several attempts, we decided to utilize an ion milling process to take advantage of the physical action of the ion bombardment and remove any contaminants independently of the chemistry. Typically, we use Ar-ion milling with a beam current of 150 mA (with beam diameter of 30 cm) for 20s at an angle of 20°C with respect to the perpendicular to the beam direction. With these conditions we etch about 5 nm of Au and 3 nm of Pt, corresponding to an increase of $\approx 10\%$ in heater resistance. With a typical beam energy of 500 eV we can estimate that a power of about 1 μW is released to the MEMS resulting only in moderate heating. This additional cleaning step revealed to be very critical for the reproducible formation of molecular junctions on the MEMS.

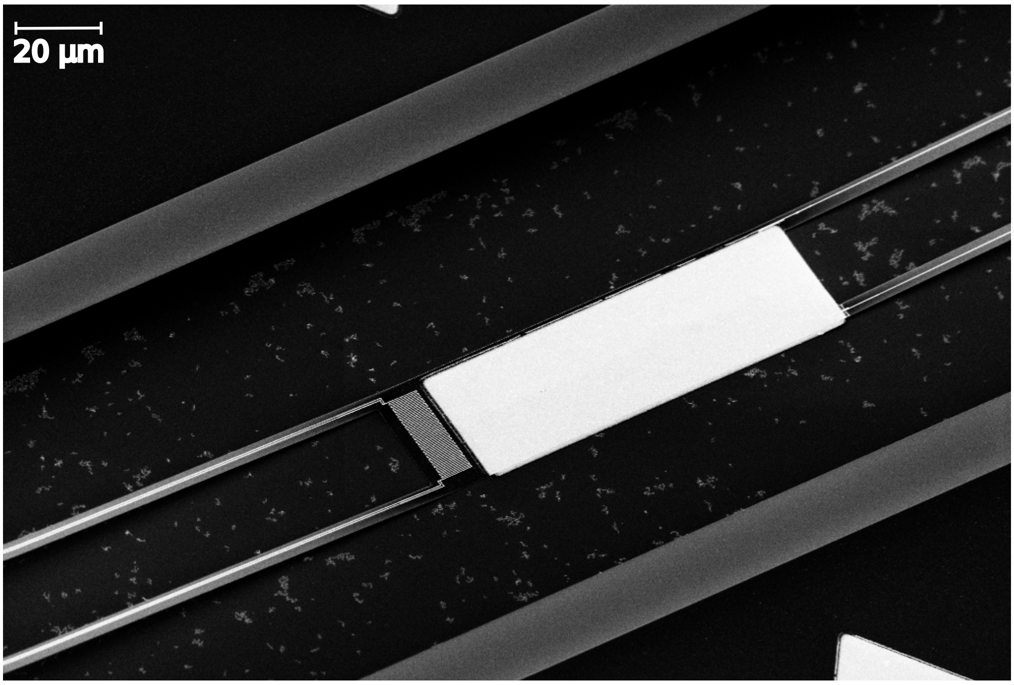

Figure 3.18: SEM picture of a collapsed MEMS because of stiction.

3.3.2 Gold surface functionalization

The most common methods to functionalize metallic surfaces with organic molecules is by direct deposition from solution or by drop casting. In the first case, the sample is immersed into a liquid solution containing the target molecules for a specific time interval while in the second, a droplet of solution is casted onto the sample and let to spontaneously evaporate. Deposition from solution is widely spread also in the community of molecular electronics, mainly because of its ease and versatility. However, suspended MEMS structures like the ones used in this work are very sensitive to external forces and in particular, capillary forces developing during the drying of the solvents. This well known problem in surface micromachining is called stiction [113, 114]. To avoid this issue, we typically use critical point drying during fabrication to release the MEMS, which is not applicable for the molecular deposition. Figure 3.18 shows an example of MEMS device that collapsed after drop casting the molecular solution. Even if electrically these devices can still function, detaching the platform from the bottom of the cavity with a micro-manipulator is possible but tedious and with a high probability of irreversibly damaging the MEMS.

A better option is to reduce the size of the droplet to fit the MEMS platform by using a glass capillary. Such capillaries can be manually fabricated by pulling around an heated region until the glass breaks. Hollow tips with few tens of μm in diameter are then filled with the target solution and mounted onto a modified tip holder. After aligning the capillary onto the MEMS with the piezo-positioners, a droplet of solution can be deposited by gently touching the gold surface. As the droplet does not wet the back side of the membrane, stiction cannot occur during the evaporation of the solvent. This method was successfully tested on few samples

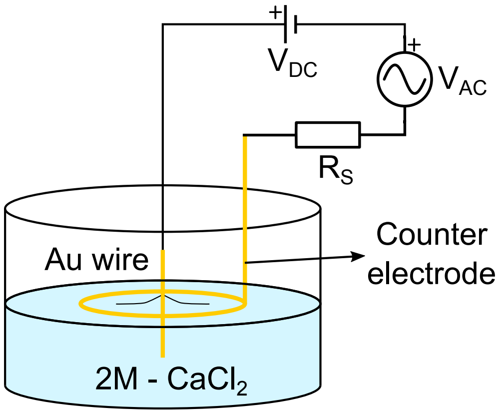

Figure 3.19: Schematic of the etching setup used to fabricate gold tips.

and the first electrical measurements of molecular junctions could be done. However, direct evaporation of the solution leaves residues on the MEMS surface, which can completely dominate the heat transport to the tip.

Finally, immersion in solution turned out to be the best approach. Since stiction occurs during the evaporation of the solvent, as long as the chip surface is covered by liquid the MEMS is safe. Therefore, we can dip the sample in solution and rinse it several times in clean solvent to remove physically adsorbed molecules. By carefully drying the sample with the N_2 gun we can then avoid stiction and reduce the amount of residues. The drying process remains a critical step, but MEMS designs with angled beams demonstrated to be robust in this respect. The best way to obtain clean samples after the deposition process consists of mixing the molecular and rinsing solutions with low vapor pressure solvents (e.g. ethanol), to slow down the spontaneous evaporation. This deposition method allows us to follow the standard protocols for the formation of self assembled monolayers on gold [115, 11] and to be flexible in terms of molecules that can be studied. Typically, we use solutions with concentrations of 0.1 to 1 mM and deposition times between few seconds to 2 hours, to have a good probability of contacting molecules during the break junction experiments.

3.3.3 STM tip preparation

Since the invention of the STM, sharp metallic tips with radius on the order of few tens of nm were prepared by electrochemical etching [116]. Typically, stiff metals like tungsten or alloys of platinum-iridium (e.g. Pt90%-Ir10%) are used to ensure high endurance and mechanical stability of the tip. Gold, even though less stable, is often the material of choice for tip enhanced raman spectroscopy because of their strong plasmonic resonances and resistance to oxidation in ambient conditions.

For STM-BJ measurements, manually cut tips made out of gold are typically used. Taking advantage of the ductility of gold, atom size contacts can be formed by repeatedly crashing the tip into the substrate, without the need of special fabrication steps. However, for heat transport measurements, the size of the tip apex determines the magnitude of the parasitic contact formed with the adsorbates on the MEMS surface. To reduce the contribution of the adsorbates to the thermal conductance of the junction, nanometer size tips with a well defined shape are necessary. For this

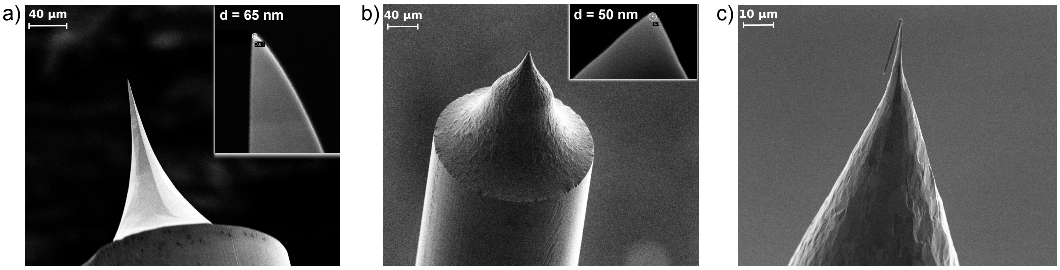

Figure 3.20: SEM images of electrochemically etched gold tips. a) Au wire flame annealed before etching. b) Au wire not flame annealed. c) Bent tip because of the high aspect ratio.

reason, we usually fabricate tips by electrochemical etching. This section focuses on the fabrication of gold tips, which are used in for the experiments in chapter 4 and 5. Recipes with other metals (Pt, Pt-Ir and W) are described in the appendix B.

Among all the different methods described in literature [116, 117, 118, 119], we decided to adopt the method described by Boyle et al. [120] as they could achieve minimum tip radius of about 10 nm with a chemically safe two step etching method. Figure 3.19 shows a schematic of the electrochemical etching setup used. A piece of gold wire of 0.25 mm diameter with 99.99+% purity (GoodFellow) is immersed by 1-2 mm in a 2 M solution of $CaCl_2$. An alternating voltage with a tuned DC offset is then applied between the Au wire and the counter electrode to start the etching process. Typically, the counter electrode is made out of Au or Pt with 1 mm diameter arranged in a loop around the tip wire. Good results can also be obtained by using graphite rods with 99.99+% purity. The alternating voltage source, consisting of a custom-built signal generator, is set to 6-8 V peak-to-peak with a frequency of 300 Hz and a suitable DC offset of 3.5-4.5 V ensures that the tip wire remains at a positive polarity. To observe the evolution of the etching, we usually check the current flowing in the electrochemical cell by measuring the voltage dropping over a small series resistance $R_s = 50\ \Omega$. With these parameters, tip with radius of about 20 to 50 nm can be fabricated in a single etching step without drop-off within 3 minutes, Figure 3.20. As a final step, the tip is rinsed in DI water in an ultrasonic bath to remove residues formed during the process. If the gold wire is flame annealed until the melting point before the etching, crystalline planes are visible along the tip cone presenting a smoother surface, Figure 3.20a. Tips with a long tapered structure are usually discarded, as they result mechanically unstable and easily bendable, Figure 3.20c. The electrochemical etching is quite sensitive to different parameters. As described in [120], the frequency of the alternating voltage influences the final tip shape and the etching speed. In particular, we observe a net decrease in current when the frequency overcomes a threshold (around few kHz), which results in etching rates greater than 15 minutes with the formation of a truncated tip cone. Another important aspect is the current flowing between the tip and the counter electrode. This depends on the external circuitry, which should not have intrinsic current limits, and the amount of ions present in the solution, which changes over time. So typically, a fresh $CaCl_2$ solution is used to fabricate 5 tips with good reproducibility.

The main advantage of this procedure is that tips with a good yield (80%) can be fabricated in a relatively short time without the need of feedback circuit to switch-off the current at the end of the etching step or a 2 steps process involving the coating of the final part of the Au wire with varnish. Modifications of this process have often given less reliable results and lower yields. However, further investigations to reduce the bubbling at tip interface and tune the angle of the tip cone may be beneficial. The detailed etching recipe is presented below. **Back electrode:** Gold loop

Electrolyte: 2M $CaCl_2$ (dihydrate, 99% purity, Sigma Aldrich) in deionized water

1. Cut about 1 cm of 0.25 mm gold wire and fix it to the tip holder.
2. (Optional) Flame anneal the tip of the wire for 1-2 s using a flame torch until a gold sphere forms at the tip.
3. (Optional) Coat the apex (1-2 mm) with varnish, to protect it during the etching as in a drop-off method.
4. Place the gold loop just below the surface of the electrolyte around the gold wire.
5. Immerse the wire by about 1-2mm into the electrolyte (make sure that the coated portion of the wire is fully immersed into the solution).
6. Apply an AC voltage V = 8 V peak-to-peak at 300 Hz with a DC offset of 4.5 V. The etching takes about 3min.
7. Rinse tip in DI water and ultrasonic bath for 30 s
8. Dry tip with N_2

Chapter 4

Metallic Quantum Point Contacts

Single atom junctions pose the ultimate limit to the scaling of electrical contacts[31]. They serve as model systems to probe electrical and thermal transport at the atomic level and investigate quantum effects occurring in one-dimensional systems[15]. Charge transport in atomic junctions has been studied intensively in the last two decades [15, 26, 23, 27]. However, heat transport remains poorly characterized because of significant experimental challenges. Specifically the combination of high sensitivity to small heat fluxes and the formation of stable atomic contacts has been a major hurdle for the development of this field. This chapter collects the experimental results on the heat transport properties of atomic contacts. Thanks to the simultaneous measurement of charge and heat transport we could observe for the first time that the direct proportionality of electrical and thermal conductance, quantized with the respective conductance quanta [50]. These measurements constitute an atomic scale verification of the well-known Wiedemann-Franz law [121] and are summarized in our recent publication [122]. Few weeks after the article was released, the results were independently confirmed by Cui et al. [69]. In this chapter, we extend the content of the publication showing recent measurements with improved accuracy and explore the effects of different tip materials and adsorbed molecules on the gold surface. The experiments with different tip materials on gold were performed by Alyssa Prasmusinto during her master thesis, under the supervision of Dr. Bernd Gotsmann and myself.

4.1 Gold-gold contacts

Atomic quantum point contacts represent an ideal platform to investigate heat transport in which quantum confinement effects cannot be neglected. The development of experimental techniques, such as scanning tunneling microscopy (STM) and mechanically controlled break junction (MCBJ) enabled the formation and manipulation of monoatomic metallic chains [15, 26, 23, 27]. More recently, Joule dissipation [60, 58] and thermoelectric effects [123, 124] have been successfully probed. Heat dissipation was measured in current-carrying single gold-gold contacts by means of STM with an integrated micro thermocouple in the tip [58]. It was shown that heat dissipates symmetrically into the two contacts, confirming that the electron transmission function T(E) of the junction element around the

Fermi energy E_F of the metallic contacts governs this phenomenon[59]. In fact, these current induced heating effects are directly related to the thermopower S of the junction, which is proportional to the derivative of T(E) at E_F. For atomic gold contacts S was determined to be very close to zero (S $\sim$ -1 μV/K) [124], in agreement with the relatively energy independent transmission function T(E) calculated with DFT methods.

As already introduced in chapter 2, the electrical conductance in atomic junctions is quantized. A single gold atom contact has a conductance equal to the quantum $G_0 = 2e^2/h$, where e is the electron charge and h Planck's constant. The Landauer approach used to describe charge transport can also be applied to heat transport [41], and predicts the validity of the Wiedemann-Franz (WF) law, which states that the thermal conductance G_{th} and the electrical conductance G_{el} are proportional to each other,

$$G_{th} = LTG_{el} \tag{4.1}$$

where T is the absolute temperature of the contact and the proportionality factor L, called the Lorenz number, assumes the universal Sommerfeld value $L_0 = 2.44 \times 10^{-8}$ V^2/K_2. The WF law applies to systems in which heat is predominantly transported by electrons and holds to a good approximation when the relaxation times for momentum and energy are the same (the scattering mechanism affects both momentum and energy transport at the same way) [125, 126]. This is largely valid for bulk metals at high and low temperature with variations of the Lorenz number lower than 10% with respect to the Sommerfeld value [127]. Verification of the WF law for metallic nanostructures, however, has proved to be difficult. Both enhancements [128, 129] and reductions [96, 130] have been reported for different metals (Au, Pt, Ni, Si..) in thin films and nanowires by using different experimental techniques, debating its general validity. Marked deviations from WF law can occur when electrons are physically confined in 1D systems, in which the Fermi-liquid state is replaced by a Tomonaga-Luttinger liquid state [131]. Owing to 1D confinement of electrons, spin-charge separation occurs, enabling scattering mechanisms to affect charge and heat transport independently. It has been experimentally demonstrated recently that isolated monoatomic gold chains on surfaces host such a Tomonaga-Luttinger liquid state[132]. Although atomic junctions are well described by the Fermi-liquid theory, no experimental demonstration on the validity of WF at this scale was reported at the time of the experiment. Most heat transport measurements in metallic ballistic systems came from 1D channels defined in 2D electron gases at low temperature [133, 134]. Metallic quantum point contacts allow similar phenomena to be studied at room temperature, because of the larger energy spacing between the available conductance channels.

Using the experimental technique explained in chapter 3, we measured simultaneously the thermal and electrical conductance of atomic gold junctions at room temperature. Figure 4.1 shows an example of an opening trace, measured at V = 50 mV. In Figure 4.1a we observe that the initial gold-gold contact is made of few atoms with an electrical conductance of about 6 G_0. When increasing the separation distance between tip and MEMS, the gold contact shrinks and the electrical conductance decreases in a typical step-like fashion characteristic of the 1D ballistic transport regime. In particular, the plateau at around 1 G_0 indicates the formation of a single atom contact. After breaking the contact (at about 4.5 nm), the tunneling regime sets in. In Figure 4.1b the thermal conductance follows

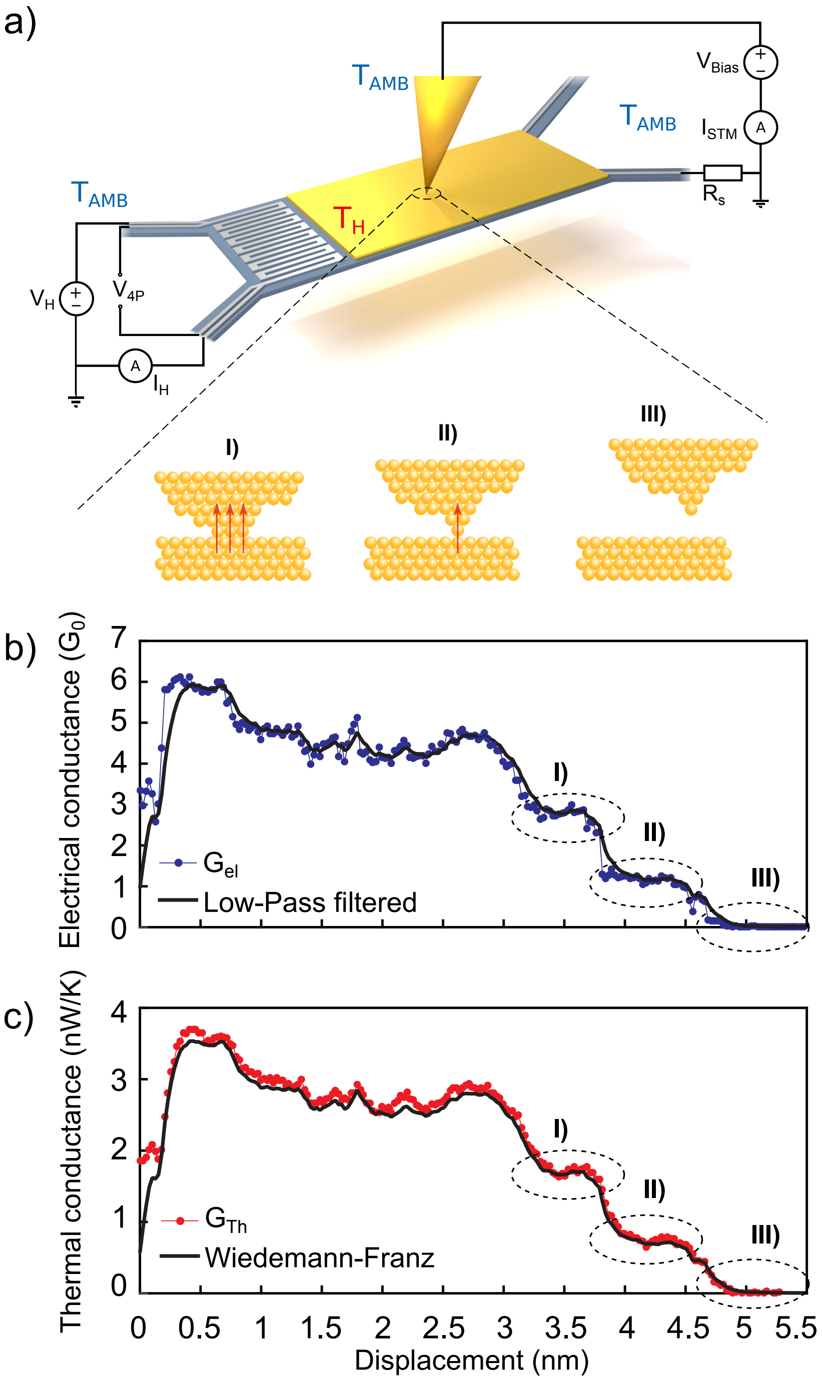

Figure 4.1: Thermal and electrical conductance of Au-Au contact during the breaking process. a) Schematic of the junction breaking on the MEMS. b) The black line has been calculated by digitally low-pass filtering the electrical signal (blue) with the thermal time constant value τ = 30 ms from calibration. c) Thermal conductance and Wiedemann-Franz law. The sampling time was set to 10 ms and the tip was retracted with an angle of about 25 deg with respect to the gold surface and a speed of 3nm/s. ΔT ranges from 41.5 K to 43.6 K, from closed (6 G_0 to open contact, respectively).

the same trend of the electrical conductance trace showing quantized steps with amplitude proportional to the number of atoms in the junction and characteristic delay given by the thermal time constant of the MEMS ($\tau = 30$ ms for this design). Indeed, by applying a digital low-pass filter to the electrical signal with a similar τ we can recover the thermal time response to step features. Using Wiedemann-Franz law with an average junction temperature of $T = (T_H + T_{amb})/2$, we can convert the electrical into thermal conductance and compare with the measured data finding an excellent agreement, Figure 4.1b.

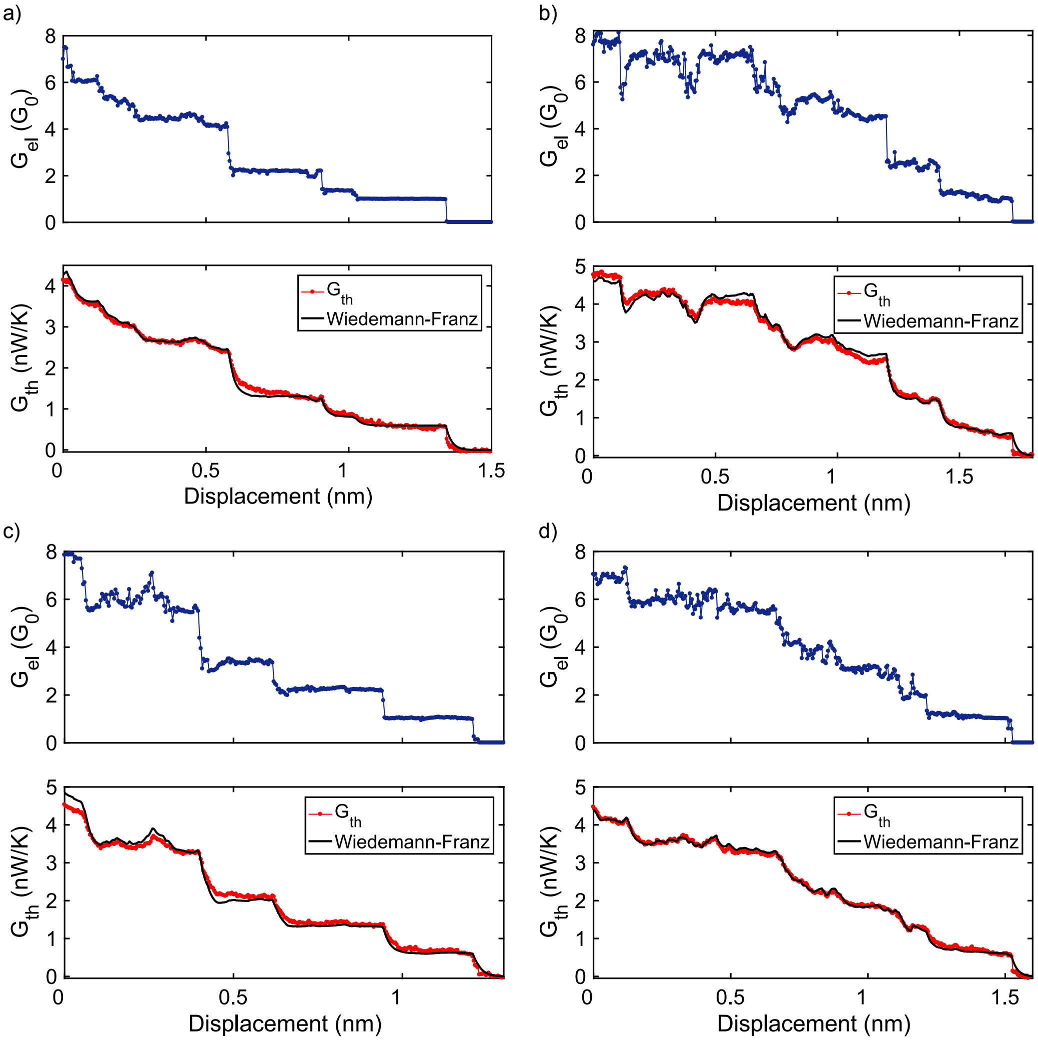

Figure 4.2: Single opening traces for Au-Au junctions measured on a different MEMS sample. Traces measured at V = 40 mV with R_s = 12.7 kΩ, average temperature difference is ΔT = 40 K. The sampling time was set to 2 ms and the thermal time constant of the MEMS was calibrated to be 20 ms. The sample was moved at 30° with respect to the tip axis at a speed of 4 nm/s along the pulling direction.

Further examples of single traces measured on a different MEMS sample are presented in Figure 4.2. Interestingly, the agreement between electrical and thermal conductance according to the Wiedemann-Franz law does not seem to depend on the

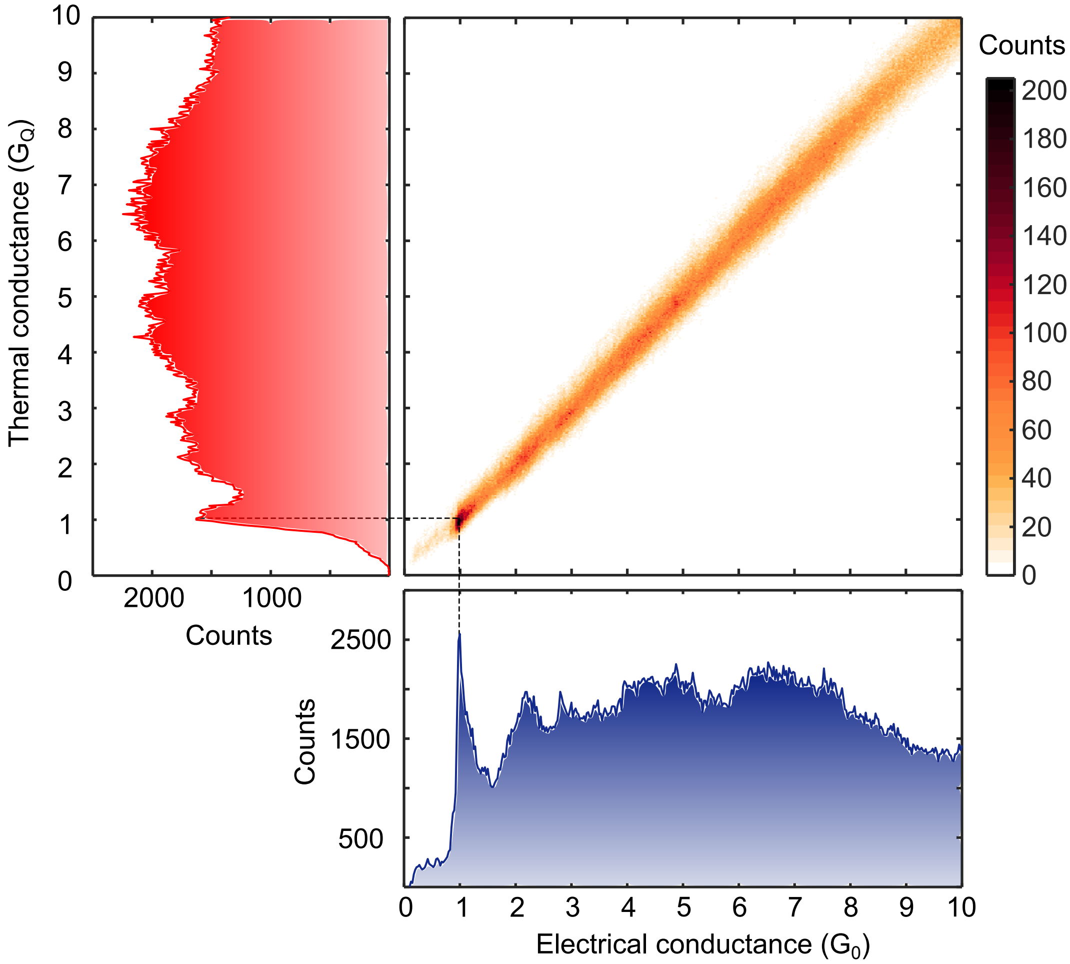

Figure 4.3: 2D histogram of thermal versus electrical conductance with respective projections onto 1D histograms. The thermal conductance has been normalized by the thermal conductance quantum G_Q= L0 TG_0. The thermal and electrical 1D histograms are built with a linear binning and a bin size of 0.025 $G_Q$and 0.025 G_0, respectively.

microscopic details of the junction, as gradual or more step-like necking processes show very similar results. Moreover, single atom plateaus with lengths greater than 0.5 nm (Figure 4.2a-c) along the motion direction are observed in 10% of the traces in the best datasets, which may indicate the formation of monoatomic chains [27]. Experiments at low temperature would enhance the thermal and mechanical stability of the junctions so that histograms of the G_0 plateau lengths could confirm the formation of atomic chains [26].

To study the evolution of the thermal versus electrical conductance, we repeat the break-junction experiment and collect few thousands traces to build two-dimensional (2D) histograms, correlating the thermal with the charge transport data as shown in Figure 4.3. The 2D histogram has been built from 2000 traces (examples in Figure 4.2) without trace selection. The sample was cleaned with oxygen plasma (400 W for 3 min) before the release of the MEMS and stored under argon atmosphere for about a month. In order to more easily compare the result with the Wiedemann-Franz law, we normalized the thermal conductance by the quantum corresponding

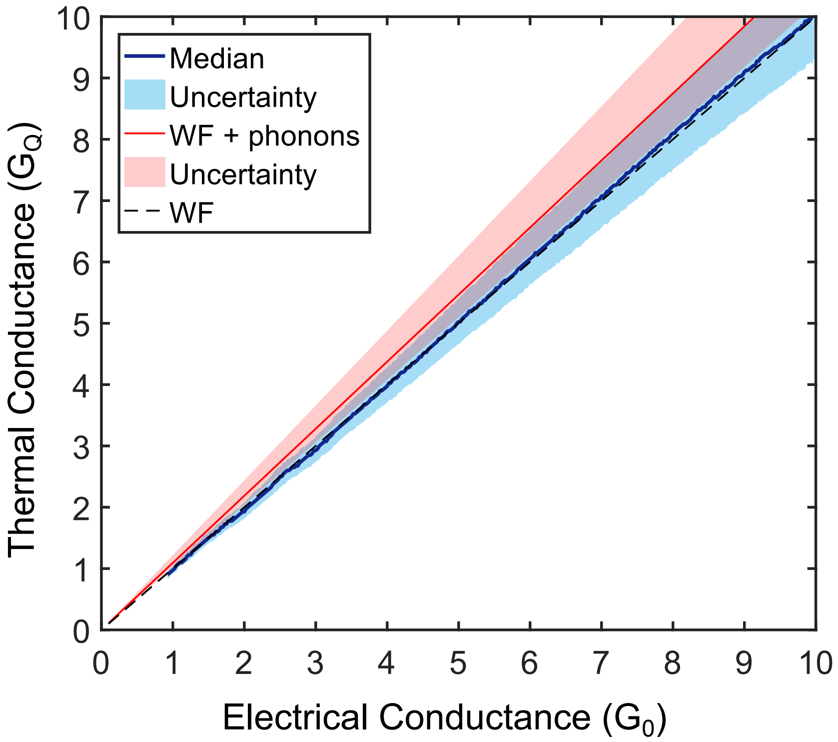

Figure 4.4: Comparison between experimental results and theoretical predictions. The thermal conductance signal has been normalized by the thermal conductance quantum for a single electron channel $G_Q = L_0TG_0$, where $T = (T_{amb}+T_H)/2$ is the average contact temperature. The dashed black line represents the electron contribution as predicted by the WF law, where the red continuous line takes also the phonon contribution to heat transport through the quantum point contact into account. The shaded areas represent the uncertainty regions.

to a single open electron channel

$$G_Q = L_0TG_0 = 2 \times \frac{\pi^2 k_B^2 T}{3h} \tag{4.2}$$

where k_B is Boltzmann constant, h Planck constant and T the average temperature. The second term can be readily obtained from the definitions of the Lorenz number $L_0 = \frac{\pi^2 k_B^2}{3e^2}$ and the electrical quantum of conductance $G_0 = \frac{2e^2}{h}$ and corresponds to the double of the thermal conductance quantum [48, 135], because of the spin degeneracy of an electron channel, see section 2.2. While the 2D histogram confirms the validity of the Wiedemann-Franz law for a single and a few gold atoms contacts, the corresponding 1D histograms demonstrate that thermal and electrical conductance are quantized. In particular, a prominent peak at one conductance quantum appears in both plots.

In Figure 4.4, we plot the thermal versus the electrical conductance extracted from the median of the 2D histogram. Experimental uncertainties and systematic errors are included, taking into account the offsets of the analog-to-digital and digital-to-analog converters, the amplifier gains, Seebeck voltages and the temperature dependence of the series resistance. The measured thermal conductance comprises the contribution of all heat carriers including electrons, phonons and radiation: $G_{Au} = G_{electrons} + G_{phonons} + G_{radiation}$. The contribution of radiation between two gold surfaces [136, 137, 70, 138] is weak and it is expected to be negligible. However, this may still reach non negligible values depending on the exact local geometry of the tip and surface around the junction, appearing as a distance dependent thermal conductance signal in the tunneling regime, see 4.1.4.

The phonon contribution to thermal conductance $G_{phonons}$ can be estimated from existing models for both single atomic contacts and larger Sharvin-type contacts, albeit with significant uncertainty. The scaling with contact size should be proportional to the electrical conductance in a situation where both charge and phonon transport is in the ballistic regime. We take into account phonon contribution between the bounds 2 and 22% of the WF law (see 4.1.1). Comparing now the prediction of the WF law and the phonon contribution with our experimental data, we find quantitative agreement within the respective uncertainties. While the experimental sensitivity in principle falls within the range of the expected phonon contributions, the overall uncertainty of the total G_{Au} does not allow an accurate investigation of the phonon transport. Taking into account the scatter of the data and the systematic errors, we can obtain an upper bound for the phonon contribution of 10% for a single atom contact. This results indicate that even by changing from diffusive to coherent ballistic transport, the phonon contribution to the thermal conductance remains similar to the bulk case [16]. As the phonon thermal conductance is expected to be constant above the Debye temperature of gold (T_D = 165 K [127]), experiments at variable temperatures may be an interesting tool for disentangling phonon and electron heat transport. More details about the estimation of the phonon contribution to the thermal conductance are provided in the next section.

4.1.1 Phonon contribution to the thermal conductance

In Figure 4.4, we plot the phonon contribution to heat transport for different values of the electrical conductance. Although the contribution of phonons falls within the experimental uncertainty, it is valuable to provide an estimate according to the theories and models available. While in bulk metals, the phonon thermal conductivity reaches values of only 1% of the electron counterpart, in thin films this can be enhanced up to ~10% because the mean free path of electrons ($\lambda_{el} \sim 20-40$ nm) is an order of magnitude larger than the one for phonons at room temperature (λ_{ph}) [16].

At temperatures greater than room temperature we do not expect reliable formation of monoatomic chains when breaking the metallic contact at G_{el}=1 G_0, but rather single atomic constrictions. In this limit we can describe heat transport within the 1D ballistic regime by using the Landauer-type approach for phonons [139, 48], because both the thermal wavelength [140] and the phonon mean free path [16] are larger than the size of a single gold atom:

$$G_{th} = \frac{{k_B}^2}{h} \sum_m \int_{x_m}^{\infty} dx \frac{x^2 e^x}{(e^x-1)^2} T_m(xK_BT/\hbar) \tag{4.3}$$

Here, the summation is over the phonon polarization modes m, T_m are the transmission coefficients of the modes, $x_m = \omega_m(k=0)/k_BT$, assuming a small temperature difference Δ T across the junction, k_B is the Boltzmann constant, h the Planck constant, and T the absolute temperature.

An upper bound for the thermal conductance $\mathrm{G_{th}}$ can be calculated with perfect adiabatic coupling of the thermal reservoirs to the ballistic contact, i.e. $T_m = 1$, although in the case of atomic contacts, a large influence of the microscopic structure of the constriction is expected [141]. To first approximation we can set the upper limit of the integral equal to the Debye frequency of gold $\omega_D = k_B T_D/\hbar$ with $\mathrm{T_D}=$ 165 K and take into account the 3 acoustic modes of the junction considered as a 1D system [142] (neglecting the torsional degree of freedom). With these approximations equation 4.3 reduces to:

$$G_{th} = 3\frac{k_B{}^2}{h}\int_0^{x_D} dx \frac{x^2 e^x}{(e^x-1)^2} \tag{4.4}$$

where $x_D = \hbar\omega_D/k_B T$. At an average temperature T= 320 K we find that $G_{th,ph} = 0.22 G_{th,el}$ at $G_{el} = 1$ $\mathrm{G_0}$. However, depending on the microscopic details of the junction, in particular to the shape of the electrodes, a decrease of $G_{th,ph}$ by about an order of magnitude with respect to the case of an ideal geometry can be expected [141]. Therefore, we can assume a minimum contribution of phonons to heat transport of $G_{th,ph} = 0.02$ $G_{th,el}$.

To extend this range to higher values of electrical conductance, we can consider that the number of both electron and phonon channels involved in transport increases in proportion to the area of the contact, A, at least for sufficiently large contacts. Then the ratio $G_{th,ph}/G_{th,el}$ will be constant with the electrical conductance. Note that this assumption doe not hold strictly: for contacts of few conductance channels different atomic configuration with different cross-sections might show the same electrical conductance value [143]. Nevertheless, the range $G_{th,ph} = (0.02 - 0.22)\, G_{th,el}$ from the above considerations should account for these uncertainties and approximations.

To find a medium value for the phonon contribution to the thermal conductance (red line in Figure 4.4) we can modify equation 4.4 as

$$G_{th} = 3N\frac{A_{el}}{A_{ph}}\frac{k_B{}^2}{h}\int_0^{x_D} dx \frac{x^2 e^x}{(e^x-1)^2} \tag{4.5}$$

where N is the number of electron channels available for conduction, and, A_{el} and A_{ph} denote the area occupied by an electron and phonon channel, respectively. It is possible to estimate $A_{el} = \lambda_F^2/\pi$ and $A_{ph} = \lambda_{th}^2/\pi$ where λ_F is the electron Fermi wavelength and λ_{th} the dominant phonon wavelength when considering thermal conductance [144]. For gold $\lambda_F = 0.52$ nm and $\lambda_{th} = 2\lambda_0 = 0.83$ nm where λ_0 represents the smallest allowed phonon wavelength as indicated by Dames [140].

Interestingly, we can obtain similar results if we apply kinetic theory to treat ballistic heat transport through point contacts [145, 146], i.e. by extending a classical theory to the range of our experiments. To estimate the area A we use the corrected Sharvin's formula for electron transport

$$G_s = G_0(\pi A/\lambda_F^2 - P/2\lambda_F) \tag{4.6}$$

where $A = \pi R^2$, $P = 2\pi R$, with R being the contact radius [147]. By calculating R we can then apply Wexler's formula in the ballistic limit to describe phonon conduction: $G_{th} = 3\pi R^2 k/4\lambda_{ph}$, where k is the bulk phonon thermal conductivity and λ_{ph} the phonon mean free path. From [16] we estimate $\lambda_{ph} = 2$ nm and $k = 2$ W/mK for gold obtaining $G_{th,ph} = 0.14 G_{th,el}$ at $G_{el} = 8G_0$, in good agreement with the range calculated above.

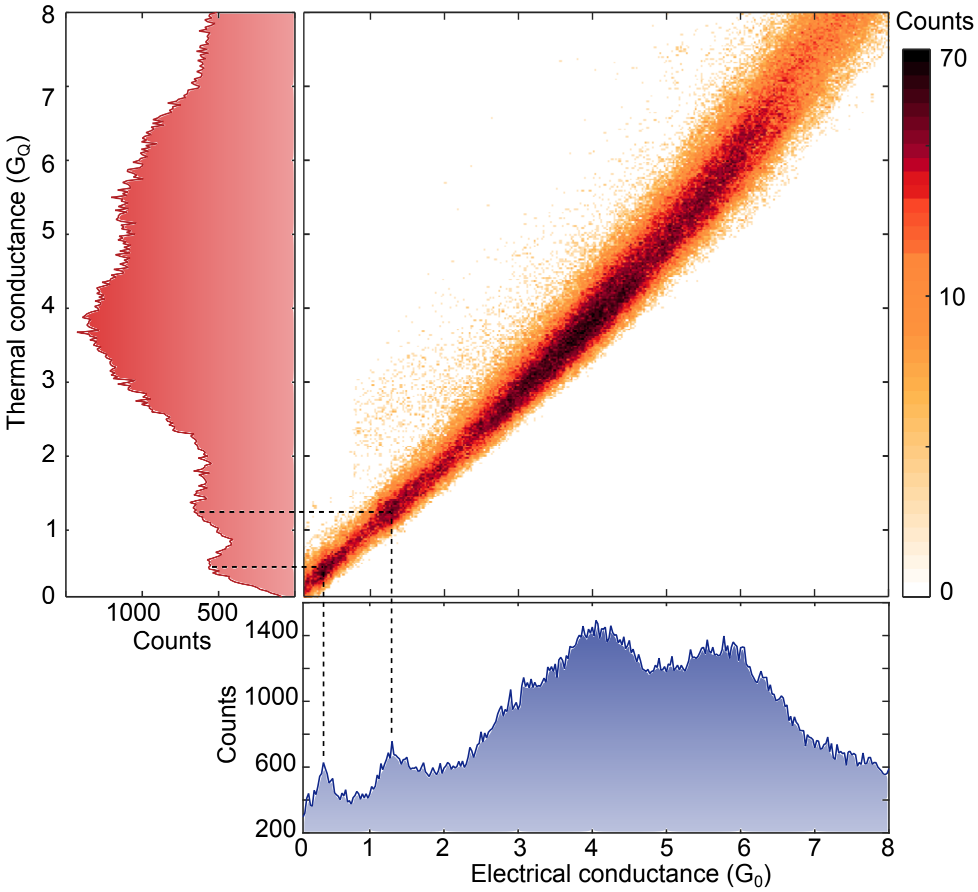

Figure 4.5: 2D histogram of the thermal versus electrical conductance of gold contacts with shifted single atom peak.. The histogram was built with 2000 over 5000 traces selected by setting the temperature range $\Delta T = (35\text{-}50)$ K between tip and MEMS. Thermal and electrical conductance have been normalized with the respective quanta and the 1D histograms built with a linear binning and a bin size of 0.025 $G_Q$and 0.025 G_0, respectively.

4.1.2 Heat transport properties of gold contacts with small organic molecules

Interestingly, tunneling through small molecules may still recover the Wiedemann-Franz signature. Figure 4.5 shows the 2D histogram of thermal and electrical conductance measured on a different MEMS sample that was cleaned by thermal annealing in high vacuum. In this measurement, we note that the mean position of the single atom peak (usually at 1 G_0) is shifted to higher values both in the electrical (~1.3 G_0) and thermal (~1.3 G_Q) conductance histograms. According to literature, the absorption of CO molecules on gold electrodes introduces an additional peak at 0.2-0.3 G_0 [148, 149] or at 0.7 G_0 [149, 150] depending on the experimental conditions. In particular den Boer et al. [148] reported a shift of the G_0 peak to larger conductance values in their study of Au-CO-Au junctions at room temperature in liquids. This shift can be attributed to the trapping of a single CO molecule in parallel with a single atom junction for some of the opening traces. In our case, we

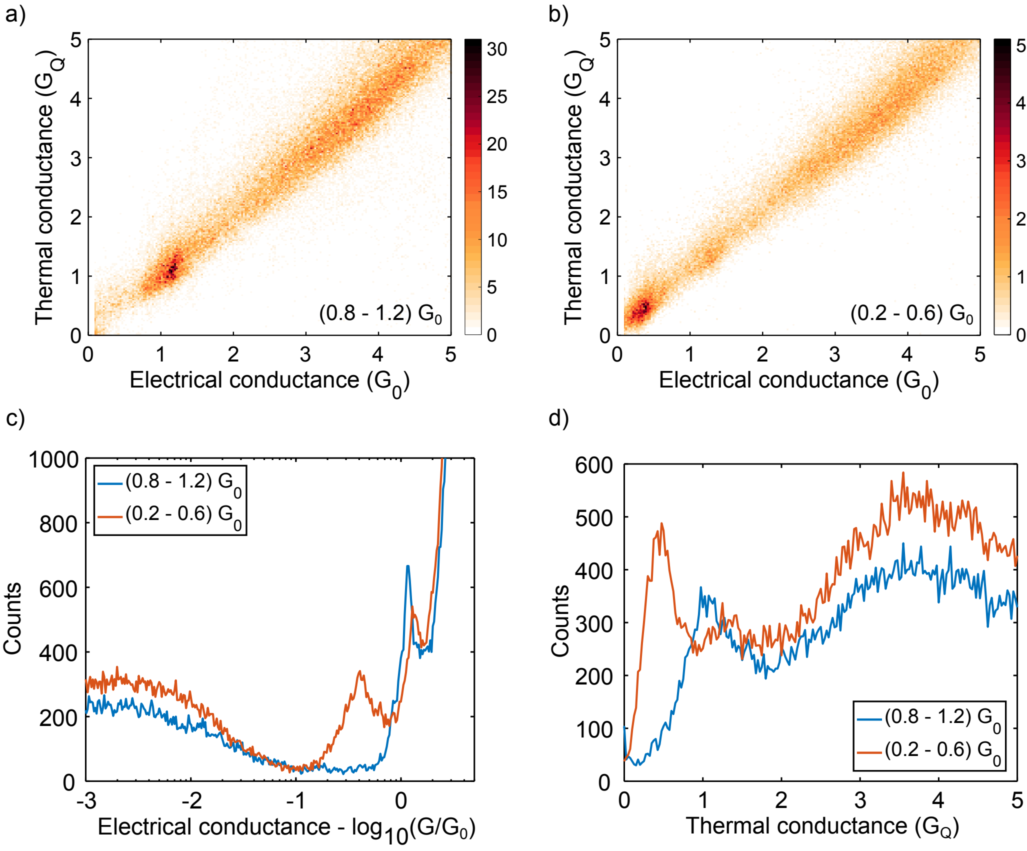

Figure 4.6: Position of the single atom peak influenced by the molecular junction. a) 2D histogram built with 576 traces showing plateaus between 0.8 and 1.2 G_0. b) 2D histogram built with 728 traces showing plateaus between 0.2 and 0.6 G_0. c) 1D electrical histogram for the 2 subsets of traces. d) 1D thermal histograms. Only the portion of trace with $G_{el} > 0.1$ G_0 was used to build the histograms, to avoid the artifact in the first bin.

can expect CO molecules to be present on the Au surface even after wet chemical and heat cleaning, probably because of the several processing steps needed for fabricating the MEMS [151, 112]. We can therefore interpret the increased conductance value as an electrical path through the CO molecules in parallel to the gold atomic contact. This is confirmed by the presence of a sharp peak at around 0.4 G_0, which can be assigned to the conduction through the molecule alone. We note, however, that also other small molecular species such as H_2O, or hydrogen have been related to similar sub-G_0 conductance features in the literature. Therefore, further studies are needed to systematically investigate these molecular junctions.

As an important evidence, we find that the measurement is composed by mainly 2 subsets of traces. By selecting traces that exhibit plateaus in the region 0.8 to 1.2 G_0 (assigned to a single atom contact in the absence of a molecule), the molecular peak at 0.4 G_0 is drastically reduced and the 1.3 G_0 peak moves towards its original value in both the electrical and thermal 1D histograms, Figure 4.6c and d. On the other hand, traces showing plateaus between 0.2 and 0.6 G_0 exhibit at the same time a peak at 1.3 G_0. This confirms the interpretation that the molecular specie with electrical conductance of 0.4 G_0 participates to charge and heat conduction before

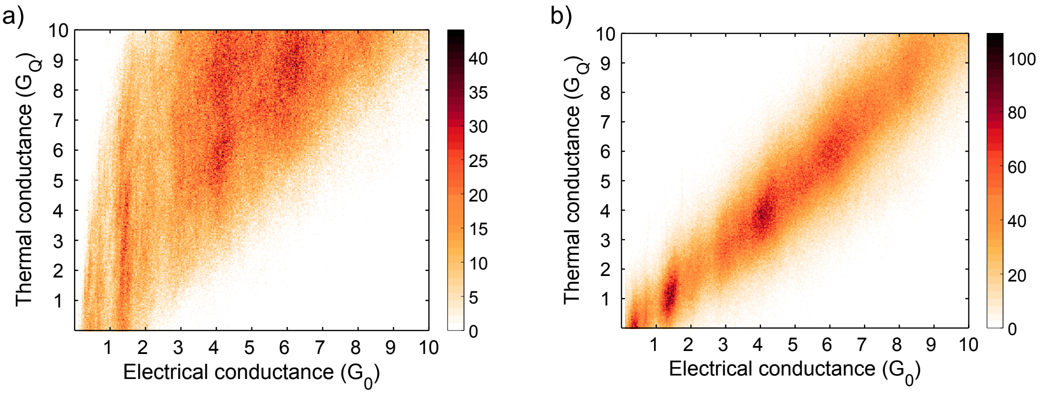

Figure 4.7: High power dissipation in atomic junctions. a) 2D histogram built with 2500 traces (without selection) measured at a voltage V = -300 mV without taking into account the power dissipated in the junction. b) Same dataset considering that half of the power dissipated in the junction contributes to the MEMS heating.

breaking the single atom contact. Moreover, all of the junction configurations (single molecule, single Au atom, single molecule and Au atom) satisfy the Wiedemann-Franz law as shown in 2D histograms Figure 4.6a and b. For molecular junctions this means that the electron contribution to the thermal conductance dominates and charge transport occurs via non-resonant coherent tunneling [152]. Similar results are predicted for highly conducting molecules like C_{60} [44] and indeed phonon thermal conductance of molecular junctions between gold electrodes is usually on the order of few tens of pW/K, thus negligible in this case[14, 43, 153]. Violations of the Wiedemann-Franz law are expected for junctions in which the Fermi energy of the electrodes lies close to one of the resonances in the transmission function. Far from resonance, if the Fermi liquid model holds, the Sommerfeld expansion of the thermal conductance integral leads to the Wiedemann-Franz law [45], as in the case of gold atomic junctions.

4.1.3 Power dissipation in atomic contacts

To verify that the analysis taking into account Joule dissipation is accurate and that the correlation between thermal and electrical transport signals is not affected by other effects than considered, we repeated the measurements using different voltage bias values and sign, reaching values of up to V = -300 mV. Under such high bias conditions, the contribution of the electronic dissipation at the junction is significant and must be taken into account, Figure 4.7. Furthermore, the temperature of the MEMS platform is strongly affected by the Joule dissipation in the junction and suspended STM line, which can even lead to a net increase of temperature in the platform instead of a net cooling through the atomic contact. The results confirm our interpretation, and the underlying assumption that heat dissipation in atomic scale gold contacts occurs symmetrically in the electrodes, as shown recently [58].

4.1.4 Thermal background

Similar to other scanning probe techniques, artifacts in the data may arise from undesired interactions between the tip and the sample. STM-BJ is not

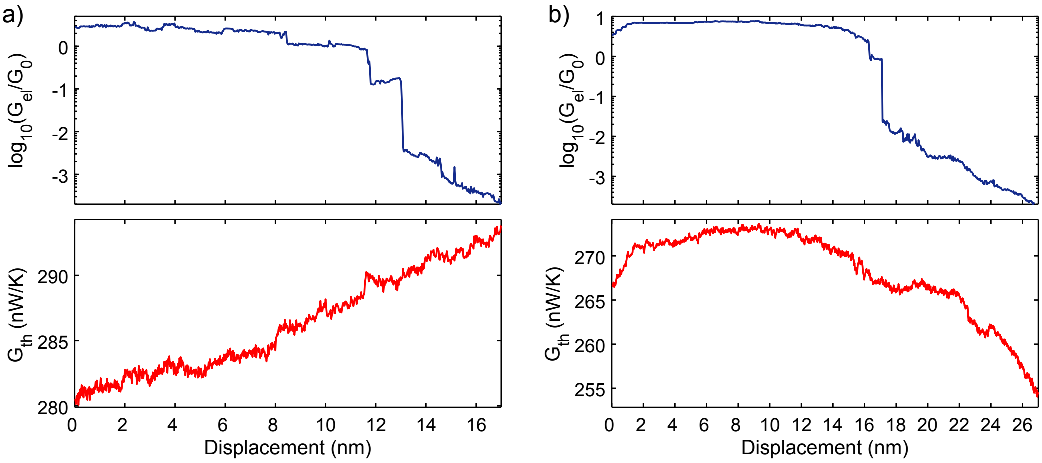

Figure 4.8: Opening traces showing a thermal conductance dominated by the thermal background.

different in this respect and selection rules are sometimes needed to analyze the measured data. However, data selection in statistical evaluation of break junction experiments requires clear criteria to avoid arbitrary influencing the outcome. In these experiments, reconfiguration of tip and MEMS surface can lead to situations in which parasitic coupling through molecular contaminants and near field radiation dominate heat transport, decreasing the sensitivity of the measurement. These situations are very clear in the data and have to be excluded from the analysis to avoid misinterpretations. Such "thermal background" has three main effects, of which either can be used as a criterion for data selection. First, the parasitic contact can be so large that the temperature of the MEMS sensor drops to below 10 °Cabove ambient as shown in Figure 4.8a. Note that the thermal conductance signal includes all the contributions: MEMS, parasitic contact and atomic junction. In the out contact (for displacements greater than 13 nm) G_{th} reaches a value of 290 nW/K, which is almost 9 times larger than the thermal conductance (34 nW/K) of the isolated MEMS as measured with the IV characteristic. This means that a large thermal contact with the tip has been formed and it is reflected in the trend versus displacement, completely uncorrelated with the electrical conductance signal G_{el}. Interestingly, G_{el} does not seem to be influenced by the formation of such parasitic contact and indeed in some cases the electrical histograms built with these type of traces do not show any artifact.

Secondly, the thermal background can present a significant slope in the thermal signal in the non-contact (tunneling) region, Figure 4.8b. Typically, background slopes up to 2-3 $nWK^{-1}nm^{-1}$ do not induce artifacts in the 2D histograms provided that the slope stays stable during the measurement (or at least few hundred traces). Thirdly, the trace length between the predefined turn-around points (e.g. $G_{el} = 5$ G_0 and 10^{-5} G_0) can be unnaturally large, up to few tens of nm. Typically, all these three effects occur simultaneously.

The criterion based on the ΔT range has been applied to the dataset in Figure 4.5. In Figure 4.9 we present, for comparison, the 2D-histograms before (a) and after (b) data selection, showing that the data omitted did not appear to have any correlated nature. This does not mean that for the histograms showed there is no

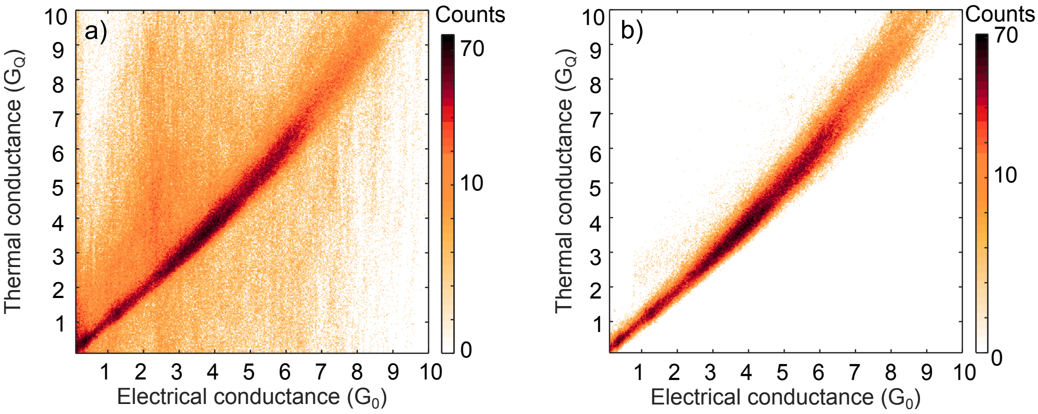

Figure 4.9: Effect of the thermal background on the conductance measurement of Au-Au contacts. a) 2D histogram obtained from 5000 traces (no selection) including the ones with unstable thermal background. b) 2D Histogram obtained selecting the 2000 traces within the temperature range ΔT = (35-50) K.

thermal background. The formation of a thermal contact (typically few tens of nW/K) between the MEMS and the tip is intrinsic to the experimental technique and cannot be easily avoided. Moreover, it provides mechanical steadiness to the junction, which is fundamental to perform STM-BJ on such compliant structures. The key aspect is the stability of the thermal background during the measurement. More details are provided in chapter 5.

4.1.5 Uncertainty calculation

Possible sources of errors can be divided into systematic errors affecting all the data in the same manner, and random scatter represented by the spread of points in the 2D histograms around the median. The overall systematic error has been included as shaded region around the distribution median in Figure 4.4. The main sources of error in the measurements are the uncertainty in the resistance value of the heater R_{4Pamb} at room temperature extracted from the I-V calibration and the accuracy in the electrical resistance measurement. Errors related on the underetched ratios (see 3.1.6), temperature variation of the beam resistance connecting the gold pad have also been considered even if having a smaller influence. Let f denote the measured quantity, in our case the median f of the 2D histogram. The absolute uncertainty δf can be defined as function of the errors δf_i induced by the single parameters i according to:

$$\delta f = \sqrt{\sum_{i=1}^{n} \delta {f_i}^2} \tag{4.7}$$

where $\delta f_i = f_i(G_{EL}) - \bar{f}(G_{EL})$ represents the distance between the median f_i and the reference $\bar{f}$ at every electrical conductance point G_{el}. Following this approach, we could propagate the uncertainty on the single parameters to the corresponding median of the histogram. We therefore considered the extremes of the uncertainty range of the parameters listed above and we built the respective 2D histograms. From the medians f_i of the obtained distributions we calculated the errors δf_i relative to the median $\bar{f}$ of the reference histogram. Finally, we used equation

4.7 to assess the total absolute error, δf. Specifically, we considered: $R_{4Pamb} = (16120 \pm 30)\ \Omega$, 5% error on the estimation of the underetched ratios for the heater and stm lines, 1% on the beam resistance in the STM circuit, and 2% on the measurement of the junction resistance (after calibration of the correction factors, amplifier gains and offsets). The resulting medians define a positive and negative error (lying above or below the reference) for every G_{el} value that can be separately inserted into equation 4.7 to obtain the lower and upper limits of the uncertainty range.

It is noteworthy, that for the dataset presented in Figure 4.4 we didn't have to consider as a correction factor the Seebeck voltage generated at the connection between the gold platform and the metal line, because made out of gold. For the sample used in Figure 4.5, instead, Pt lines were used to contact the gold platform forming effectively a thermocouple which adds a series voltage V_{Seeb} to the junction that depends on the temperature T of the membrane. If a positive voltage bias is applied to the tip then $V_{Seeb}(T) = \Delta S(T - T_{amb})$ with $\Delta S = (S_{Pt} - S_{Au})$. The experimental characterization of this effect is a challenging task because it involves the disentanglement of the Seebeck effect from the temperature dependent series resistance $R_b(T)$. For bulk Au-Pt wire thermocouples ΔS values of 7 µV/K are reported [154]. The film quality can affect the value of the Seebeck coefficient but it is hard to find a direct comparison in literature. Au-Pt [137] and Au-Cr [58] micro-thermocouples integrated in AFM tips are reported to have ΔS values that are very similar to the bulk counterparts. Using $\Delta S = 7.5$ µV/K with an estimated accuracy of 10% gives an offset $V_{Seeb} = 280$ µV at $\Delta T = 40$ K. This may appear negligible with respect to the voltage applied (~ 50 mV), but we should take into account that most of it drops over the external series resistance ($R_s = 100$ kΩ in this case) when the junction is closed ($R_j < 12.9$ kΩ). Therefore, the correction becomes important especially for electrical contacts with conductance above 5 G_0.

The compensation for the Seebeck voltage still carries significant uncertainty, which is reflected in the curvature of the 2D histogram observed in Figure 4.5. Notably, this bending of the 2D histogram for Au-Au contacts was no longer observed for samples with gold lines connecting to the MEMS platform, confirming the influence of the Seebeck voltage in the electrical conductance measurement.

4.1.6 Angled approach

As described in section 3.2.3, the approach/retraction motion of the tip is usually performed at an angle between 25 to 40 deg with respect to the in-plane direction of the membrane. When the tip is moved without such an angle, i.e. simply perpendicular to the surface, in most of the cases the pulling motion leads to strong spring loading of the MEMS. As a result, the electrical conductance typically jumps directly from the values of fully closed junctions (e.g. 10 G_0 or more) to the tunneling regime (below 10^{-3} G_0), effectively omitting the atomic-scale contact sizes. If, in contrast, the angled approach is used, then the spring loading of the MEMS sample can be significantly reduced. A remaining small amount of spring loading occurred potentially ensuring that the opened junction does not immediately close again due to long-range attractive forces through a jump-to-contact procedure. More importantly, however, the pulling procedure resulted in a higher yield in producing junctions with conductance values associated with atomic scale contacts between 1

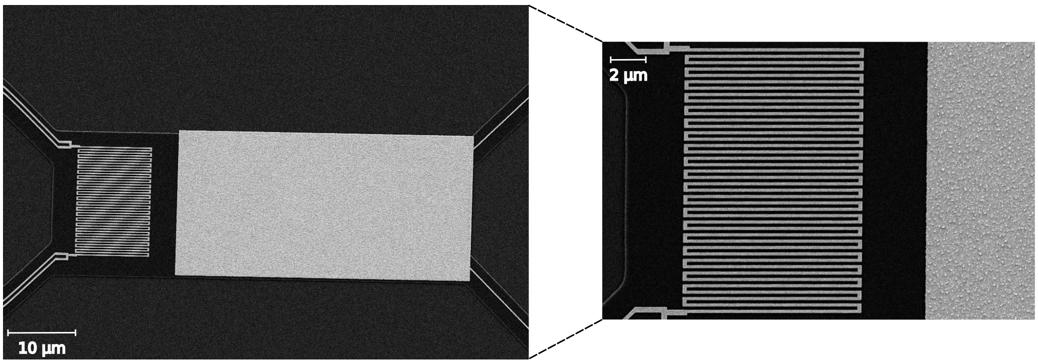

Figure 4.10: SEM image of a MEMS sample with a rough gold surface. Gold nanoclusters with an average size of 50×50 × 50 nm are randomly distributed on the surface.

and 10 G_0.

The observation that a rupture, or decohesion process is eased by a lateral motion is well known from tribology studies. However, the downside of this approach is a greater sensitivity of the measurement to variations in the thermal background. A significant influence of the roughness of the sputtered gold surface on the observed decohesion process is also expected, translating on the atomic scale into significantly different local angles with respect to an idealized flat surface and influencing the stretching of bonds during the opening traces. The estimations of the in-plane ($\sim$ 100 N/m) and out-of-plane ($\sim$ 1 N/m) spring constants of the MEMS device support this reasoning. To quantify the effect, however, would not only require quantitative determination of the effective spring constants along xyz, but it would also require knowledge on the roughness and geometry of both tip and surface that goes beyond the scope of this work.

4.1.7 Gold surface roughness

The role of surface roughness in the STM-BJ experiments performed on the MEMS is still under experimental investigation. Usually, the gold film on the fabricated samples features an rms roughness of 2.5 nm measured over an area of $1 \times 1 \mu m^2$ using atomic force microscopy (tips from nanosensors PPP-NCHR-W, guaranteed radius of curvature below 10 nm taken fresh from the wafer). Figure 4.10 shows an example of a fabrication run in which the gold film underwent substantial heating after the oxygen plasma treatment before releasing. Even though the causes are still somewhat unclear, the samples represented an ideal test case to probe the effects of surface roughness. Having an atomically flat metallic surface is fundamental for performing STM imaging or to create high quality self assembled monolayers, but it is not reported to influence break junction measurements, as the process requires only the formation of electrical contacts between tip and MEMS. In fact, several molecules were deposited on these surfaces and their electrical conductance successfully measured. On the other hand, the roughness showed a quite striking effect concerning thermal conductance measurements. In fact, atomic and molecular junctions could be formed on these samples with high yield and reliability. The histogram showed in figure 4.3 is an example. The reason of this beneficial effect of roughness may be explained by taking into account that the tip is moved at an angle with respect to the MEMS surface to take advantage of its larger in-plane stiffness; thus, the uneven topography of the gold film might help the breaking of the junction. Moreover, the size of the thermal contact formed between tip and MEMS can be reduced by the presence of irregularities on the surface, decreasing the parasitic heat conduction through adsorbates. Even if the gold surface roughness seem to have a influence on the experiment, it is not a requirement, as good datasets were regularly measured on standard samples, as shown in Figure 4.5. These effects on the junction mechanics and cleanliness need further investigations, and attempts to fabricate samples with specific topographic features on the MEMS are currently under test.

4.1.8 Tip temperature

During the break junction experiment, we assume that the gold tip is at room temperature near the apex, that is at a distance from the atomic junction consistent with the ballistic nature of transport, i.e. comparable to the mean free path of electrons, which can was estimated to 5 nm [146, 155, 156] in similar junctions (significantly lower than the 20 nm estimated in bulk [16]). If the thermal resistance along the Au wire is not negligible, i. e. between the junction and the base of our microscope, there could possibly be a temperature difference between the two positions. For an order of magnitude estimation of the effect we can calculate the thermal resistance of a wire shaped as a truncated cone with base and tip radius of R_1 =0.125 mm and R_2 =25 nm, respectively and a length $L = 0.5$ mm as estimated from electron microscopy images of our tips. From Fourier's law of (diffusive) thermal transport one can demonstrate that the thermal resistance R of the tip is

$$R_{th} = \frac{L}{\pi R_1 R_2 k} \tag{4.8}$$

where ρ is the thermal conductivity of gold. Assuming $k = 315$ WK$^-$1m$^-$1 we obtain resistance of about 2×10^5 K/W. As this is orders of magnitude smaller than the thermal resistance of the atomic contacts ($\mathrm{R_{th}} = 1.76 \times 10^8$ K/W for a 10 $\mathrm{G_0}$ contact at 300 K), we may safely neglect the effect of a series thermal resistance in the tip within the accuracy of our experiment.

The temperature of the base plate of the microscope is the reference for both tip and MEMS. This affects the value of the average temperature of the junction used to verify the Wiedemann-Franz but not the electrical conductance which is temperature independent. The temperature of the lab is controlled to 295 K within 0.01 K [55] and the microscopes base plate is thermally well coupled to the environment. The uncertainty in the base temperature can therefore be neglected for the purpose of this experiment. The position of the $\mathrm{G_0}$-peak in the electrical conductance histogram should not depend on the T of the tip. This is not true for the thermal conductance quantum which by definition depends linearly on the junction temperature. However, the results obtained at high electrical voltage 4.1.3 confirm that a large temperature change at the tip can be excluded.

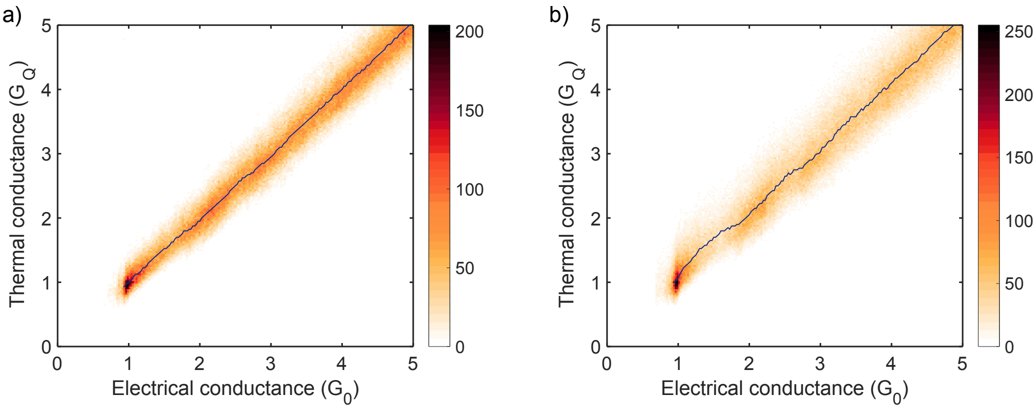

Figure 4.11: 2D histogram of thermal versus electrical conductance. a) Electrical conductance traces digitally low-pass filtered to build the histogram. The black continuous line corresponds to the median of the histogram. b) Unfiltered electrical conductance traces.

4.1.9 Data analysis procedure

The electrical and thermal conductance traces showed in this chapter are calculated according to the mathematical model presented in 3.1.6. All the data analysis is performed in Matlab with own written codes. To build the 2D histograms, the out-of-contact value is subtracted to the thermal conductance signal trace by trace, to compensate for variations in the thermal background. For this purpose, the electrical conductance G_{el} is used as reference and the out-of-contact defined when $G_{el} < 5 \times 10^{-2}$ with an additional delay of few ms, to take into account the slow step response of the thermal conductance. Since the temperature of the MEMS changes continuously during the measurement and within each single trace, the quantum of thermal conductance is calculated according to the average junction temperature obtained for every datapoint. Typically, to build the 2D histograms in the contact regime, the points in the electrical and thermal traces below $G_{el} = 0.1\ G_0$ are excluded to avoid the high number of counts in the first bins.

Figure 4.11 shows the effect of using a low-pass filtered electrical signal with the thermal time constant. As this is usually higher (20 to 40 ms) than the sampling time set to capture the dynamics of the breaking process (typically 1 to 10 ms), at the sharp transition between 2 electrical plateaus the thermal conductance responds with its intrinsic delay. This can be clearly observed in the 2D histograms as deviations from the Wiedemann-Franz law with apparent higher Lorenz numbers, e.g. in the transition between 1 and 2 G_0, Figure 4.11b. For this reason, the digitally filtered electrical traces are usually employed to build the 2D histograms.

4.2 Pt-Pt contacts

Platinum is also one of the most investigated metals to contact single organic molecules and to study charge transport in atomic junctions [15]. Differently from gold, breaking platinum point contacts does not show conductance quantization and the 1D histograms measured at low temperature (4 K) are usually characterized by one peak between 1.5 and 2 G_0, which is attributed to the formation of a single atom

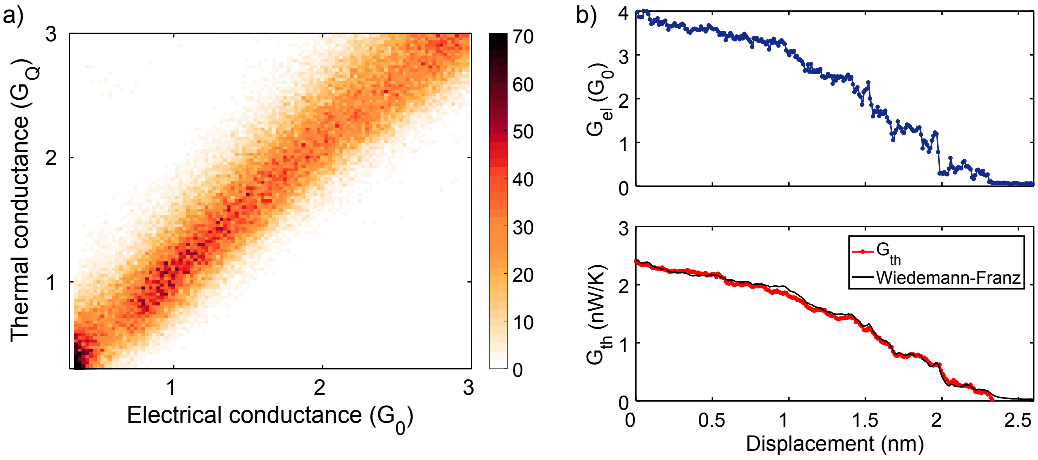

Figure 4.12: Heat transport measurements across Pt atomic contacts. a) 2D histogram built with 1024 traces measured at V = 50 mV and average $\Delta T \sim 48$ K. b) Example of single opening trace showing correlated electrical and thermal conductance.

constriction [157, 158, 159]. The fact that single atoms have a conductance higher than a quantum G_0 stems from the electrical conduction through the anisotropic d orbitals, which can allow up to 5 conduction channels with transmissions lower than 1 and strongly dependent on the coupling to the neighbouring atoms in the leads [15, 30]. It was shown that platinum can also form monoatomic chains during break junction experiments, a feature of 5d metals that present surface reconstruction (Au Pt and Ir) [160, 158]. Moreover, contrary to gold, Pt atomic contacts are stable at room temperature and therefore interesting for molecular electronics applications[161].

To investigate heat transport properties of Pt atomic contacts, we fabricated MEMS with platinum platforms, keeping the same design with angled beams, and electrochemically etched Pt-tips as explained in the appendix B. Figure 4.12a shows the 2D histogram of the thermal versus electrical conductance built with 1024 traces showing at least 25 ms long traces in the conductance region between 0.8 and 2 G_0 (to exclude fast breaking traces). Both thermal and electrical conductance have been normalized with the respective quanta. As in the case for gold, we find a very good agreement with the Wiedemann-Franz law, demonstrating that most of the heat is transported by electrons. As expected for room temperature experiments, the electrical and thermal 1D histograms do not show particular features [124], and single opening traces exhibit a rather continuous breaking behavior without clear steps, Figure 4.12b. It was indeed reported that the electrical conductance of Pt contacts is sensitive to the presence of adsorbates on the surface, reflected in the non-reproducible structure in the histograms measured at room temperature. For instance, the introduction of hydrogen molecules at 4 K shifts the characteristic peak from 1.5 to 0.9 G_0 [157], similarly to nominally clean experiments at room temperature [162]. As reported in literature, also in our experiments we find it more challenging to obtain reproducible electrical and thermal histograms in comparison with gold contacts. These results for Pt-atomic contacts were also confirmed in recent experiments [69] and theoretical studies [163]. Interestingly, similar experimental challenges are reflected in the lower statistics (100 traces compared to 2000 for gold contact) reported in Ref. [69].

In the future, it will be interesting to explore the heat transport properties of different metals at low and high temperature, to gain further insights into the phonon dynamics, which so far has remained experimentally inaccessible. For measurements with molecular junctions, it is especially appealing to extend the measurement technique to metals with higher Debye temperatures like Ni (T_D = 345 K) or aluminum (T_D = 390 K) [164], to minimize phonon filtering of the electrodes and investigate the contribution to the thermal conductance of the vibration modes of the molecules at different energies.

4.3 Metallic hetero-junctions

In the early indentation experiments of a stiff STM tip (e.g. W, Pt-Ir, Ni...) into a soft substrate like gold, it was found that a thin gold layer can adhere to the surface of the tip [15, 165]. Such coated tips were used to study electrical conductance quantization of gold [166] and other metals (Pt, Cu and Ni) [22]. Atomically thin metallic tip coatings fabricated via electrochemical methods were also used to perform BJ experiments [167]. Using tips fabricated with metals like Pt-Ir and W is quite attractive because of the high-durability and mechanical stability demonstrated by these materials and indeed it is very common for STM imaging in different environment conditions from UHV to ambient (only for Pt-Ir as W oxidizes).

To investigate the effects of different tip materials in the heat transport measurements, we fabricated Pt, Pt-Ir (10% Ir) and W tips by electrochemical etching achieving tip radius on the order of 50 nm, for Pt and Pt-Ir, and 25 nm, for W. Prior to start the measurement on the MEMS, the freshly fabricated tips were indented on a gold pad on the substrate to avoid the influence of the MEMS mechanics during tip formation. Few hundred break-junction traces were then collected to test the gold coating of the tips. Indeed, after few indentation cycles electrical histograms showed quantized conductance peaks at multiples of G_0, as typically observed with Au tips. Figure 4.13 shows the results obtained with Pt and Pt-Ir tips on the MEMS. As expected, W tips demonstrated to be harder to clean especially because of oxidation and gave inconclusive results. Single opening traces (b-d) exhibit quantization steps and plateaus at 1 G_0, indicating the formation of single gold atom contacts. The thermal conductance follows a similar trend in good agreement with the Wiedemann-Franz law. To confirm this finding, we built 2D histograms (a-c) with respectively 878 and 795 traces (out of 2000) showing 1G_0 plateaus of at least 10 ms long. This selection was done to underline the single atom peak in the thermal histogram, which otherwise would be hidden by the fast breaking traces. Note that this does not affect the slope of the 2D histogram. The histograms were built with the unfiltered electrical traces to avoid the smearing of the 1 G_0 peak. Interestingly, we obtain very good agreement with the Wiedemann-Franz law also with these coated tips, within the uncertainty of the experiment. This means that the interface thermal resistance between the tip metal and the gold layer is negligible and it does not influence the average temperature of the junction. The samples used for these experiments feature a gold line connecting to the platform on the MEMS. We could therefore expect seebeck voltages generated by the metallic hetero-junction when the MEMS is heated, but

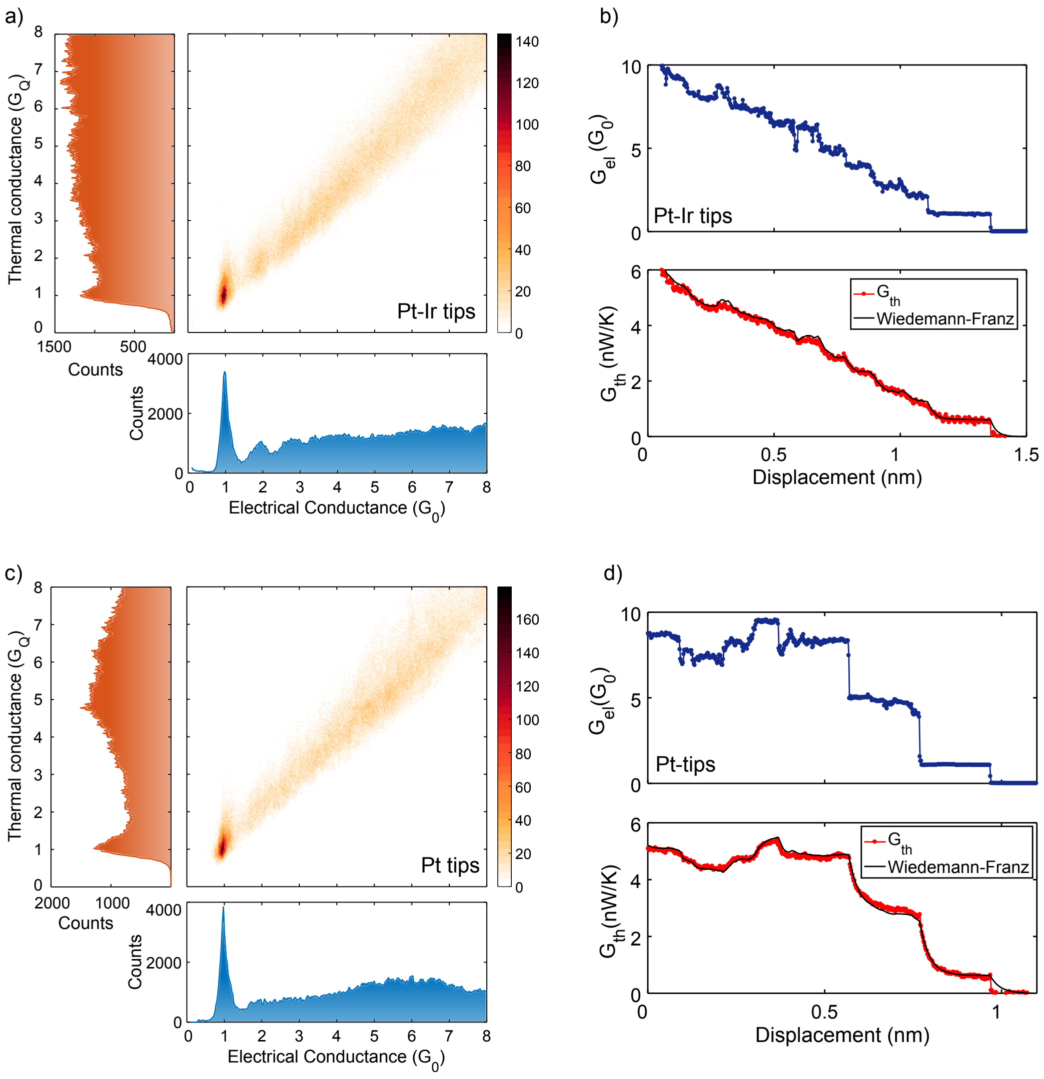

Figure 4.13: Heat transport measurements of Au-Au contacts with Pt-Ir and Pt tips. a-b) 2D histogram and example of opening trace with Pt-Ir tip measured at V = 40 mV. c-d) 2D histogram and example opening trace with Pt tip measured at V = 40 mV.

the effects are negligible considering the small series resistance (R_s = 16 kΩ taking into account the external and beam resistance) and ΔT = 30 K.

Moreover, the plateaus at 1 conductance quantum appear to be longer than the ones usually measured with gold tips. This effect seems to be enhanced when performing the experiments on the MEMS. While on the substrate, different tip materials yield on average 2-3 data points at 1 G_0 per trace, on the MEMS with Pt and Pt-Ir tips we can reliably obtain 3 to 5 points compared to 1-2 with Au tips. This corresponds to an average greater plateau length, while the maximum one stays unvaried. Only with in rare occasions, we can obtain quantized peaks with intensities as showed in Figure 4.3. This phenomenon is of course extremely beneficial for heat transport measurements, as longer plateaus allow the thermal signal to reach equilibrium, compensating for the thermal time constant.

These results were confirmed on MEMS designs with different angles of the beams, and do not depend on the approaching angle of the tip (20° to 40°). This can be understood, by considering that the breakdown mechanism of the junction is thermally activated, and independent on the force applied with the typical experimental conditions. It is known that the atomic/molecular junction lifetime and breaking force depends on the force loading rate [168, 169, 170]. In particular, stretching the contact lowers the energy barrier required to break the bond and below a stretching rate of about 2600 nN/s for gold at room temperature [168], the breaking is mainly thermally activated. With typical closing/opening speeds of 1 to 4 nm/s and an estimated stiffness of the MEMS of maximum 100 N/m along the direction parallel to its axis, we can safely assume to be in the spontaneous breaking regime.

The effect of the stiffer tip material on the mechanical stability of the junction depends on many different parameters, like the tip shape, material properties or the microscopic details of the junctions formed. We can expect that the hardness of the metal does not play a significant role, as Pt and Pt-Ir yield similar results. However, the Young's modulus (79 GPa for Au, 168 GPa for Pt, 185 for hardened Pt-Ir) [171] combined with the apex shape may result in an increased tip mechanical stability. Performing a thorough analysis of this effect requires large statistics and proper knowledge of the microscopic details of the junction, which goes beyond the scope of this work. However, the finding that stiffer metallic tips improve the stability of single atomic contacts on the MEMS without affecting the heat transport measurements is very interesting and it might be beneficial also for molecular junctions.

Chapter 5

Single Molecule Junctions

In this chapter, heat transport measurements across single molecular junctions are presented. In particular, by using the technique described in chapter 3, we probed the electrical and thermal conductance of two model systems, namely dithiol-oligo(phenylene ethynylene) (OPE3) and octane dithiol (ODT) with gold electrodes. In agreement with density functional theory and transport calculations, we show that octane junctions have the higher phonon thermal conductance.

The work presented here represents the first measurement of thermal transport through single molecules. The experimental method developed is versatile and can be applied to different molecular systems without foreseen difficulties. These results have been recently submitted for publication. The theoretical calculations presented in section 5.5 have been performed by our collaborators Dr. Hatef Sadeghi, Dr. Sara Sangtarash and Prof. Colin Lambert from the University of Lancaster.

5.1 Introduction

Heat transport through molecular systems takes place through a wealth of transport mechanisms. When the heat is carried by vibrations, these include ballistic and hopping transport, phonon interference [172, 173, 12], rectification [13] and localization [5], and extend beyond equilibrium-based thermodynamic transport [6]. The characterization of molecular junctions and tuning of such properties would underpin numerous technologies and isolate fundamental effects yet to be demonstrated.

Both experimental and theoretical analyses of molecular heat transport face severe challenges. To simulate heat transport in molecular junctions, different length scales of heat carrying phonons have to be taken into account, ranging from Ångstroms to microns at ambient temperature. Molecular dynamics simulations have been utilised in the classical or high temperature limit to identify the role of binding groups and interference effects [172]. More recently, significant progress was made describing junctions as Landauer systems with an energy-dependent phonon transmission calculated using Green's functions and density functional theory [173, 5, 14], or approaches beyond the harmonic approximation [6]. Numerous predictions of interference phenomena [173, 7] and non-linear effects [13] await experimental verification.

The thermal conductance of a single molecular junction is typically an order of magnitude lower than the thermal conductance quantum (284 pW/K at room temperature)[1] and therefore difficult to measure. For example, alkanes chemically bound to two metal thermal reservoirs, have measured and predicted thermal conductance values on the order tens of picowatts per Kelvin [6, 174]. As these systems form self-assembled monolayers (SAMs) of high quality, they can be measured using spatially averaging methods like time/frequency-domain thermoreflectance [8, 9] or scanning thermal microscopy [4]. However, for most molecular systems, ordered films cannot readily be made and even if that is case uncertainties in the actual percentage of molecules bridging the reservoirs still remain [9, 4]. Single molecule measurements are prone to difficulties, due to the experimentally inaccessibility of the atomic-scale environment of an individual molecular junction, but they would enable systematic studies of the relationship between chemical structure and energy transport properties.

As model molecular systems, we have chosen oligo(phenylene ethynylene)dithiol (OPE3) and octaneditiol (ODT) contacted by gold electrodes. OPE3 is probably the best studied molecule for electrical transport, with widespread agreement reached by different groups for its electrical conductance [175, 36, 106, 176]. However, heat transport through OPE3 with thiolate end groups has neither been studied experimentally nor theoretically. On the other hand, ODT is a member of the alkane family, whose thermal transport properties have been intensively studied both theoretically and experimentally. Nevertheless, the many possible junction configurations recognized in the charge transport experiments [177, 178, 56, 176], make it a challenging system to test the limits of our new method.

5.2 Experimental results

In order to combine heat and charge transport measurements at the single molecule level, we use MEMS structures with angled beams, like the ones described in chapter 3 and utlised to study gold atomic contacts. The main difference with the experiments of chapter 4 lies in the sample preparation. The MEMS are cleaned by a combination of oxygen plasma and ion milling to remove contaminants post-fabrication and retrieve a fresh gold surface. OPE3 or ODT are deposited on the gold platform by immersing the entire MEMS in freshly prepared solutions of dichloromethane or ethanol, respectively, with concentrations ranging from 0.1 to 1 mM for 30s to 2 hours. After the deposition, the samples are rinsed several times in clean solvent to eliminate physically adsorbed molecules. The details about the sample preparation are provided in section 5.3.

After deposition of the molecules, the MEMS is loaded into the vacuum chamber, until a pressure of about 10^{-7} mbar is reached. During the STM-break junction experiments the electrochemically etched gold tip and the sample substrate are kept at room temperature (22 °C) by the mechanical links to the setup. Figure 5.1a shows a schematic of the measurement technique. Prior to contact formation, the membrane is heated to a temperature $T_H \sim 350$ K by applying a constant voltage to the Pt-heater, corresponding to few µW of dissipated power. The temperature T_H is continuously monitored by measuring the 4-probe resistance of the heater with

---

[1] Note that the thermal conductance of a single gold atom is equal to 568 at room temperature, corresponding to 2 conductance quanta, because of the spin degeneracy of a single electron channel.

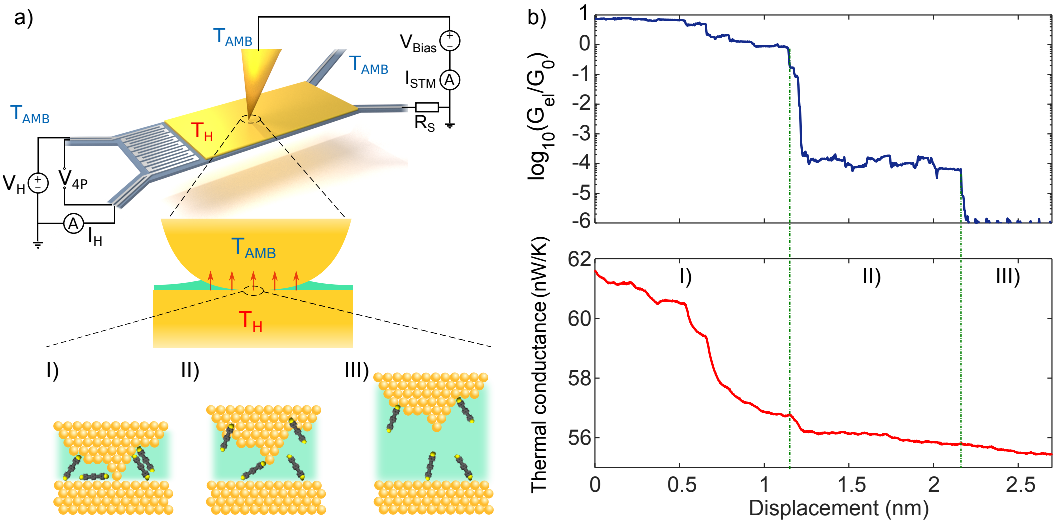

Figure 5.1: Schematic of the measurement technique. a) Schematic diagram of the experiment with the different transport regimes I – II – III upon breaking the tip-MEMS contact. The green meniscus represents the thermal contact with adsorbates on the MEMS. b) Example of typical opening trace showing the variation of the electrical conductance of the junction G_{el} normalized by the conductance quantum $G_0 = 2e^2/h$ and the overall thermal conductance of the Tip-MEMS system versus tip displacement. I) Au-Au contact. II) Formation and elongation of a single molecule junction indicated by the electrical conductance plateau. The variation in thermal conductance is most likely due to a modulation of the contact area with the adsorbates. III) Breaking of the molecular junction, resulting in a small decrease of the overall thermal conductance, on the scale of few tens of pW/K.

the same circuitry and gain settings used in the atomic contact experiments, equal to 1000 for both the heater current and 4-probe voltage (see Figure 3.6 for the full electrical circuit). The total thermal conductance k_{th}[2] of the MEMS is calculated by dividing the total power provided to the heater and the $\Delta T = T_H\text{-}T_{AMB}$ with respect to the substrate.

Figure 5.1b shows an example of a single opening trace measured by retracting the tip at 25° with respect to the MEMS surface at a speed of 5 nm/s along the motion direction. As typically done in break junction measurements, gold contacts with conductance of about 10 G_0 are formed during approach so that the single atom peak at 1 G_0 can be used as reference. Moreover, this leads to rearrangements of the microscopic details of the contact that above room temperature reduce the statistical correlations between consecutive traces [179]. In other words, closing the contact to 10 G_0 helps the formation of new molecular junctions in every trace, so that the electrical histograms are representative of the different binding configurations of the molecule.

By looking at the electrical conductance trace in Figure 5.1b, we can distinguish 3 different transport regimes: (I) Au-Au, (II) Au-molecule-Au, (III) Au-tunneling-Au. During the thinning of an Au-Au point contact (I), the thermal conductance of the junction is proportional to the electrical one, decreasing in a step-like fashion because

---

[2] In this chapter, the letter "k" is used to refer to the thermal conductance, to distinguish between the electron contribution to heat transport k_{el} and the electrical conductance G_{el}

of the quantized availability of electron channels. Most of the heat is transported by electrons following the Wiedemann-Franz law, as shown in chapter 4. Some traces exhibit a second regime (II), in which G_{el} shows a plateau indicating the formation of a molecular junction. Finally, in the last regime (III) the molecular junction is broken. The thermal conductance of the molecule can then be obtained from the signal change around the breaking point of the junction.

The thermal conductance plotted in Figure 5.1b includes both the contributions of the MEMS (~45 nW/K) and the thermal contact with the tip. A similar plateau might be expected for k_{th} in the second regime (II). However, a linear decrease versus tip displacement is usually observed, with slopes ranging between 0.5 and 3 $nWK^{-1}nm^{-1}$. This is caused by an additional thermal conductance path with relatively long range, which can be attributed to thermal near-field radiation, target molecules not specifically bound to both electrodes, and other adsorbates on the gold surfaces originating from the solvent or residues from the fabrication steps of the MEMS. Such adsorbates, sketched as the light green layer in Figure 5.1a, are only weakly bonded to the gold electrodes and make a negligible contribution to the electrical conductance of the junction. Nevertheless, they form a strong mechanical contact between tip and MEMS, with a typical thermal conductance of about 10 to 30 nW/K that depends on their relative distance. Upon retracting the tip, the contact area with the adsorbate layer and the influence of radiation are gradually reduced giving rise to the thermal background observed in the opening traces. This is observed in all the break junction experiments performed on the MEMS, also prior to the molecule deposition and immersion in liquid solvents, as described in chapter 4. Notably, thermal conductance variations versus tip-surface distance with similar slopes were recently measured in near-field heat transport measurements between nominally clean surfaces in UHV, even after thorough in-situ cleaning procedures. This indicates that the contribution of radiation to the distance-dependent thermal conductance at nm distances cannot be excluded and most likely cannot be avoided experimentally [138, 70]. Under stable conditions, the thermal background does not significantly change during repeated opening and closing of the break-junction contact, showing approximately a linear dependence with displacement and keeping the same slope in the region of analysis described below.

The experimental procedure to extract the thermal conductance of a single molecule is firstly illustrated for OPE3s. As in a standard break junction measurement, we typically collect 2000 to 5000 traces per dataset and construct 1D and 2D histograms for the electrical conductance opening traces. In doing so, we rescale the displacement and the thermal conductance axis by shifting their origin to the breaking point of the molecular junction. This means that for every trace that has a defined electrical signature of the molecule, we locate the breaking point of the molecular plateau in the electrical conductance trace and use this to rescale the displacement and thermal conductance axes, Figure 5.2. The offset in the thermal conductance includes the contributions of the MEMS, the adsorbates and near field radiation. Subtracting these effects for each traces allows us to compensate for variations in the thermal contact to the tip without making any prior assumption on their origin. Moreover, traces showing molecular plateaus with different lengths, as normally observed in a break junction measurement, can be combined together to obtain the most probable thermal conductance of the molecular junction. For this reason, the atomic contacts and molecular plateaus

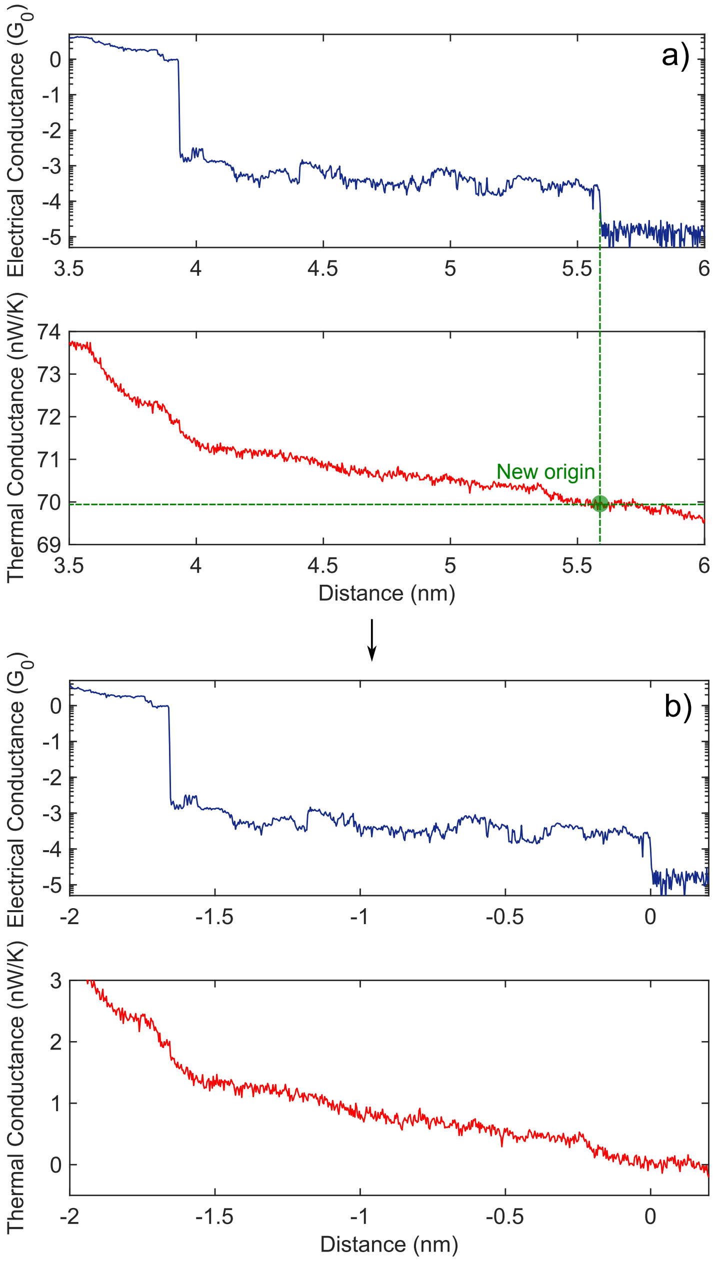

Figure 5.2: Rescaling of a single trace according to the breaking point of the molecular junction. a) Electrical and thermal conductance opening trace as measured. By locating the rupture of the molecular junction in the electrical signal, we can then extract the thermal conductance and displacement offset. b) Rescaled electrical and thermal conductance trace.

appear at negative displacements on the x axis.

Figure 5.3 shows the results obtained for dithiol-OPE3. By looking at the 1D electrical histogram in Figure 5.3a, we first note that the observed single peak in at 2.7×10^{-4} G_0 is in excellent agreement with several independent reports in different environmental conditions [175, 36, 106, 176] indicating single-molecule OPE3 junctions. The 2D histogram also exhibits a clear molecular plateau between

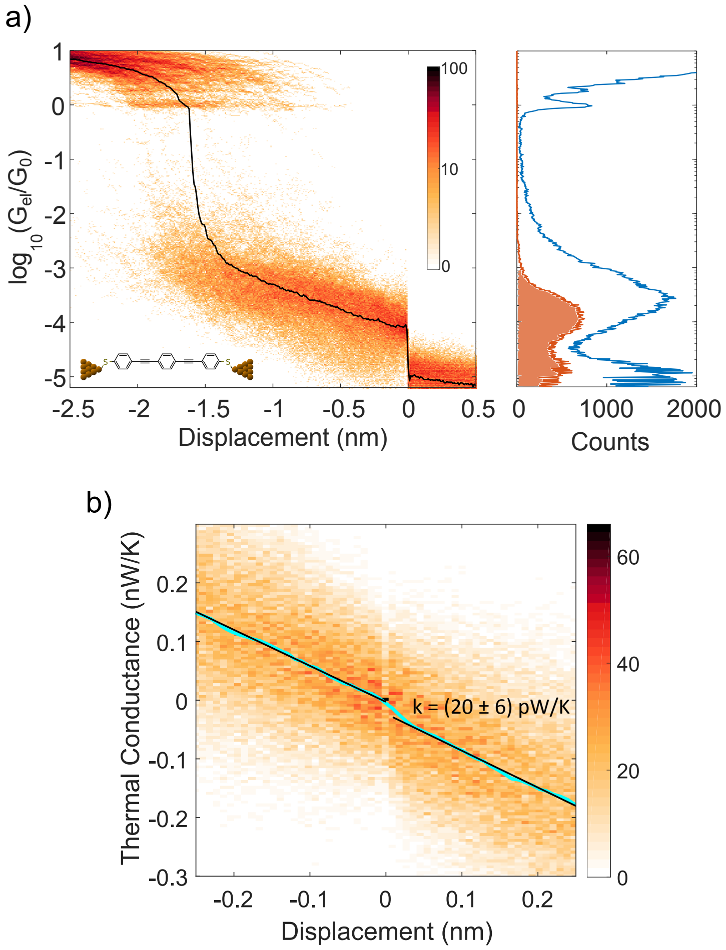

Figure 5.3: Experimental results for OPE3-dithiol. a) Electrical 2D and 1D histograms constructed with 411 traces measured at a fixed voltage of 50 mV and a pulling speed v = 3 nm/s at an angle of 40° with respect to the MEMS surface. From the histograms we can extract the molecular electrical conductance of about 2.7×10^{-4} G_0. The black line represents the median of the 2D histogram. The orange 1D histogram indicates the electrical conductance of the junction before breaking, reconstructed from the 2D histogram in the displacement range between -0.5 nm and 0.2 nm. b) 2D Thermal conductance histogram for OPE3. The mean (light blue) shows a clear step around 0 (breaking point of the molecular junction). The black lines represent the linear fits of the mean before and after the step, giving a thermal conductance k = (20±6) pW/K.

-1.5 and 0 nm, as typically occurring during the stretching process of a molecular junction [40]. Note that in the 2D histogram, all the traces are aligned at the breaking of the junction as indicated by the sharp transition at 0 nm in the median (black line). Since every trace is characterized by a molecular plateau with a different length, the accumulation at 1 G_0, which is normally used as reference for the displacement axis, appears smeared out. The orange 1D histogram has been extracted by adding the counts of the 2D histogram in the displacement range between -0.5 nm and 0.2 nm. In the analysis method presented here, we focus on the molecular junction configuration before breaking; the position of the maximum in the 1D electrical histogram, might be influenced by the stretching process, i.e.

the slope in the molecular plateaus, and therefore it is more accurate to consider the position of the peak in the histogram built with the final portions of the plateaus to compare between different measurements. Note that this does not change the agreement with literature as values between 1.2×10^{-4} G_0 and 2.8×10^{-4} G_0 have been reported for dithiol-OPE3 [180, 36, 176].

In Figure 5.3b, we constructed the 2D histogram of the thermal conductance versus the displacement. The mean of such 2D thermal histogram shows a clear step in the thermal background at the breaking point of the molecular junction (d = 0 nm). To extract the thermal conductance of the molecule, we then take the difference at 0 nm between the linear fits of the mean, giving a value of k = (20±6) pW/K. With this method, even though the contribution of a single molecule to the thermal conductance (∼ 20 pW/K) is on the same order of the rms noise of the measured signal (∼ 25 pW/K to 50 pW/K with an integration time of 1 ms), by taking the mean of the 2D thermal histogram we can average out the random fluctuations occurring during the measurement and extract the molecular signature, boosting the sensitivity of the technique. In fact, the mean shows little variations and similar slopes before and after the junction rupture, apart from the step at 0 nm. The observed change in thermal conductance is not instantaneous, but occurs over about 10 ms (30 pm with a speed of 3 pm/ms) because of the thermal time constant of the tip-MEMS system.

The method described relies on the identification of the breaking point of a molecular junction in the electrical conductance trace, very similarly to what has been done previously for the measurement of breaking forces [181, 182]. We defined criteria to locate the breaking point of the molecular plateaus automatically that were applied to all the datasets. Specifically, we defined as region of interest the electrical conductance range where the molecular plateau is expected, which is 8 to 30×10^{-5} G_0 for OPE3. Molecular plateaus should be at least 50 ms long (∼ 50 to 100 pm at usual perpendicular opening speeds of 1 pm/ms), to avoid artifacts of the thermal low-pass filtering. Traces showing a ratio in electrical conductance before and after the breaking point of the molecular junction lower than 3 are excluded. This condition serves to exclude traces from the analysis which carry significant uncertainty on the configuration of the molecular junction. The only selection condition that we apply on the thermal signal is based on the thermal background slope. Datasets with non-linear or strongly varying background slopes over time indicate unstable experimental conditions and were not utilized in this work. In fact, the scatter in the mean and corresponding fitting uncertainty would be too large to be considered as significant results. Few examples of selected and discarded traces are reported in Figure 5.4.

5.2.1 Experimental results with octane-dithiol molecular junctions

The same experimental and theoretical methods were applied to study the thermal transport properties of ODT (Figure 5.5). In contrast to OPE3, the junction dynamics of ODT show stronger variation, as confirmed in independent reports. The different conductance values observed are attributed to various binding configurations of the S-Au bond [56, 183], gauche defects [176, 184] and a higher likeliness to observe multiple-molecules in a single junction [177, 185]. Nevertheless, there is consensus about the frequently observed electrical conductance of 5×10^{-5}

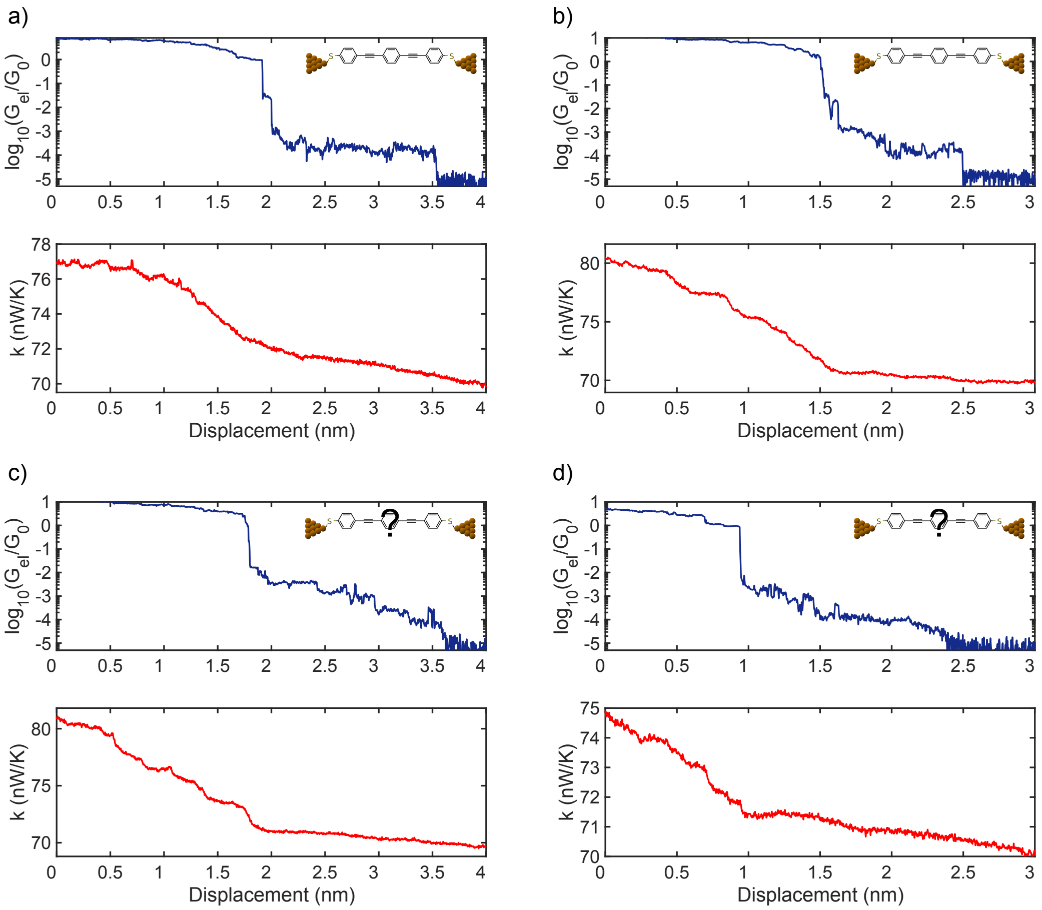

Figure 5.4: Examples of single opening traces for OPE3. a-b) Selected traces used to build the histograms reported in Figure 5.3. c-d) Discarded traces, because not showing clear breaking of the molecular junction.

G_0 [56] relating to the atop-atop configuration (thiol group binding to a single gold atom) of a single stretched ODT the molecule. Most of the histograms show a prominent peak between 5 and 7 $\times 10^{-5}$ G_0, which we attribute to the atop-atop configuration. With lower probability, we observe plateaus at 1×10^{-5} G_0 and at about 1×10^{-4} G_0, in agreement with a recent robust statistical approach [176]. Therefore, to simplify the analysis of the thermal signal, we consider molecular traces with plateaus between 2 and 8×10^{-5} G_0. Examples of selected and discarded traces are shown in Figure 5.6. For this junction configuration, we obtain a thermal conductance k = (29±8) pW/K, which is higher than the one of a single OPE3 molecule, in contrast to the lower electrical conductance. Indeed, as we will see in section 5.5, the thermal conductance of these molecular junctions is dominated by the contribution of phonons. For the first time, we can therefore study phonon transport across single molecules and investigate the influence of the chemical structure of the molecular backbone.

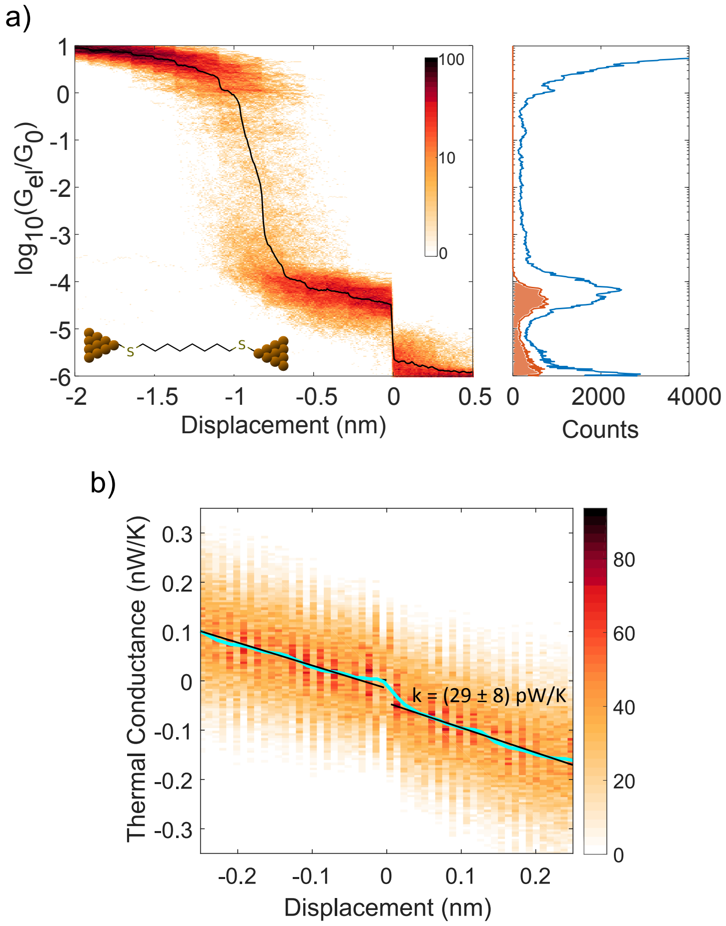

Figure 5.5: Experimental (a-b) and theoretical (c-d-e) results for octanedithiol (ODT). a) Electrical 2D and 1D histograms constructed with 615 traces measured at a fixed voltage of 90 mV, a pulling speed v = 3 nm/s at an angle of 40° with respect to the MEMS surface. From the histograms we can extract the most probable molecular electrical conductance of about 7×10^{-5} G_0. Note that the peak shifts to 5×10^{-5} G_0 before breaking (orange 1D histogram). b) 2D Thermal conductance histogram. The mean (light blue) shows a clear step around 0 nm (breaking point of the molecular junction), giving a thermal conductance k = (29±8) pW/K.

5.2.2 Reproducibility of the measurements

The results presented have been reproduced by performing different measurements on two MEMS samples for each molecule. Figure 5.7 shows the results obtained for OPE3. In particular, the data presented in Figure 5.7a was collected by moving the tip by 100s of nanometers to a different location on the MEMS surface used in Figure 5.3 (Sample 1). Note that even though the electrical conductance peak in the 1D histogram (blue) is slightly shifted to higher values, the orange histogram, corresponding to the breaking configuration, agrees well with the other reported datasets, with a peak around 1.2×10^{-4} G_0. Figure 5.7b shows the result obtained on a different MEMS design (Sample 2). The details about the sample preparation are provided in section 5.3. The shorter plateau length visible in the 2D histogram agrees well with previous reports [36] and it may indicate a different stretching

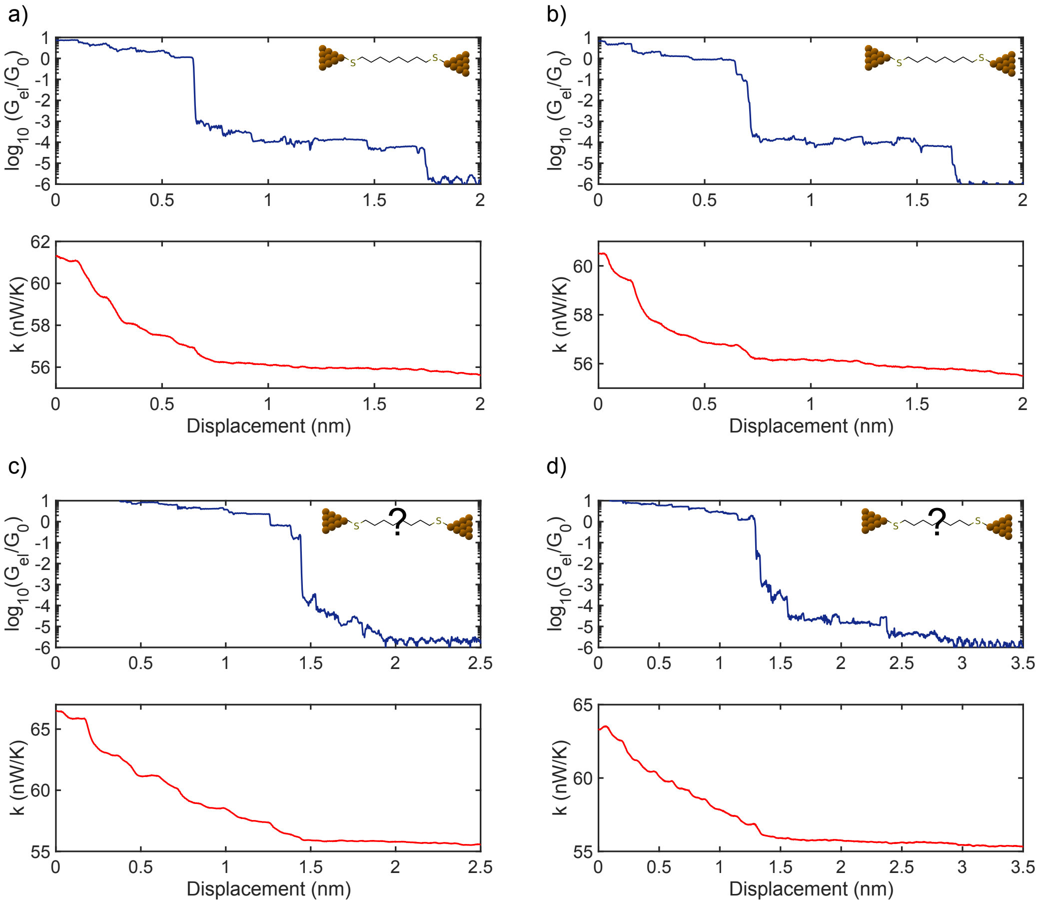

Figure 5.6: Examples of single opening traces for ODT. a-b) Selected traces used to build the histograms reported in Figure 5.5. c-d) Discarded traces, because not showing clear molecular plateaus (c) or breaking of the molecular junction (d).

mechanism of the molecular junction. For instance, a larger snap-back of the gold electrodes [37] may be reflected in the small number of counts at G_0. Note however that the displacement scale along the pulling direction carries significant uncertainty, as it is calculated from the nominal conversion factors of the piezo-scanner between applied voltage and distance, and by considering the angle with respect to the MEMS surface. In practice, non-ideality in the scanner motion together with the gold surface roughness may have a significant effect on the actual displacement at the atomic scale. Among all the measurements shown in Figures 5.3 and 5.7 we find good agreement in the thermal conductance extracted from the 2D histograms within the experimental uncertainty. The error bars for the thermal conductance values are different for each dataset as their calculation takes into account the number of traces used to construct the 2D histogram, the scatter in the data and the noise in the mean. A detailed description of the uncertainty calculation is provided in section 5.4.

Figure 5.8 collects the results obtained for ODT. All the 1D electrical histograms show a molecular conductance peak centered around $5{\times}10^{-5}$ G_0 as expected by the selection of traces in the conductance region between 2 and 8×10^{-5} G_0. As mentioned before, this was done to extract the thermal conductance of ODT in the

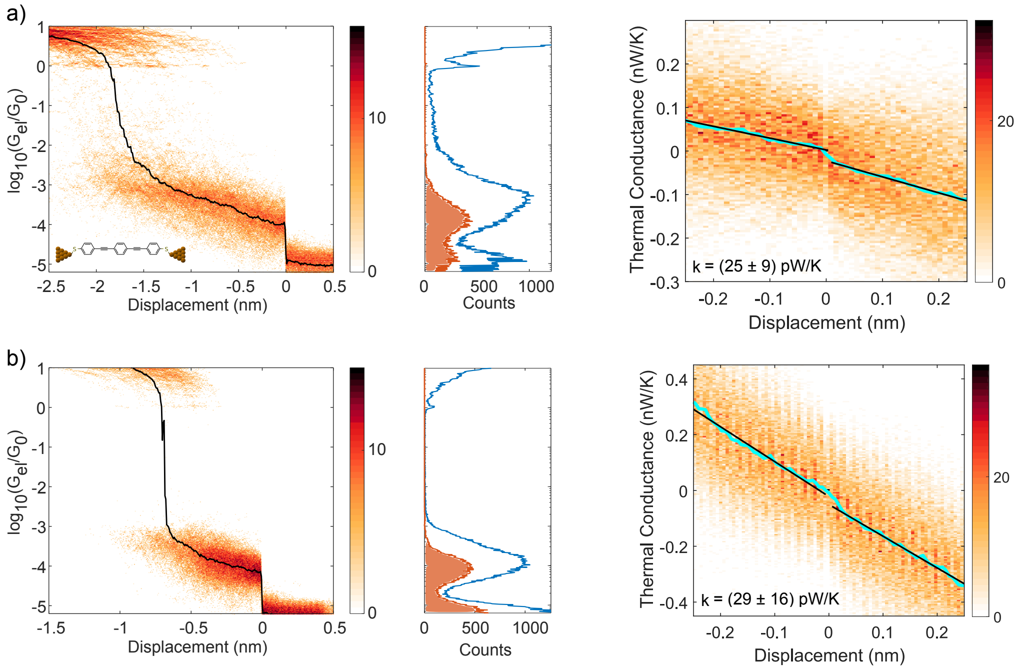

Figure 5.7: Experimental results obtained for OPE3-dithiol. a) The histograms are built from 223 traces measured at a fixed voltage V = 50 mV, angle = 40° and opening speed v = 3 nm/s along the pulling direction (Sample 1). b) The histograms are built from 310 traces measured at 40 mV, angle = 30°, v = 2nm/s (Sample 2).

atop-atop configuration, which is formed with a higher probability in agreement with previous reports [176]. For all the measurements, the thermal conductance extracted for a single ODT molecule take values around 40 pW/K, in agreement with the result reported in Figure 5.5 within the experimental uncertainty.

The thermal conductance measured for both OPE3 and ODT did not show any dependence on the experimental conditions. Similar values are obtained by performing STM-BJ measurements on different spots on the MEMS and with different MEMS designs with angles between the beams of 45° and 10°. Pulling speeds between 1 and 5 nm/s at approaching angles of 20° to 40° yielded also similar results. Moreover, all the measurements were performed in a ΔT range between 20 and 50 K depending on the thermal conductance of tip-MEMS system. Within the uncertainty, no temperature dependence was observed, as expected in this high temperature regime, see 5.5.

We collected several independent evidences to demonstrate that the experimental technique presented here is not affected by systematic changes of the thermal background upon breaking of the molecular junctions, due to a mechanical backlash of the MEMS. First, the same data analysis was applied to the gold-gold contact regime, Figure 5.9. To do this, we took into account traces showing plateaus at least 20 ms long in the conductance range between 0.8 and 1.2 G$_0$. With the same code used for the molecular junctions, we aligned the thermal conductance traces at the breaking of the single atom plateau and built the 2D thermal histogram versus displacement, Figure 5.9a. In this graph, the origin of the displacement axis indicates the transition between gold contact and tunneling regime. Because

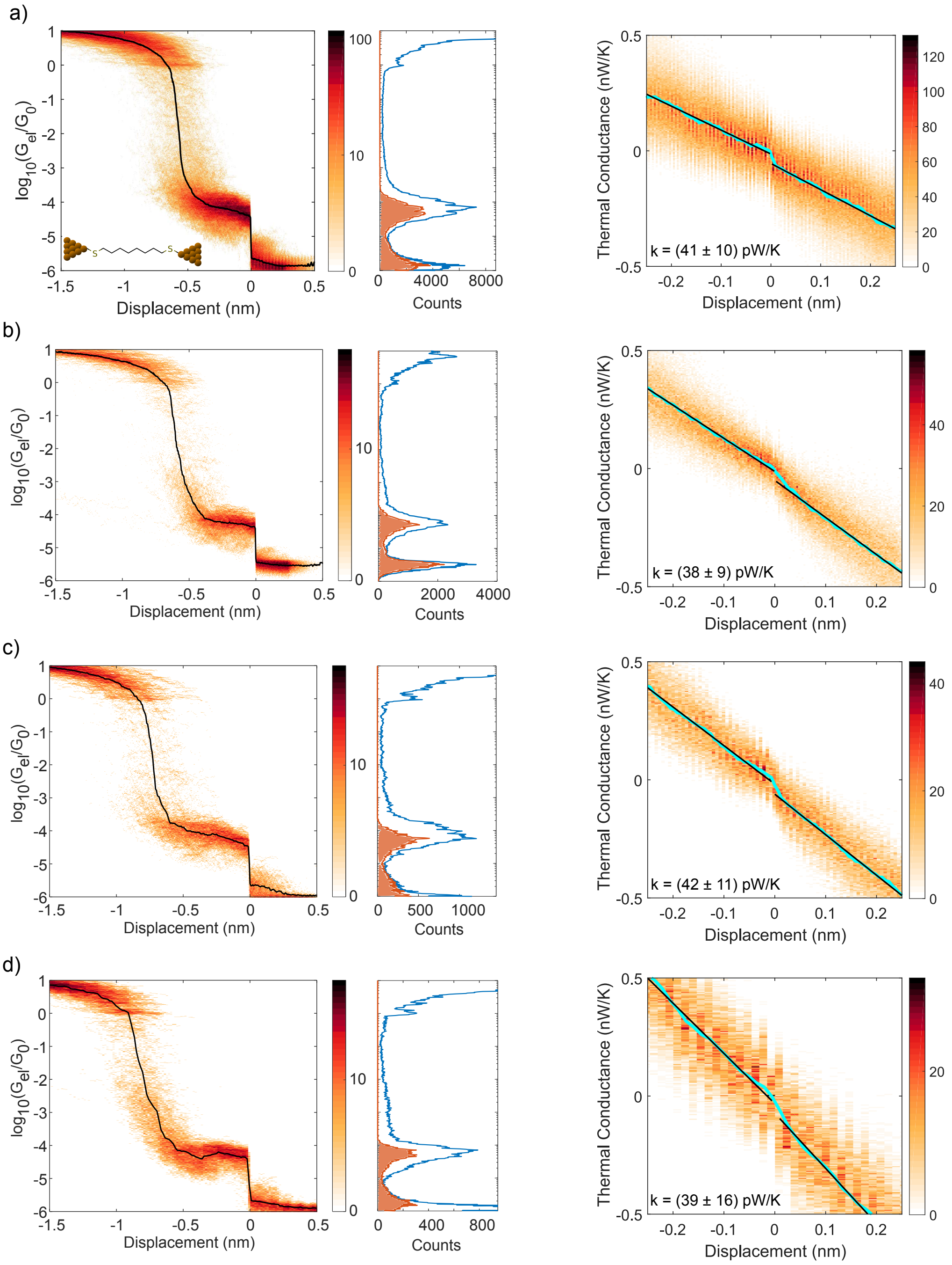

Figure 5.8: Experimental results obtained for OPE3-dithiol. All the histograms were measured at V = 90 mV: a) Sample 1, 1130 traces, Angle = 23°, v = 1.3 nm/s along the pulling direction. b) Sample 2, 301 traces, Angle = 25°, v = 1.3 nm/s. c) Sample 1, 254 traces, Angle = 27°, v = 2.2 nm/s. d) Sample 1, 316 traces, Angle = 23°, v = 5 nm/s.

of the different trends in the two regimes (characteristic of the respective heat transport mechanisms), we extrapolated the mean of the thermal background after reaching thermal equilibrium ($x > 0.15$ nm) up to the contact breaking. In this way, we obtain a thermal conductance of 540 pW/K, which is very close

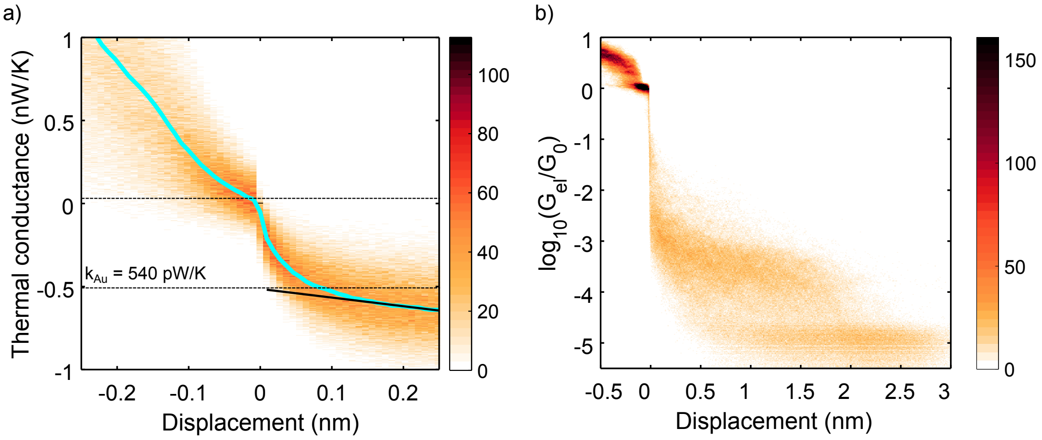

Figure 5.9: 2D thermal and electrical conductance histograms of gold quantum point contacts. The histograms are obtained by applying the same data analysis method to the OPE3 dataset shown in Figure 5.3, in the electrical conductance range 0.8 $G_0 < G < 1.2\ G_0$, and are built with 991 traces showing plateaus at least 20 ms long.

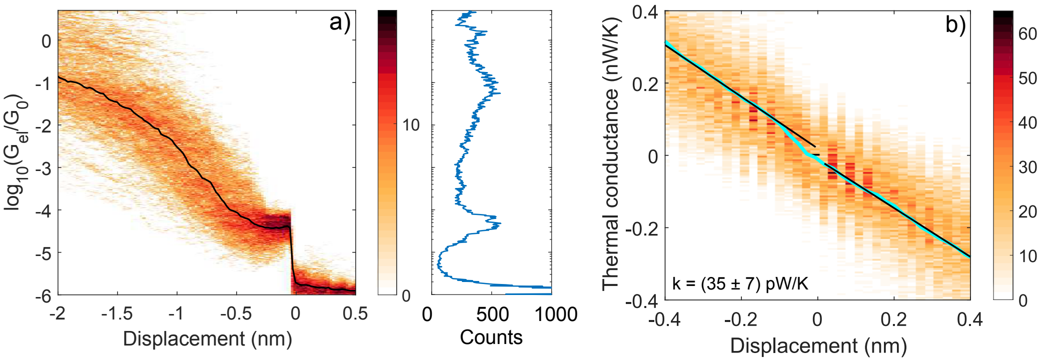

Figure 5.10: Example of electrical (a) and thermal (b) conductance histograms obtained for ODT by using the closing curves. The histograms were built with 440 traces and measured at V = 90 mV with an angle = 23° with respect to the MEMS surface. In this case, x = 0 nm corresponds to the formation of the molecular junction.

to the value predicted by the Wiedemann-Franz law k_Q = 577 pW/K, for one electrical conductance quantum at T = 305 K (average junction temperature during the measurement), in agreement with the results reported in chapter 4 and in an another independent study [69]. This finding confirms that the microscopic rearrangements occurring at the breaking of the contact have a minor influence on the thermal conductance extracted by the analysis method presented.

Interestingly, the formation of molecular junctions, as indicated by the typical OPE3 molecular conductance plateaus between 10^{-3} G_0 and 10^{-4} G_0 in the 2D electrical histogram in Figure 5.9b, does not affect the thermal conductance extracted for the single atom contact. A single OPE3 molecule in parallel to a gold atom would indeed bring a negligible contribution to both the electrical and thermal conductance measured, in contrast with the results shown in section 4.1.2.

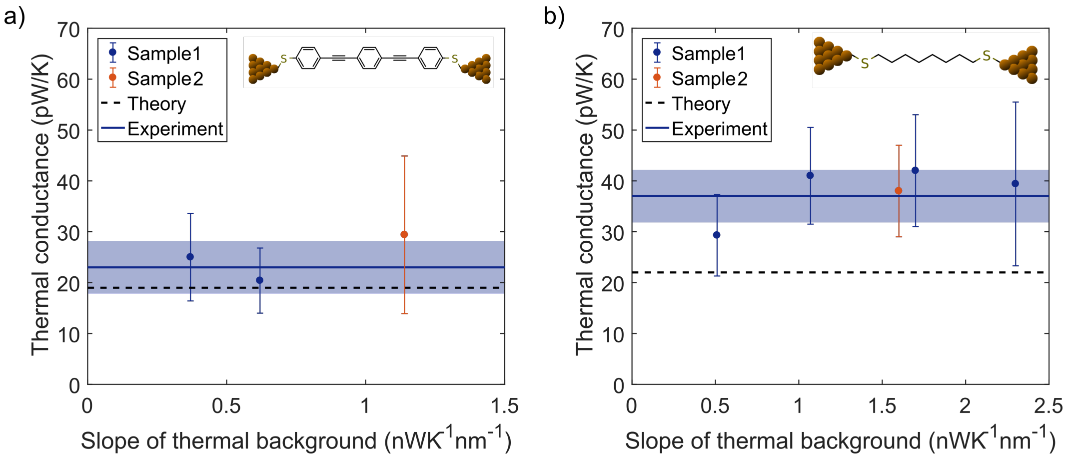

Figure 5.11: Summary of the experimental results obtained for OPE3 (A) and ODT (B). By performing the weighted average of the different experimental datapoints for each molecule we obtain k = (23±5) pW/K for OPE3 and k = (37±5) pW/K for ODT. The experimental uncertainty is represented by the shaded region around the mean value (blue line).

A second evidence that the thermal conductance measured is not affected by systematic changes in the thermal background comes from the analysis of the closing traces. In the case of ODT, we obtained similar values of thermal conductance of k = (35 ± 7) pW/K upon forming molecular junctions within closing traces, Figure 5.10. In the break-junction measurements, we typically set approach and retraction speeds independently in order to maximize the throughput of measured traces. In particular, it was found empirically that faster closing speeds can improve the formation of clean molecular junctions. For this reason, in Figure 5.10b, the junction was closed at 7.5 nm/s along the motion direction, making the thermal conductance step in the histogram mean to shift to negative displacements with respect to the origin (ODT junction formation). In fact, the thermal conductance change occurs over a distance of about 0.1 nm along the approaching direction, corresponding to a time interval of 13 ms, close to thermal time constant $\tau = 22$ ms of the isolated MEMS[3]. The formation of a molecular junction during the approaching cycle is a thermally activated process. This phenomenon is typically exploited in the so called I(s) technique [176, 186, 187], where the spontaneous attachment of molecules prior to the metallic contact formation (the junction is not fully closed like in a break-junction measurement) is used to measure the electrical conductance of molecular junctions. While the rupture of a molecular junction releases a force (on the order of 1 nN) that might induce a change in thermal background, the thermally activated junction formation is expected to have a negligible influence on the tip-MEMS distance. Therefore, the agreement between the results obtained with the opening and closing traces confirms that the distance variation of the thermal background is independent of the thermal conductance change occurring at the breaking of a molecular junction.

Finally, a mechanical backlash at the tip-MEMS contact would lead to an apparent step in the thermal conductance trace in proportion to the slope of the

---

[3] When the tip is contact with the MEMS, the thermal conductance of the system increases leading to an effective faster time response.

thermal background. To test this, we plot in Figure 5.11 the thermal conductance obtained from all the measurements that have just been presented, versus the thermal background slope extracted from the linear fit of the histogram mean at displacements x > 0 nm. Within our uncertainty, we do not observe any significant dependence of the thermal conductance of OPE3 and ODT on the background slope. We can then calculate the weighted average $\bar{k}$ and standard deviation $\sigma_{\bar{k}}$ of the ensemble of measurements starting from the values k_i and standard deviations σ_i (see section 5.4) of each datapoint and using

$$\bar{k} = \frac{\sum_{i=1}^{n} k_i \sigma_i^{-2}}{\sum_{i=1}^{n} \sigma_i^{-2}} \tag{5.1}$$

and

$$\sigma_{\bar{k}} = \frac{1}{\sqrt{\sum_{i=1}^{n} \sigma_i^{-2}}} \tag{5.2}$$

In this way we obtain $\bar{k} = (23 \pm 5)$ pW/K for OPE3 and $\bar{k} = (37 \pm 5)$ pW/K for ODT.

5.3 Sample preparation

Cleaning the gold surface on the MEMS devices is performed by a combination of oxygen plasma and ion milling. Before depositing the molecules, the samples are cleaned by oxygen plasma (400 W for 5 min) to remove resist residues and other hydrocarbons. We then perform an Ar - ion milling step (beam current 150 mA with 30 cm as beam diameter for 20 s) to physically clean the top surface. After cleaning the MEMS, we immerse it in the solution of the target molecules. In the case of OPE3, we obtained the molecules with acetyl-protected thiol groups from Sigma Aldrich and an additional purification step (purity $\geq$ 99%) was then performed by our collaborators at the University of Basel. For the deposition, Sample 1 was immersed in a solution of dichloromethane (DCM) with concentration c = 1 mM for 2 min. Two equivalents of tetrabutylammonium hydroxide (i.e., one TBAH molecule per acetyl group) were added to the solution to deprotect the thiol groups and improve the formation of the S-Au bond. A similar procedure was employed for Sample 2, but with c = 0.25 mM for 30 min. In both cases, the MEMS samples were then rinsed in a mixture of clean DCM and ethanol and carefully dried under N_2 flow. In the case of ODT, we obtained the molecules from Sigma Aldrich (purity $\geq$ 97%) and used ethanol as a solvent. Sample 1 was immersed in a solution with c = 1.2 mM for 30 s, then rinsed twice in clean ethanol and dried with N_2. Similarly, for Sample 2 we used c = 0.3 mM and 30 s.

The sample preparation is a critical step and determines the yield and quality of the measurement. Too long exposures to the molecular solution usually results in a dense monolayer on the MEMS surface hindering the reliable formation of single molecule junctions. On the other hand, short deposition times can produce films with low coverage, reducing the probability of junction formation. The suitable combination of immersion times and solution concentration was determined empirically during the PhD project. In the case of ODT, few samples were prepared with a concentration of c = 0.3 mM and deposition times of 15 to 30 minutes. On the gold pad on the substrate, high quality electrical histograms were measured, showing molecular peaks in the expected conductance range. However, on the MEMS, the formation of gold contacts was hindered by the molecular film, making the break junction measurement mechanically unstable. This was confirmed by the formation of large thermal contacts with fluctuating thermal background.

In the case of OPE3, longer deposition times are usually needed to obtain a good junction formation probability (with 20% to 50% of the traces showing molecular plateaus). The preparation procedure involves the use of a deprotecting agent to cleave the acetyl group attached to the sulfur atom, which serves to avoid the formation of disulfide compounds in presence of oxygen [188, 11]. The use of tetrabutylammonium hydroxide is widely adopted for STM-BJ experiments with dithiol-OPE3 [36, 106], however direct adsorption of acetyl-protected molecules was reported as alternative for single molecule measurements [106] and for the formation of monolayers [189, 188]. This is particular attractive as it simplifies the sample preparation step and avoids the formation of longer compounds due to the oxidation of deprotected molecules, which may contribute to parasitic heat conduction (thermal background). However, direct adsorption of OPE3 with different deposition times yielded poor results in terms of junction formation. In the future, further investigations of the influence of oxygen during the deposition of acetyl-protected dithiols may provide insights into the effects on the thermal background of disulfides and other deposition byproducts.

5.4 Uncertainty calculation of experimental data

The uncertainty reported for the thermal conductance of the molecular junctions are composed of 2 main contributions: the RMS error of the 2D distribution ϵ_d and the error obtained by subtracting the linear fits of the thermal background. In the first case, we calculate the RMS error of the datapoints in the 2D histogram from the calculated mean at x = 0.1 nm and divide it by the square root of the number of traces used to build the histogram. Note that as the width of the histogram is homogeneous around the breaking point (x = 0), the RMS error does not change if calculated at another displacement value (e.g. x = -0.1 nm). To evaluate the error in extracting the step height from the linear fits, we consider the RMS error of the fit with respect to the mean of the 2D histogram within the fit range before and after the breaking point, respectively ϵ_b and ϵ_a. Finally, the total uncertainty is given by

$$\epsilon_{tot} = \sqrt{\epsilon_d^2 + \epsilon_b^2 + \epsilon_a^2} \tag{5.3}$$

For instance, for the OPE3 dataset shown in Figure 2, we obtain in the fit range: $\epsilon_d = 5$ pW/K, $\epsilon_b = 2.8$ pW/K (fit range -0.4 < x < -0.02) and $\epsilon_a = 2.8$ pW/K (0.02 < x < 0.4) corresponding to $\epsilon_{tot} = 6.4$ pW/K. The fit range is always taken symmetric with respect to the breaking point. Variations in the step height that can result from the noise in the mean are included in the uncertainty range calculated with this method. To further check the robustness of the data analysis method, we verify that mean and median of the 2D histograms give the same result within 10%. The median is less sensitive to the occurrence of outliers in the histogram and therefore a useful cross-check of the quality of the data.

5.5 Comparison with theory and previous experiments

The simulation of vibrational heat transport across molecular junctions (single or self assembled monolayers) present numerous challenges related to the intrinsic non-equilibrium nature of the problem, involving many-body interactions and quantum effects [45, 6]. Fourier's law is not valid in 1D systems at the nanoscale. In fact, its formula

$$\dot{Q} = -\kappa \nabla T \tag{5.4}$$

where $\dot{Q}$ is the heat flux, κ the thermal conductivity and ∇T the temperature gradient, implies diffusive energy transfer and relies on the definition of local heat flux and temperature field, which are not well defined concepts at the atomic scale and assume local equilibrium [190, 191, 45]. The heat transport properties of molecular chains between macroscopic electrodes are better characterized by their thermal conductance $k = \frac{\dot{Q}}{\Delta T}$, where ΔT is the temperature difference between the leads. To answer the questions related to the nature of transport (ballistic or diffusive), quantum effects [6], anharmonicity [5], electron-phonon and electron- electron interaction [45, 192, 193], non linear effects [13], role of the coupling strength of the molecules to the electrodes, several theoretical models have been developed. The two main approaches are Molecular Dynamics (MD) simulations and Green's function techniques, each with its own advantages and limitations. Molecular Dynamics has been widely used to study heat transport across SAM interfaces with different materials [194, 9, 195, 196, 172], to determine the interfacial thermal resistance. Basically, it consists in solving numerically the classical Newton equations of motion by assuming certain interaction potential between the atoms. It can be used to simulate heat transport in realistic structures and far from equilibrium, however it generally does not include quantum effects. Thus, the results obtained from MD are valid in the high temperature regime, where phonons obey Boltzmann statistics. However, since the vibrational energies of the molecules extend typically above room temperature, Bose-Einstein statistics cannot be neglected. For this reason, interfaces in MD simulations of sandwiched SAM structures are found to act independently, which is not always the case, e.g. when two different metals are used for the electrodes [9].

On the other hand, in the basic form of the Green's function approach, one typically assumes a Landauer type of transport and the phononic thermal conductance of the molecular junction k_{ph} is proportional to the transmission probability of phonons $T_{ph}\omega$ In particular, the phonon thermal conductance k_{ph} at temperature T can be directly calculated from the phonon transmission $T_{ph}(\omega)$ by using

$$k_{ph}(T) = \frac{1}{2\pi} \int_0^\infty \hbar\omega T_{ph}(\omega) \frac{\partial f_{BE}(\omega, T)}{\partial T} d\omega \tag{5.5}$$

where $f_{BE}(\omega, T) = \left(e^{\hbar\omega/k_B T} - 1\right)^{-1}$ is Bose–Einstein distribution function and $\hbar = 4.14 \times 10^{-15}$ eV is reduced Planck's constant and $k_B = 8.6 \ \times 10^{-5}\ eV/K$ is Boltzmann's constant. The phonon transmission $T_{ph}(\omega)$ is typically calculated in terms of single particle Green's function in combination with the mean field hamiltonian of the junction obtained with Density Functional Theory (DFT), from which the dynamical matrix describing the harmonic response of the junction is calculated. This method describes single particle coherent transport, in which inelastic processes are assumed to occur only in leads and the force interactions between the atoms in the junction are calculated within the harmonic approximation. It has been developed by several groups to study heat transport across single molecular junctions [45, 6, 5, 18, 44] and in general it is valid if the phonon mean free path is larger than the junction size. The main advantage of this ab-initio method is that it has an intrinsically quantum nature and thus suitable to study phonon quantum interference [14, 7, 12]. However, being a one particle problem, the interactions between the carriers involved in transport (e.g. phonon-phonon, electron-phonon) are not included. The leads are then ideal objects imposing the boundary conditions (e.g. T difference, chemical potential...) to the transport problem, as no dynamic interaction with the environment is allowed. Then, because inelastic processes take place only in the leads, the temperature distribution along the junction is assumed to be homogeneous and non-linear phenomena, like memory effects or rectification cannot be considered. Finally, as DFT is a ground state theory, care has to be taken when simulating non-equilibrium problems like heat transport. Having said so, in the linear regime (small ΔT), this method demonstrated to be very powerful, predicting general results like the phonon thermal conductance quantization in one dimensional systems [48], which was later confirmed experimentally [50]. In molecular junctions, this method has become recently quite popular to engineer the thermal conductance of molecules for thermoelectric applications [14, 197] and study phonon quantum interference arising from atomic substitutions in the molecular backbone, the effect of the anchoring groups [198] or Fano-resonances induced by side groups [7].

To conclude this overview on the theoretical methods, the effects of interactions in the system can be included via the so called Non Equilibrium Green's functions formalism (NEGF). This method was successfully applied for instance to study heat dissipation in current carrying molecular junctions [45, 199, 193] and thermoelectric effects [200]. The main difference with the equilibrium approach is that the system under study is described by a dynamical matrix or more generally by an hamiltonian which includes anharmonic interactions (higher order terms of the expansion of the elastic potential) and other effects of interest (e.g. the dynamical matrix is temperature dependent or the hamiltonian depends on the voltage applied).

Thermal transport across the molecular junctions of dithiol-OPE3 and octanedithiol was simulated by our collaborators at the University of Lancaster, Dr. Hatef Sadeghi, Dr. Sara Sangtarash and Dr. Colin Lambert. By using a combination of density functional theory (DFT) and Green's function scattering method within the framework of coherent transport described with the Landauer formalism [14, 18, 201], they calculated the thermal conductance due to phonons and electrons from the respective transmission functions (see equation 5.5). Similarly the electrical conductance $G_{el}\left(T\right) = G_0 L_0$ and the electronic contribution of the thermal conductance $k_{el}\left(T\right) = (L_0 L_2 - L_1^2)/hTL_0$ are calculated from the electron transmission coefficient $T_{el}\left(E\right)$ where the momentums $L_n(T)$ are defined as

$$L_n(T) = \int_{-\infty}^{+\infty} dE \ \left(E - E_F\right)^n \ T_{el}\left(E\right) \left(-\frac{\partial f_{FD}(E,T)}{\partial E}\right) \tag{5.6}$$

and $f_{FD}\left(E,T\right) = \left(e^{(E-E_F)/k_B T} + 1\right)^{-1}$ is the Fermi-Dirac probability distribution function, T is the temperature, E_F is the Fermi energy, $G_0 = 2e^2/h$ is the conductance quantum, e is electron charge and h is the Planck's constant. The

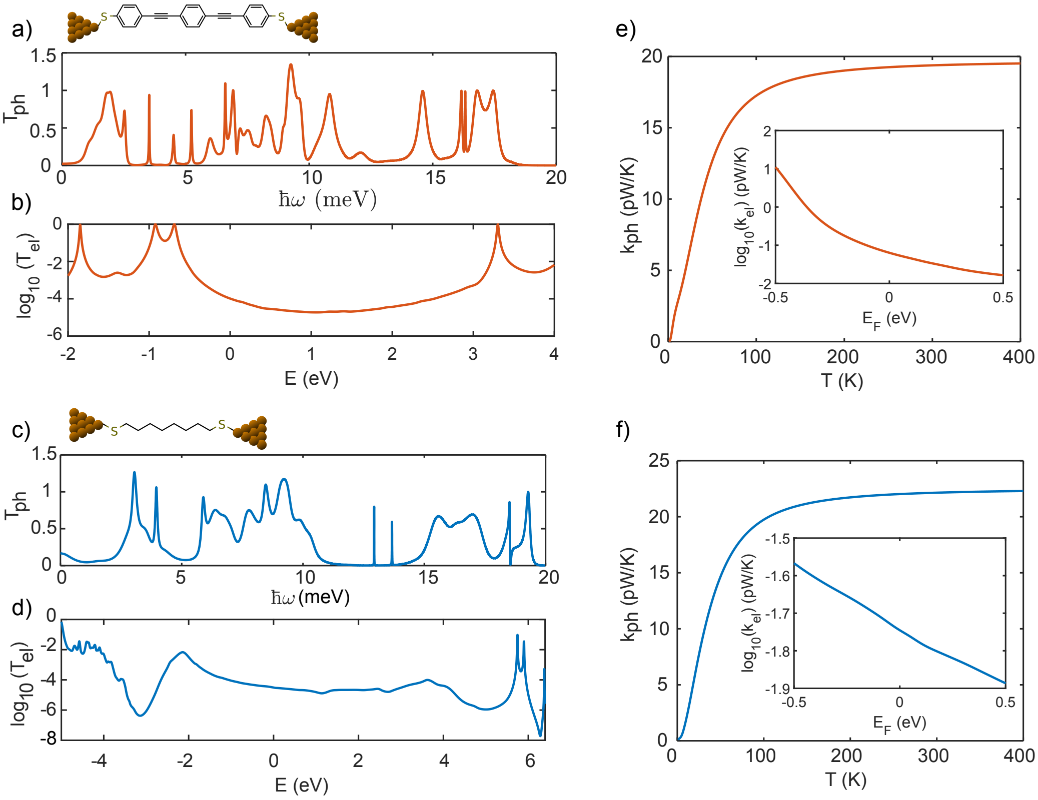

Figure 5.12: Theoretical calculations for OPE3 (a-b-e) and ODT (c-d-f). a-c) Transmission coefficient T_{ph} of phonons with energy $\hbar\omega$. b-d) Transmission coefficient T_{el} of electrons with energy E. e-f) Calculated thermal conductance k_{ph} due to phonons versus temperature T. The inset shows the thermal conductance due to electrons versus the Fermi energy at room temperature.

details of the computational methods are provided in Ref. [18].

The results of the simulations for OPE3 and ODT (in the atop-atop configuration) are summarized in Figure 5.12. The phonon transmission coefficients T_{ph} of OPE3 and ODT are truncated at energies higher than 20 meV, because of the phonon density of states of the gold electrodes [200, 14], Figure 5.12a and c. Moreover, due to low Debye temperature of gold ($T_D = 165$ K) the phonon thermal conductance for temperatures higher than ∼200 K saturates to 19 pW/K for OPE3 and 22 pW/K for ODT, Figure 5.12e and f. The method assumes harmonic approximation to calculate the dynamical matrix of the molecular junctions and the temperature dependence enters in the phonon thermal conductance k_{ph} through the Bose-Einstein distribution. For both molecules, the electron transmission T_{el} is dominated by their highest occupied molecular orbitals (HOMO) as expected for thiol anchoring groups [36], Figure 5.12b and d. In addition, the room temperature thermal conductance due to electrons is calculated from the electron transmission T_{el} as a function of the electrodes Fermi energy E_F, as shown in the inset of Figure 5.12e and f. At the DFT Fermi energy ($E_F = 0$), the thermal conductance due to electrons is about 0.07 pW/K for OPE3 and 0.02 pW/K for ODT, much smaller than the phonon contribution.

In the case of OPE3, we find excellent quantitative agreement between our

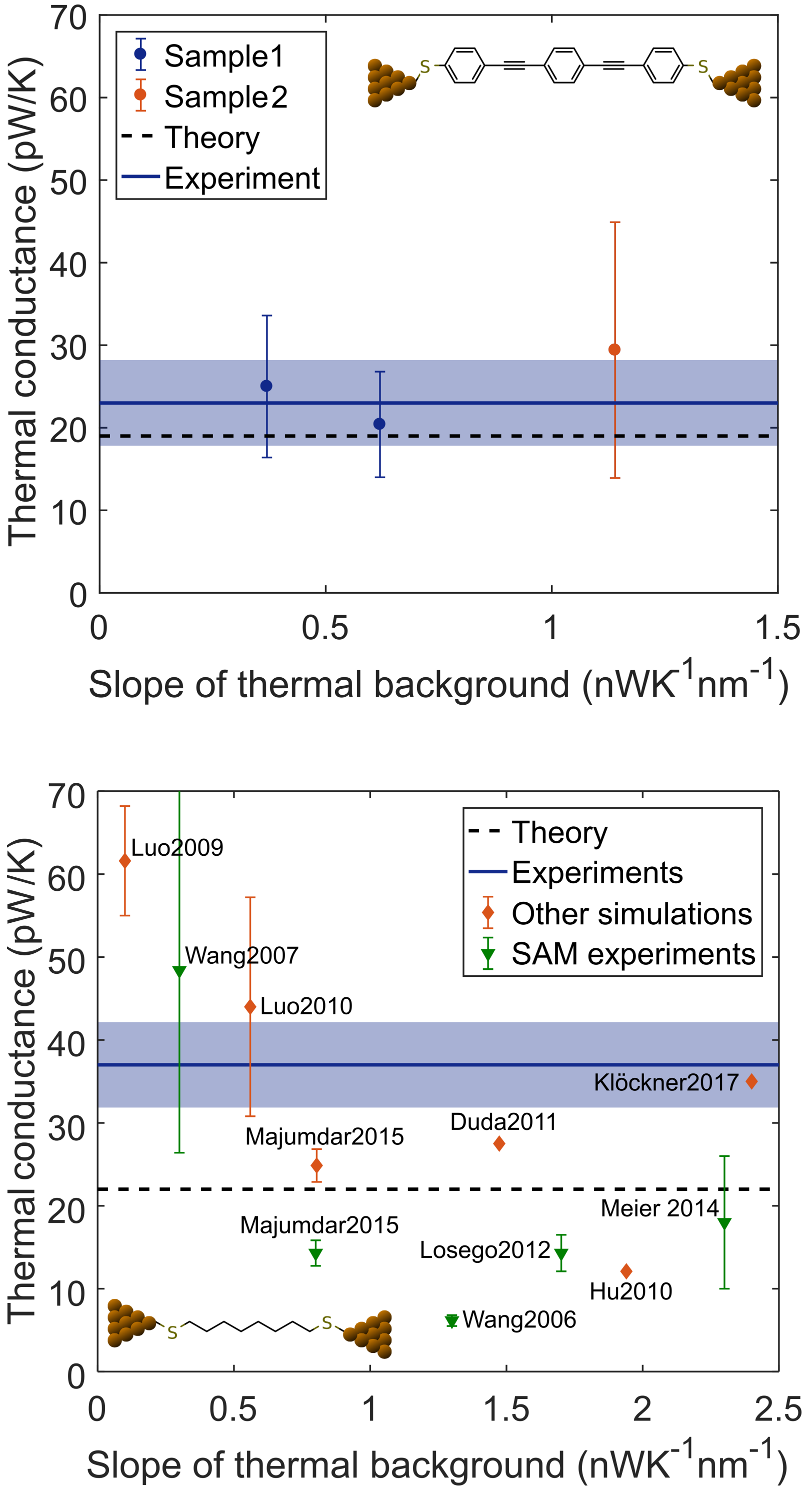

Figure 5.13: Summary of the experimental results obtained for OPE3 (top) and ODT (bottom), in comparison with the theoretical predictions and available measurements and simulations in literature. In the case of ODT (bottom), we added the results from MD simulations (Luo2009 [195], Luo2010 [196], Majumdar2015 [9] and Hu2010 [172]), ab-initio simulations (Klöckner2017 [44]) and other theoretical approaches (Duda2011 [174]). Moreover, for direct inter-comparison, we adapted the main results obtained on the thermal interface conductance of SAM: Wang2007 [202], Majumdar2015 [9], Losego2012 [8], Wang2006 [10], Meier 2014 [4].

simulations and the experiments, Figure 5.13. Considering the history of molecular electronics, this was partly unexpected at the first measurement attempts. This also confirms that the Landauer formalism within the harmonic approximation can be used to simulate phonon transport in these short molecular junctions under small temperature and voltage differences. Heat transport of the thiol-bound OPE3 system has not been studied before, but there are simulations (based on a similar ab-initio approach) for Au-OPE3-Au junction using amine anchor groups [44] yielding $\sim$ 24 pW/K, suggesting a very similar bonding strength of the respective anchor groups. Simulations of OPE3 bound to silicon [12] predicting $\sim$ 60 pW/K highlights the role of a higher Debye temperature of Si compared to Au electrodes, which allows higher frequency phonon transport leading to higher thermal conductance.

To discuss the results obtained for ODT, it is worth to consider also the numerous predictions and experiments present in literature. Thermal transport through SAMs of alkane thiols between different materials, in contrast, have been studied using many methods, both theoretically and experimentally, mainly focusing on SAMs. The results in which the molecules are linked to at least one gold electrode via the thiol bond are included in Figure 5.13 for comparison with our measurements, after the conversion from the typical units of MW/(m^{2}K) to pW/K, considering a SAM density of thiol-alkanes on gold of 0.22 nm^2 [11, 4]. Unfortunately, we are not aware of any experiments of octane-dithiol films sandwiched between gold electrodes. The closest system with a SAM of C10-S2 on gold was characterized in two separate studies by Majumdar et al. (Majumdar2015) [9, 43] with Frequency Domain Termoreflectance (FDTR), reporting values of 14 pW/K, in contrast with the higher values predicted by NEMD simulations of about 25 pW/K. This discrepancy was attributed to the lower effective number of molecules contacting the electrodes because of their surface roughness, estimated to 54 % of the total. As heat transport along alkanes with more than 8 C atoms is fairly length independent [5, 174, 4, 10, 44], the results obtained with longer alkane chains can be compared with our data.

In Figure 5.13 we also added data obtained for different systems and measurement techniques: Au-S-C8-S-GaAs with 3ω (Wang2006), Au-S-C8-CH3-SiO2 with Scanning Thermal Microscopy (Meier2014), Au-S-C11-Si-Quartz with Time Domain Termoreflectance (Losego2012) and Au-S-C8-CH3 with vibrational sum-frequency generation spectroscopy (Wang2007). Interestingly, the scatter in the data and simulations is very similar, even if slightly different systems are considered, with most of the results falling in the range between 15 and 50 pW/K. More importantly, our measured value of 37$\pm$5 pW/K is in excellent agreement with the range obtained from NEMD simulations (25 pW/K, Majumdar2015, and 43 pW/K, Luo2010) and ab-initio methods (22 pW/K and 35 pW/K, Klockner2017) on octane-dithiol between gold electrodes. This agreement with predictions given by two very different theoretical frameworks suggests that in this system heat transport is mainly dominated by the interfaces, namely the S-Au bond. To go beyond the predictions of classical molecular dynamics, it would be interesting to investigate quantum phonon interference effects by comparing the thermal conductance of modified alkane chains.

In conclusion, thermal transport of both OPE3 and ODT is dominated by phonons with negligible contributions from electronic transport channels, in agreement with the Wiedemann-Franz law. Both experimentally and theoretically, in excellent agreement with literature values, we find that the phonon thermal conductance is higher in ODT junctions, compared with OPE3. This for instance can be explained with the greater width of the phonon transmission resonances (Figure 5.12a and c), which implies a higher density of phonon states at the connection point to electrodes in ODT. This result might seem unintuitive with classical arguments, as OPE3 has a significant stiffer backbone compared with ODT. However, at high frequencies, the transmission is limited by the number of open phonon channels in the gold electrodes, which goes to zero above 20 meV. This further demonstrates that the combination of a molecule that transmits better high energy modes with low Debye frequency electrodes like gold, can be followed as a strategy to suppress the thermal conductance of phonons, which is fundamental for thermoelectric applications.

Chapter 6

Conclusions and Outlook

This thesis reports on the development and demonstration of a novel experimental technique to investigate heat transport at the atomic and molecular scale. Before this work, there was no method able to reach these length scales in thermal transport experiments. The technique combines highly sensitive heat flux measurements with break junction methods, to simultaneously measure the thermal and electrical conductance of atomic scale contacts. This was achieved by using MEMS structures with an integrated microheater/temperature sensor as suspended substrates for performing break junction experiments in a high-vacuum scanning tunneling microscope. Thanks to the high thermal resistance of the MEMS sensors, the low noise laboratory environment and instrumentation, we obtained state-of-the-art sensitivities of 15 pW/K in a bandwidth of 50 Hz at a temperature difference of 50 K around room temperature.

With this technique, we investigated the heat transport properties of atomic gold contacts (Figure 4.3). For the first time, we observed thermal conductance quantization at room temperature and demonstrated the validity of the Wiedemann-Franz law in single atom contacts. Within the uncertainties of the experiment, we could conclude that ballistic phonon transport in these systems contribute with less than 10% to the overall thermal conductance. We further confirmed these results by investigating platinum quantum point contacts and gold atomic junctions formed with Pt and Pt-Ir tips. Good agreement with the Wiedemann-Franz law was also found for gold-gold junctions in the presence of small organic molecules. These results suggest that heat transport in highly transmitting contacts is dominated by electrons and that phonons plat only a minor role.

The experimental technique was then further optimized and developed to characterize the thermal conductance of single molecular junctions. To do this, we solved several experimental challenges connected to the cleaning of the MEMS sensors, deposition of the molecules from solutions and mechanical stability of the tip-MEMS contact. We measured thermal transport across two model systems dithiol-oligo(phenylene ethynylene) (OPE3) and octane-dithiol (ODT), finding very good agreement with our theoretical simulations based on the Green's Function scattering method and the predicted and measured literature values (Figure 5.13). In the case of ODT, our result fitted well with the thermal transport measurements performed on alkane chains of similar lengths, molecular dynamics and ab-initio simulations, suggesting that transport in this system is mostly dominated by the interface thermal resistance with the electrodes. The measurements were reproduced several times on two samples for each molecule and in different experimental conditions (e.g. while closing or opening the junction), confirming the excellent accuracy of the method.

These studies demonstrate that the experimental technique developed is suitable to investigate heat transport across molecules with different chemical backbones, therefore opening the door to systematic studies of the structure-property relationship. In fact, depositing molecules from solution will allow us to apply the measurement technique to different classes of molecules, exploring the many theoretical predictions that have been already put forward. This represents a fundamental step to engineer phonon transport in these nanoscale systems.

6.1 Outlook

Personally, I think it is a wonderful time to think about future experiments, as the technique described in this work opens to so many directions that it is hard to focus on one. From the experimental point of view, my colleagues have been already developing a new setup to perform heat transport measurements at cryogenic temperatures. This will improve the atomic and molecular junction mechanical stability and hopefully provide further insights into the phonon dynamics. Varying the temperature in heat transport measurements corresponds to electrically gate the system under study and to play with the carrier population. Especially, at intermediate temperature ranges, larger deviations from predictions could arise because the assumptions in the transport models might break down in the transition regimes. A temperature dependent measurement of the thermal conductance of a molecular junction would indeed prove or disprove the validity of the harmonic approximation in the ab-initio simulation of these systems.

A next interesting feature to implement in the setup, is the simultaneous measurement of the Seebeck coefficient of molecular junctions. This is in principle only a matter of programming a new measurement routine, as it is intrinsic to the technique to apply a temperature difference and measure the electrical current simultaneously. Measuring the Seebeck coefficient, thermal and electrical conductance would allow to extract the thermoelectric energy conversion efficiency figure of merit ZT for a single molecule.

Enhancements of the thermal sensitivity to obtain the molecular conductance already from single traces could be achieved by employing AC modulation schemes of the MEMS or tip temperature. Further insights into the breaking dynamics of the molecular junction and interaction with the thermal background could be obtained by combining the technique with conductive atomic force microscopy, but it would require a dramatic change of the setup.

In terms of interesting molecular systems, one might start from the investigation of quantum interference phenomena to find new ways to engineer phonon transport and reduce or enhance thermal conduction. Another very interesting but also challenging direction would be studying systems that undergo structural changes by applying an external stimulus (voltage pulse, UV light, etc.) to obtain a demonstration of tunable thermal conductance, which can have a large number of applications.

Finally, one might envision to combine thermal transport measurements at a single molecule level, with optical pumping-probe methods, or in general optical techniques, to obtain information about the dynamics of the heat transfer process or about spectroscopic features (e.g. Raman spectra) of the molecular junctions.

Appendix A

Power dissipation and temperature distribution along the supporting beams

---

In this section, the temperature distribution along the supporting beam of the MEMS is calculated from the one dimensional heat diffusion equation to obtain the fraction of dissipated power contributing to the temperature rise of the central platform.

Because of the typical size of the SiNx beam (4 µm × 0.15 µm × 260 µm), we can consider heat transport along the beam length as one dimensional. The Joule heat generated in a segment of volume $dV = A_{Pt}dx$ of a Pt-line by a current I by can be expressed as

$$\dot{Q}_G = \rho_{el} I^2 dx / A_{Pt} \tag{A.1}$$

where ρ_{el} is the electrical resistivity of platinum. If we neglect the contribution of thermal radiation, $\dot{Q}_G$ is equal to the heat conducted by the SiNx beam and the Pt line

$$\dot{Q}_c = -kA \frac{d^2 \Delta T(x)}{dx^2} dx \tag{A.2}$$

with $kA = k_{Pt}A_{Pt} + k_{SiN}A_{SiN}$ being the effective thermal conductivity and cross section of the beam. Combining equations A.1 and A.2 we obtain

$$\frac{d^2 \Delta T(x)}{dx^2} + \frac{RI^2}{kV} = 0 \tag{A.3}$$

where R is the electrical resistance of the Pt line with length L and $kV = kAL$. If we define $x = 0$ as the substrate and $x = L$ as the connection point with the MEMS platform, we can write the boundary conditions (neglecting the spreading the resistance which is expected to be small)

$$\Delta T(0) = 0 \quad \text{and} \quad \Delta T(L) = \Delta T_h \tag{A.4}$$

and solve A.3 as

$$\Delta T(x) = -\frac{RI^2}{2kV} x^2 + \left(\frac{\Delta T_h}{L} + \frac{RI^2}{2kV} L \right) x \tag{A.5}$$

From this we can apply Fourier's law and calculate the heat flow at the MEMS platform

$$\dot{Q} = -kA \left. \frac{d\Delta T(x)}{dx} \right|_{x=L} = \frac{1}{2} R I^2 - G_{th} \Delta T_h \tag{A.6}$$

where the first term corresponds to the Joule heat generation and the second to the heat conduction through the beam with a total thermal conductance of G_{th}. This demonstrates that only half of the power dissipated in the metal lines along the beams is contributing to the temperature rise of the MEMS. Note that so far we have assumed that both the effective thermal conductivity and the electrical resistivity of platinum do not depend on temperature and we neglected the contribution of thermal radiation. Deviations from A.6 can be expected at high temperature differences ($\Delta T > 100$ K), out of the normal working regime.

Appendix B

Tip etching with different metals

B.1 Pt and Pt-Ir tips

To etch platinum and platinum-iridium tips, a recipe has been developed referring to the methods proposed by Musselmann et al. [203] and Valencia et al. [204]. Both groups suggest a two-step approach, comprising a coarse etching step using a relatively high AC voltage ($>$ 25 V RMS) followed by a pulsed fine etching step at lower voltage ($<$ 5 V). The first step is intended to form the main cone of the tip with a radius of a few micrometers, whereas the second forms a sharpened cone on top of the main one with an apex diameter of 100 nm.

Figure B.1 shows a schematic of the setup used to fabricate Pt/Pt-Ir tips. A transformer connected to the power socket supplies a RMS voltage of 25 V at 50 Hz to the metal wire and the graphite ($99.99+\%$) counter electrode immersed in a 2M solution of $CaCl_2$, achieving sufficiently high current of around 500 mA. Etching times of about 4 min for platinum and 9 min for platinum-iridium are observed without drop-off. Then, a manual switch placed between the transformer and the counter electrode is used to apply voltage pulses of 2.5 V RMS in intervals of 1 s, achieving apexes with diameters of about 100 nm reproducibly, Figure B.1. The steps of the platinum/platinum-iridium tip etching are listed below:

Back electrode: Graphite rod

Electrolyte: 2M CaCl2 (dihydrate, 99% purity, Sigma Aldrich) in DI water

1. Cut about 1 cm of 0.25mm Pt/Pt-Ir wire and fix it to the tip holder.
2. Lower the wire about 1-2mm into the electrolyte.
3. Apply a 25V AC signal at 50 Hz. The solution will start to bubble around the tip. The coarse etching process takes around 4 min for Pt and 9 min for Pt-Ir.
4. When done, lower the tip further into the solution by 0.5 mm.
5. Set a voltage of 2.5 V RMS and toggle the switch for 1 s. Repeat 4 more times.
6. Rinse the tip in DI water and in an ultrasonic bath for 30 s.
7. Dry the tip with N_2 gun.

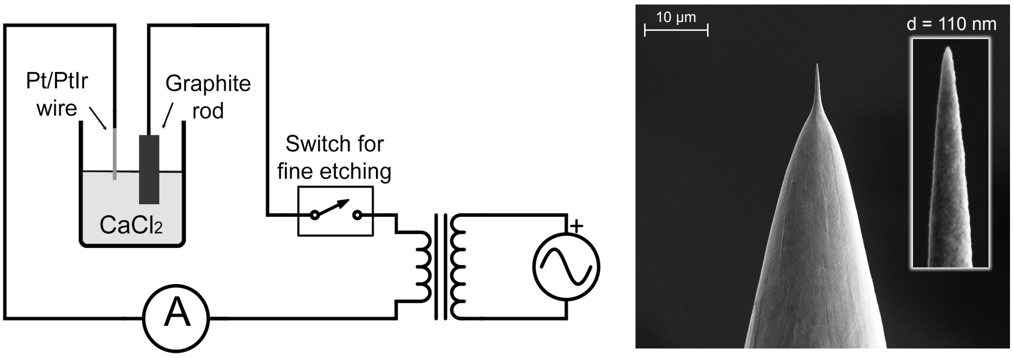

Figure B.1: Schematic of the etching setup to fabricate Pt and Pt-Ir tips (left) and scanning electron micrograph of Pt tip with radius of ∼ 55 nm (right).

B.2 W tips

Tungsten is another very common material used to fabricate sharp tips by electrochemical etching for scanning tunneling microscopy [205, 206]. Among all the recipes available in literature, we adopted the method described by Collins [207], where a wire loop used as a counter electrode is not immersed in solution but contains a thin electrolyte layer, which the tungsten tip can go through. In this way, the etching is localized at the tip area in contact with the solution; the process ends with the drop of the portion below the loop, creating effectively 2 tips. Typically, the tip that falls shows the smallest radius.

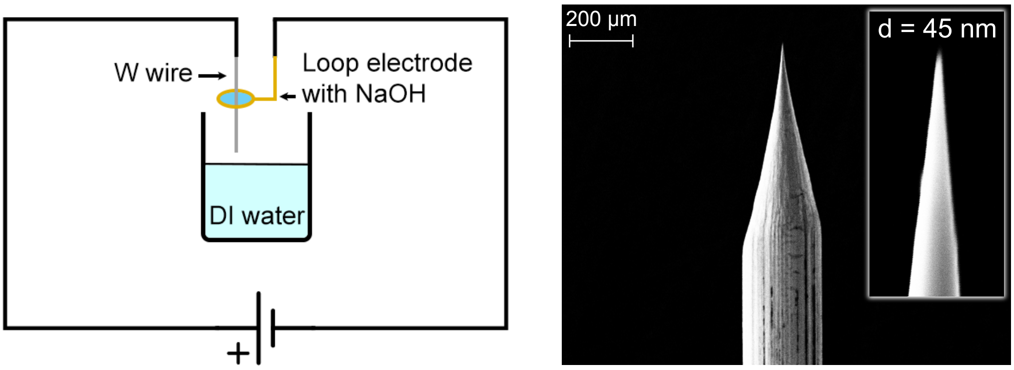

Figure B.2: Schematic of the etching setup to fabricate W tips (left) and scanning electron micrograph of W tip with radius ∼ 22 nm (right).

Figure B.2 shows a schematic of the etching setup. The technique works with both AC and DC voltages yielding a similar apex diameter of around 50-100 nm. The difference between them lies mainly in the etching time and the shape of the resulting tip cone: using AC modulation, the etching is fast and with bubbles (≈ 3 min), forming a conical tip with a large cone angle (Figure B.2), while using a DC voltage, it does not generate bubbles but is rather slow (≈ 12 min), giving tip shapes with high aspect ratio. For the STM-BJ experiments, the AC method is preferable as it provides tips with low aspect ratio, helping the formation of stable junctions.

After the etching, tungsten tips are known to oxidize quickly when exposed to air. There are several known methods to clean the oxide from STM tips, including UHV annealing, chemical treatment using hydrofluoric acid, AC polishing and sputtering [208]. In addition, Vesel et al. also demonstrated a oxide cleaning method on tungsten substrates using H_2 plasma [209]. We obtained the best results by cleaning the etched tips by ion milling (10 min, at 500 mA and 600 V). After this step, break junction experiments on a gold substrate yielded quantization peaks at multiples of the conductance quantum G_0, as expected for Au-Au contacts. The full recipe is described below:

Electrode: Gold loop

Electrolyte: 2M NaOH (97% purity, Sigma Aldrich) in DI water

1. Cut about 1 cm of 0.25 mm tungsten wire and fix it to the tip holder.
2. Dip the gold loop into NaOH to have a thin layer of solution that stays inside the loop.
3. Prepare a beaker of DI water and place it under the loop, to recover the lower tip after drop-off.
4. Lower the wire about halfway through the loop. Make sure not to pop the solution inside the loop, otherwise repeat step 2.
5. Apply 3.5V AC signal at 50 Hz or 3.5V DC signal. The solution will start to bubble around the tip. Wait until the bottom part of the tip falls. The process takes approximately 3 min with AC and 12 min with DC.
6. When done, rinse the dropped portion of the wire in DI water in an ultrasonic bath for 1min, then in isopropanol for another 1min.
7. Dry the tip with N_2 gun.

Bibliography

[1] A. L. Moore and L. Shi, "Emerging challenges and materials for thermal management of electronics," *Materials Today*, vol. 17, no. 4, pp. 163–174, 2014.

[2] E. Pop, "Energy dissipation and transport in nanoscale devices," *Nano Research*, vol. 3, no. 3, pp. 147–169, 2010.

[3] B. Russ, A. Glaudell, J. J. Urban, M. L. Chabinyc, and R. A. Segalman, "Organic thermoelectric materials for energy harvesting and temperature control," *Nature Reviews Materials*, vol. 1, p. 16050, 2016.

[4] T. Meier, F. Menges, P. Nirmalraj, H. Hölscher, H. Riel, and B. Gotsmann, "Length-dependent thermal transport along molecular chains," *Physical Review Letters*, vol. 113, no. 6, pp. 1–5, 2014.

[5] D. Segal, A. Nitzan, and P. Hänggi, "Thermal conductance through molecular wires," *The Journal of Chemical Physics*, vol. 119, no. 13, pp. 6840–6855, 2003.

[6] D. Segal and B. K. Agarwalla, "Vibrational Heat Transport in Molecular Junctions," *Annual Review of Physical Chemistry*, vol. 67, pp. 185–209, may 2016.

[7] M. Famili, I. Grace, H. Sadeghi, and C. J. Lambert, "Suppression of Phonon Transport in Molecular Christmas Trees," *ChemPhysChem*, vol. 18, pp. 1234–1241, feb 2017.

[8] M. D. Losego, M. E. Grady, N. R. Sottos, D. G. Cahill, and P. V. Braun, "Effects of chemical bonding on heat transport across interfaces," *Nature Materials*, vol. 11, no. 6, pp. 502–506, 2012.

[9] S. Majumdar, J. A. Sierra-Suarez, S. N. Schiffres, W. L. Ong, C. F. Higgs, A. J. H. McGaughey, and J. A. Malen, "Vibrational mismatch of metal leads controls thermal conductance of self-assembled monolayer junctions," *Nano Letters*, vol. 15, no. 5, pp. 2985–2991, 2015.

[10] R. Y. Wang, R. A. Segalman, and A. Majumdar, "Room temperature thermal conductance of alkanedithiol self-assembled monolayers," *Applied Physics Letters*, vol. 89, no. 17, pp. 2004–2007, 2006.

[11] J. C. Love, L. a. Estroff, J. K. Kriebel, R. G. Nuzzo, and G. M. Whitesides, *Self-Assembled Monolayers of Thiolates on Metals as a Form of Nanotechnology*, vol. 105. 2005.

[12] T. Markussen, “Phonon interference effects in molecular junctions.,” *The Journal of chemical physics*, vol. 139, no. 24, p. 244101, 2013.

[13] D. Segal and A. Nitzan, “Heat rectification in molecular junctions,” *Journal of Chemical Physics*, vol. 122, p. 194704, 2005.

[14] H. Sadeghi, S. Sangtarash, and C. J. Lambert, “Oligoyne Molecular Junctions for Efficient Room Temperature Thermoelectric Power Generation,” *Nano Letters*, vol. 15, pp. 7467–7472, 2015.

[15] N. Agraït, A. L. Yeyati, J. M. van Ruitenbeek, and J. M. V. Ruitenbeek, “Quantum properties of atomic-sized conductors,” *Physics Reports*, vol. 377, no. 2-3, pp. 81–279, 2003.

[16] A. Jain and A. J. H. Mcgaughey, “Thermal transport by phonons and electrons in aluminum, silver, and gold from first principles,” *Physical Review B*, vol. 93, no. 8, pp. 1–21, 2016.

[17] R. Landauer, “Spatial Variation of Currents and Fields Due to Localized Scatterers in Metallic Conduction,” *IBM Journal of Research and Development*, vol. 1, no. 3, pp. 223–231, 1957.

[18] H. Sadeghi, “Theory of Electron, Phonon and Spin Transport in Nanoscale Quantum Devices,” *Nanotechnology*, vol. 29, no. 37, pp. 1–22, 2018.

[19] C. J. Lambert, “Basic concepts of quantum interference and electron transport in single-molecule electronics,” *Chemical Society Reviews*, vol. 44, no. 4, pp. 875–888, 2015.

[20] B. J. van Wees, H. van Houten, C. W. J. Beenakker, J. G. Williamson, L. P. Kouwenhoven, D. van der Marel, and C. T. Foxon, “Quantized conductance of point contacts in a two-dimensional electron gas,” *Physical Review Letters*, vol. 60, pp. 848–850, feb 1988.

[21] J. Gooth, M. Borg, H. Schmid, V. Schaller, S. Wirths, K. Moselund, M. Luisier, S. Karg, and H. Riel, “Ballistic One-Dimensional InAs Nanowire Cross-Junction Interconnects,” *Nano Letters*, vol. 17, no. 4, pp. 2596–2602, 2017.

[22] L. Olesen, E. Laegsgaard, I. Stensgaard, F. Besenbacher, P. Stoltze, and K. W. Jacobsen, “Quantized conductance in an atom-sized point contact,” *Physical Review Letters*, vol. 72, no. 14, pp. 2251–2254, 1994.

[23] C. J. Muller, J. Krans, T. N. Todorov, and M. A. Reed, “Quantization efFects in the conductance of metallic contacts at room temperature,” *Physical Review B*, vol. 53, no. 3, pp. 1022–1025, 1996.

[24] F. Schwarz and E. Lörtscher, “Break-junctions for investigating transport at the molecular scale,” *Journal of Physics Condensed Matter*, vol. 26, no. 47, 2014.

[25] N. Agraït, R. J.G., and S. Vieira, “Conductance steps and quantization in atomic-size contacts,” *Physical Review B*, vol. 47, no. 18, pp. 12345–12348, 1993.

[26] A. I. Yanson, G. R. Bollinger, H. E. van den Brom, N. Agraït, J. M. van Ruitenbeek, H. E. V. D. Brom, N. Agrait, J. M. van Ruitenbeek, J. M. V. Ruitenbeek, H. E. van den Brom, N. Agraït, and J. M. van Ruitenbeek, “Formation and manipulation of a metallic wire of single gold atoms,” *Nature*, vol. 395, no. 6704, pp. 783–785, 1998.

[27] H. Ohnishi, Y. Kondo, and K. Takayanagi, “Quantized conductance through individual rows of suspended gold atoms,” *Nature*, vol. 395, no. October, pp. 2–5, 1998.

[28] M. Brandbyge, M. R. Sørensen, and K. W. Jacobsen, “Conductance eigenchannels in nanocontacts,” *Physical Review B*, vol. 56, no. 23, pp. 14956–14959, 1997.

[29] E. Scheer, N. Agraıt, J. C. Cuevas, A. L. Yeyati, B. Ludophk, A. Martın-Rodero, G. R. Bollinger, and U. Jan M., van Ruitenbeekk Cristian, “The signature of chemical valence in the electrical conduction through asingle-atom contact,” *Nature*, vol. 394, pp. 154–157, 1998.

[30] S. K. Nielsen, Y. Noat, M. Brandbyge, R. H. M. Smit, K. Hansen, L. Y. Chen, a. I. Yanson, F. Besenbacher, and J. M. van Ruitenbeek, “Conductance of single-atom platinum contacts: Voltage dependence of the conductance histogram,” *Physical Review B*, vol. 67, no. 24, p. 245411, 2003.

[31] J. Carlos Cuevas and E. Scheer, *Molecular Electronics: an Introduction to Theory and Experiment.* World Scientific Publishing Co. Pte. Ltd., 2nd editio ed., 2017.

[32] T. A. Su, M. Neupane, M. L. Steigerwald, L. Venkataraman, and C. Nuckolls, “Chemical principles of single-molecule electronics,” *Nature Reviews Materials*, vol. 1, 2016.

[33] N. J. Tao, “Electron transport in molecular junctions.,” *Nature nanotechnology*, vol. 1, no. 3, pp. 173–181, 2006.

[34] A. Vilan, D. Aswal, and D. Cahen, “Large-Area, Ensemble Molecular Electronics: Motivation and Challenges,” *Chemical Reviews*, vol. 117, no. 5, pp. 4248–4286, 2017.

[35] Q. Lu, K. Liu, H. Zhang, Z. Du, X. Wang, and F. Wang, “From tunneling to hopping: A comprehensive investigation of charge transport mechanism in molecular junctions based on oligo(p-phenylene ethynylene)s,” *ACS Nano*, vol. 3, no. 12, pp. 3861–3868, 2009.

[36] R. Frisenda, S. Tarkuç, E. Galán, M. L. Perrin, R. Eelkema, F. C. Grozema, and H. S. J. van der Zant, “Electrical properties and mechanical stability of anchoring groups for single-molecule electronics,” *Beilstein Journal of Nanotechnology*, vol. 6, no. 1, pp. 1558–1567, 2015.

[37] P. Moreno-García, M. Gulcur, D. Z. Manrique, T. Pope, W. Hong, V. Kaliginedi, C. Huang, A. S. Batsanov, M. R. Bryce, C. Lambert, and T. Wandlowski, "Single-molecule conductance of functionalized oligoynes: Length dependence and junction evolution," *Journal of the American Chemical Society*, vol. 135, no. 33, pp. 12228–12240, 2013.

[38] V. Kaliginedi, P. Moreno-García, H. Valkenier, W. Hong, V. M. García-Suárez, P. Buiter, J. L. Otten, J. C. Hummelen, C. J. Lambert, and T. Wandlowski, "Correlations between molecular structure and single-junction conductance: A case study with oligo(phenylene-ethynylene)-type wires," *Journal of the American Chemical Society*, vol. 134, no. 11, pp. 5262–5275, 2012.

[39] T. Böhler, A. Edtbauer, and E. Scheer, "Conductance of individual C60 molecules measured with controllable gold electrodes," *Physical Review B - Condensed Matter and Materials Physics*, vol. 76, no. 12, pp. 1–5, 2007.

[40] C. Huang, A. Rudnev, W. Hong, and T. Wandlowski, "Break junction under electrochemical gating: testbed for single-molecule electronics," *Chemical Society Reviews*, vol. 44, pp. 889–901, 2015.

[41] P. N. Butcher, "Thermal and electrical transport formalism for electronic microstructures with many terminals," *J. Phys. Condens. Matter*, vol. 2, pp. 4869–4878, 1990.

[42] H. van Houten, L. W. Molenkamp, C. W. J. Beenakker, and C. T. Foxon, "Thermo-Electric Properties of Quantum Point Contacts," *Quantum*, vol. 215, pp. 1–8, 2005.

[43] S. Majumdar, J. A. Malen, and A. J. H. McGaughey, "Cooperative Molecular Behavior Enhances the Thermal Conductance of Binary Self-Assembled Monolayer Junctions," *Nano Letters*, vol. 17, no. 1, pp. 220–227, 2016.

[44] J. C. Klöckner, R. Siebler, J. C. Cuevas, and F. Pauly, "Thermal conductance and thermoelectric figure of merit of C$_{60}$-based single-molecule junctions: electrons, phonons, and photons," *Physical Review B*, vol. 95, no. 254404, 2017.

[45] Y. Dubi and M. Di Ventra, "Colloquium: Heat flow and thermoelectricity in atomic and molecular junctions," *Reviews of Modern Physics*, vol. 83, no. 1, pp. 131–155, 2011.

[46] J. B. Pendry, "Quantum limits to the flow of information and entropy," *Journal of Physics A: Mathematical and General*, vol. 16, no. October 1982, pp. 2161–2171, 1983.

[47] E. Taylor and D. Segal, "Quantum Bounds on Heat Transport Through Nanojunctions," *Physical Review Letters*, vol. 114, no. 22, pp. 1–5, 2015.

[48] L. G. C. Rego and G. Kirczenow, "Quantized Thermal Conductance of Dielectric Quantum Wires," *Physical Review Letters*, vol. 81, no. 4, p. 232, 1998.

[49] L. G. C. Rego and G. Kirczenow, “Fractional Exclusion Statistics and the Universal Quantum of Thermal Conductance: A Unifying Approach,” *Physical Review B*, vol. 59, no. 20, p. 7, 1999.

[50] K. Schwab, E. A. Henriksen, J. M. Worlock, and M. L. Roukes, “Measurement of the quantum of thermal conductance,” *Nature*, vol. 404, no. 6781, pp. 974–977, 2000.

[51] G. Binnig and H. Rohrer, “Scanning tunneling microscopy,” *Surface Science*, vol. 126, no. 1-3, pp. 236–244, 1983.

[52] A. Aviram and M. A. Ratner, “Molecular Rectifiers,” *Chemical Physics Letters*, vol. 29, no. 277, 1974.

[53] B. Xu and N. J. Tao, “Measurement of Single-Molecule Resistance by Repeated Formation of Molecular Junctions,” *Science (New York, N.Y.)*, vol. 301, no. 5637, pp. 1221–1223, 2003.

[54] S. V. Aradhya and L. Venkataraman, “Single-molecule junctions beyond electronic transport,” *Nature Nanotechnology*, vol. 8, no. 6, p. 399, 2013.

[55] E. Lörtscher, D. Widmer, and B. Gotsmann, “Next-generation nanotechnology laboratories with simultaneous reduction of all relevant disturbances,” *Nanoscale*, vol. 5, no. 21, pp. 10542–10549, 2013.

[56] C. Li, I. Pobelov, T. Wandlowski, A. Bagrets, A. Arnold, and F. Evers, “Charge transport in single Au | alkanedithiol | Au junctions: Coordination geometries and conformational degrees of freedom,” *Journal of the American Chemical Society*, vol. 130, no. 1, pp. 318–326, 2008.

[57] S. Anthony, “http://www.stofficetokyo.ch/switzerland-offers-the-worlds-quietest-room/.”

[58] W. Lee, K. Kim, W. Jeong, L. A. Zotti, F. Pauly, J. C. Cuevas, and P. Reddy, “Heat dissipation in atomic-scale junctions.,” *Nature*, vol. 498, no. 7453, pp. 209–12, 2013.

[59] L. A. Zotti, M. Bürkle, F. Pauly, W. Lee, K. Kim, W. Jeong, Y. Asai, P. Reddy, and J. C. Cuevas, “Heat dissipation and its relation to thermopower in single-molecule junctions,” *New Journal of Physics*, vol. 16, 2014.

[60] M. Tsutsui, T. Kawai, and M. Taniguchi, “Unsymmetrical hot electron heating in quasi-ballistic nanocontacts.,” *Scientific reports*, vol. 2, p. 217, 2012.

[61] Keithley Instruments, *Low Level Measurements Handbook.* 2012.

[62] S. F. Karg, V. Troncale, U. Drechsler, P. Mensch, P. Das Kanungo, H. Schmid, V. Schmidt, L. Gignac, H. Riel, and B. Gotsmann, “Full thermoelectric characterization of InAs nanowires using MEMS heater/sensors.,” *Nanotechnology*, vol. 25, no. 30, p. 305702, 2014.

[63] C. Yu, S. Saha, J. Zhou, L. Shi, A. M. Cassell, B. A. Cruden, Q. Ngo, and J. Li, “Thermal Contact Resistance and Thermal Conductivity of a Carbon Nanofiber,” *Journal of Heat Transfer*, vol. 128, pp. 234–239, sep 2005.

[64] A. I. Boukai, Y. Bunimovich, J. Tahir-Kheli, J.-K. Yu, W. A. Goddard III, and J. R. Heath, “Silicon nanowires as efficient thermoelectric materials,” *Nature*, vol. 451, p. 168, jan 2008.

[65] M. C. Wingert, Z. C. Chen, E. Dechaumphai, J. Moon, J. H. Kim, J. Xiang, and R. Chen, “Thermal conductivity of Ge and Ge-Si core-shell nanowires in the phonon confinement regime,” *Nano Letters*, vol. 11, no. 12, pp. 5507–5513, 2011.

[66] B. Song, A. Fiorino, E. Meyhofer, and P. Reddy, “Near-field radiative thermal transport: From theory to experiment,” *AIP Advances*, vol. 5, no. 5, pp. 0–47, 2015.

[67] G. Mészáros, C. Li, I. Pobelov, and T. Wandlowski, “Current measurements in a wide dynamic range-applications in electrochemical nanotechnology.,” *Nanotechnology*, vol. 18, no. 42, p. 424004, 2007.

[68] R. Frisenda, V. A. Janssen, F. C. Grozema, H. S. Van Der Zant, and N. Renaud, “Mechanically controlled quantum interference in individual π-stacked dimers,” *Nature Chemistry*, vol. 8, no. 12, pp. 1099–1104, 2016.

[69] L. Cui, L. Cui, W. Jeong, S. Hur, M. Matt, J. C. Klöckner, F. Pauly, P. Nielaba, J. C. Cuevas, E. Meyhofer, and P. Reddy, “Quantized thermal transport in single-atom junctions,” *Science (New York, N.Y.)*, 2017.

[70] K. Kloppstech, N. Könne, S. A. Biehs, A. W. Rodriguez, L. Worbes, D. Hellmann, and A. Kittel, “Giant heat transfer in the crossover regime between conduction and radiation,” *Nature Communications*, vol. 8, p. 14475, 2017.

[71] F. Menges, P. Mensch, H. Schmid, H. Riel, A. Stemmer, and B. Gotsmann, “Supplymentary document - Temperature mapping of operating nanoscale devices by scanning probe thermometry,” *Nature Communications*, vol. 7, pp. 1–16, 2016.

[72] J.-P. Bourgoin, G.-G. Allogho, and A. Haché, “Thermal conduction in thin films measured by optical surface thermal lensing,” *Journal of Applied Physics*, vol. 108, p. 073520, oct 2010.

[73] H. Ftouni, C. Blanc, D. Tainoff, A. D. Fefferman, M. Defoort, K. J. Lulla, J. Richard, E. Collin, and O. Bourgeois, “Thermal conductivity of silicon nitride membranes is not sensitive to stress,” *Physical Review B - Condensed Matter and Materials Physics*, vol. 92, no. 12, pp. 1–7, 2015.

[74] W.-h. Chuang, S. Member, T. Luger, R. K. Fettig, R. Ghodssi, and A. T-shape, “Mechanical Property Characterization of LPCVD Silicon Nitride Thin Films at Cryogenic Temperatures,” *Journal of microelectromechanical systems*, vol. 13, no. 5, pp. 870–879, 2004.

[75] S. D. Senturia, *Microsystem design.* Kluwer Academic Publishers, 2001.

[76] A. Somà and A. Ballestra, "Residual stress measurement method in MEMS microbeams using frequency shift data," *Journal of Micromechanics and Microengineering*, vol. 19, no. 9, p. 095023, 2009.

[77] G. Rubio-Bollinger, S. R. Bahn, N. Agraït, K. W. Jacobsen, and S. Vieira, "Mechanical Properties and Formation Mechanisms of a Wire of Single Gold Atoms," *Physical Review Letters*, vol. 87, no. 2, p. 026101, 2001.

[78] B. Song, Y. Ganjeh, S. Sadat, D. Thompson, A. Fiorino, V. Fernández-Hurtado, J. Feist, F. J. Garcia-Vidal, J. C. Cuevas, P. Reddy, and E. Meyhofer, "Enhancement of near-field radiative heat transfer using polar dielectric thin films.," *Nature nanotechnology*, vol. 10, no. February, p. 253, 2015.

[79] O. Elíasson, G. Vasile, S. Ægir Jónsson, G. I. Gudjonsson, M. Arikan, and S. Ingvarsson, "Power regulation and electromigration in platinum microwires," *Review of Scientific Instruments*, vol. 85, no. 11, 2014.

[80] S. Kilgore, *Electromigration in gold interconnects*. PhD thesis, Arizona State University, 2013.

[81] S. Chang, S. Sen, P. Zhang, B. Gyarfas, B. Ashcroft, S. Lefkowitz, H. Peng, and S. Lindsay, "Palladium electrodes for molecular tunnel junctions," *Nanotechnology*, vol. 23, no. 42, 2012.

[82] L. Venkataraman, S. V. Aradhya, M. Frei, A. Physics, A. Mathematics, N. York, U. States, C. Matter, H. Academy, A. Halbritter, and L. Venkataraman, "Correlating structure, conductance, and mechanics of silver atomic-scale contacts," *ACS Nano*, vol. 7, no. 4, pp. 3706–3712, 2013.

[83] T. Kim, H. Vázquez, M. S. Hybertsen, L. Venkataraman, H. Vazquez, M. S. Hybertsen, and L. Venkataraman, "Conductance of molecular junctions formed with silver electrodes," *Nano Letters*, vol. 13, no. 7, pp. 3358–3364, 2013.

[84] R. Vardimon, M. Klionsky, and O. Tal, "Indication of Complete Spin Filtering in Atomic-Scale Nickel Oxide," *Nano Letters*, vol. 15, no. 6, pp. 3894–3898, 2015.

[85] S. K. Lee, T. Ohto, R. Yamada, and H. Tada, "Thermopower of benzenedithiol and C60molecular junctions with Ni and Au Electrodes," *Nano Letters*, vol. 14, no. 9, pp. 5276–5280, 2014.

[86] K. Ullmann, P. B. Coto, S. Leitherer, A. Molina-ontoria, N. Mart, M. Thoss, and H. B. Weber, "Single-Molecule Junctions with Epitaxial Graphene Nanoelectrodes," *Nanoletters*, vol. 15, no. 5, pp. 3512–3518, 2015.

[87] F. Prins, A. Barreiro, J. W. Ruitenberg, J. S. Seldenthuis, N. Aliaga-Alcalde, L. M. K. Vandersypen, and H. S. J. Van Der Zant, "Room-temperature gating of molecular junctions using few-layer graphene nanogap electrodes," *Nano Letters*, vol. 11, no. 11, pp. 4607–4611, 2011.

[88] S. Sadat, E. Meyhofer, and P. Reddy, “Resistance thermometry-based picowatt-resolution heat-flow calorimeter,” *Applied Physics Letters*, vol. 102, no. 16, 2013.

[89] F. Warkusz, “The size effect and the temperature coefficient of resistance in thin films,” *Journal of Physics D: Applied Physics*, vol. 11, no. 5, pp. 689–694, 2001.

[90] G. Fischer, H. Hoffmann, and J. Vancea, “Mean free path and density of conductance electrons in platinum determined by the size effect in extremely thin films,” *Physical Review B*, vol. 22, no. 12, pp. 6065–6073, 1980.

[91] J. Zhang, Y. Nagao, S. Kuwano, and Y. Ito, “Microstructure and temperature coefficient of resistance of platinum films,” *Japanese Journal of Applied Physics, Part 1: Regular Papers and Short Notes and Review Papers*, vol. 36, no. 2, pp. 834–839, 1997.

[92] M. Zeier, J. Hoffmann, and M. Wollensack, “Metas.UncLib - A measurement uncertainty calculator for advanced problems,” *Metrologia*, vol. 49, no. 6, pp. 809–815, 2012.

[93] B. L. Zink and F. Hellman, “Specific heat and thermal conductivity of low-stress amorphous Si-N membranes,” *Solid State Communications*, vol. 129, no. 3, pp. 199–204, 2004.

[94] X. Zhang and C. P. Grigoropoulos, “Thermal conductivity and diffusivity of free-standing silicon nitride thin films,” *Review of Scientific Instruments*, vol. 66, no. 2, pp. 1115–1120, 1995.

[95] R. Sultan, A. D. Avery, G. Stiehl, and B. L. Zink, “Thermal conductivity of micromachined low-stress silicon-nitride beams from 77 to 325 K,” *Journal of Applied Physics*, vol. 105, no. 4, 2009.

[96] F. Völklein, H. Reith, T. W. Cornelius, M. Rauber, and R. Neumann, “The experimental investigation of thermal conductivity and the Wiedemann-Franz law for single metallic nanowires.,” *Nanotechnology*, vol. 20, no. 32, p. 325706, 2009.

[97] J. Stefan, “Über die Beziehung zwischen der Wärmestrahlung und der Temperatur,” 1879.

[98] L. Boltzmann, “Ableitung des Stefan’schen Gesetzes, betreffend die Abhängigkeit der Wärmestrahlung von der Temperatur aus der electromagnetischen Lichttheorie,” *Annalen der Physik*, vol. 258, no. 6, pp. 291–294, 1884.

[99] P. J. Van Zwol, D. F. Vles, W. P. Voorthuijzen, M. Péter, H. Vermeulen, W. J. Van Der Zande, J. M. Sturm, R. W. E. Van De Kruijs, F. Bijkerk, M. P??ter, H. Vermeulen, W. J. Van Der Zande, J. M. Sturm, R. W. E. Van De Kruijs, and F. Bijkerk, “Emissivity of freestanding membranes with thin metal coatings,” *Journal of Applied Physics*, vol. 118, no. 21, pp. 2–6, 2015.

[100] A. H. Sully, E. A. Brandes, and R. B. Waterhouse, “Some measurements of the total emissivity of metals and pure refractory oxides and the variation of emissivity with temperature,” *British Journal of Applied Physics*, vol. 3, no. 3, pp. 97–101, 1952.

[101] L. L. Patera, X. Liu, N. Mosso, S. Decurtins, S. X. Liu, and J. Repp, “Crystallization of a Two-Dimensional Hydrogen-Bonded Molecular Assembly: Evolution of the Local Structure Resolved by Atomic Force Microscopy,” *Angewandte Chemie - International Edition*, vol. 56, no. 36, pp. 10786–10790, 2017.

[102] L. Gross, F. Mohn, N. Moll, P. Liljeroth, and G. Meyer, “The Chemical Structure of a Molecule Resolved by Atomic Force Microscopy,” *Science (New York, N.Y.)*, vol. 325, no. August, pp. 1110–1113, 2009.

[103] E. Lo, E. Lörtscher, B. Gotsmann, Y. Lee, L. Yu, C. Rettner, and H. Riel, “Transport Properties of a Single-Molecule Diode,” *ACS Nano*, vol. 6, no. 6, pp. 4931–4939, 2012.

[104] K. Luka-Guth, S. Hambsch, A. Bloch, P. Ehrenreich, B. M. Briechle, F. Kilibarda, T. Sendler, D. Sysoiev, T. Huhn, A. Erbe, and E. Scheer, “Role of solvents in the electronic transport properties of single-molecule junctions,” *Beilstein Journal of Nanotechnology*, vol. 7, no. 1, pp. 1055–1067, 2016.

[105] T. Kim, P. Darancet, J. R. Widawsky, M. Kotiuga, S. Y. Quek, J. B. Neaton, and L. Venkataraman, “Determination of energy level alignment and coupling strength in 4,4’-bipyridine single-molecule junctions,” *Nano Letters*, vol. 14, no. 2, pp. 794–798, 2014.

[106] M. T. González, E. Leary, R. García, P. Verma, M. A. Herranz, G. Rubio-Bollinger, N. Martín, and N. Agraït, “Break-junction experiments on acetyl-protected conjugated dithiols under different environmental conditions,” *Journal of Physical Chemistry C*, vol. 115, no. 36, pp. 17973–17978, 2011.

[107] M. H. Dishner, M. M. Ivey, S. Gorer, J. C. Hemminger, and F. J. Feher, “Preparation of gold thin films by epitaxial growth on mica and the effect of flame annealing,” *Journal of Vacuum Science & Technology A: Vacuum, Surfaces, and Films*, vol. 16, no. 6, pp. 3295–3300, 1998.

[108] C. G. Worley, “Removing sulfur from gold using ultraviolet/ozone cleaning,” *Journal of Vacuum Science & Technology A: Vacuum, Surfaces, and Films*, vol. 13, no. January, p. 2281, 1995.

[109] D. E. King, “Oxidation of Gold By Ultraviolet-Light and Ozone At 25-Degrees-C,” *J. Vac. Sci. Technol. A*, vol. 13, no. 3, pp. 1247–1253, 1995.

[110] E. Hesse and J. A. Creighton, “Investigation by surface-enhanced Raman spectroscopy of the effect of oxygen and hydrogen plasmas on adsorbate-covered gold and silver island films,” *Langmuir*, vol. 15, no. 10, pp. 3545–3550, 1999.

[111] K. Raiber, A. Terfort, C. Benndorf, N. Krings, and H. H. Strehblow, "Removal of self-assembled monolayers of alkanethiolates on gold by plasma cleaning," *Surface Science*, vol. 595, no. 1-3, pp. 56–63, 2005.

[112] H. Ron, S. Matlis, and I. Rubinstein, "Self-Assembled Monolayers on Oxidized Metals . 2 . Gold Surface Oxidative Pretreatment , Monolayer Properties , and Depression Formation," *Langmuir*, vol. 7463, no. 14, pp. 1116–1121, 1998.

[113] W. M. Van Spengen, R. Puers, and I. De Wolf, "On the physics of stiction and its impact on the reliability of microstructures," *Journal of Adhesion Science and Technology*, vol. 17, no. 4, pp. 563–582, 2003.

[114] N. Tas, T. Sonnenberg, H. Jansen, R. Legtenberg, and M. Elwenspoek, "Stiction in surface micromachining," *Journal of Micromechanics and Microengineering*, vol. 6, no. 4, pp. 385–397, 1996.

[115] C. Vericat, M. E. Vela, G. Benitez, P. Carro, and R. C. Salvarezza, "Self-assembled monolayers of thiols and dithiols on gold: new challenges for a well-known system," *Chemical Society Reviews*, vol. 39, no. 5, p. 1805, 2010.

[116] A. J. Melmed, "The art and science and other aspects of making sharp tips," *Journal of Vacuum Science & Technology B: Microelectronics and Nanometer Structures*, vol. 9, no. 2, p. 601, 1991.

[117] A. J. Nam, A. Teren, T. A. Lusby, and A. J. Melmed, "Benign making of sharp tips for STM and FIM: Pt, Ir, Au, Pd, and Rh," *Journal of Vacuum Science & Technology B: Microelectronics and Nanometer Structures*, vol. 13, no. 4, p. 1556, 1995.

[118] L. Libioulle, "Very sharp gold and platinum tips to modify gold surfaces in scanning tunneling microscopy," *Journal of Vacuum Science & Technology B: Microelectronics and Nanometer Structures*, vol. 13, no. 3, p. 1325, 1995.

[119] B. Ren, G. Picardi, and B. Pettinger, "Preparation of gold tips suitable for tip-enhanced Raman spectroscopy and light emission by electrochemical etching," *Review of Scientific Instruments*, vol. 75, no. 4, pp. 837–841, 2004.

[120] M. G. Boyle, L. Feng, and P. Dawson, "Safe fabrication of sharp gold tips for light emission in scanning tunnelling microscopy," *Ultramicroscopy*, vol. 108, no. July, pp. 558–566, 2008.

[121] R. Franz and G. Wiedemann, "Über die Wärme-Leitungsfähigkeit der Metalle," *Annalen der Physik*, vol. 165, no. 8, pp. 497–531, 1853.

[122] N. Mosso, U. Drechsler, F. Menges, P. Nirmalraj, S. Karg, H. Riel, and B. Gotsmann, "Heat transport through atomic contacts," *Nature Nanotechnology*, vol. 12, no. 5, pp. 430–433, 2017.

[123] M. Tsutsui, T. Morikawa, A. Arima, and M. Taniguchi, "Thermoelectricity in atom-sized junctions at room temperatures," *Scientific Reports*, vol. 3, p. 3326, 2013.

[124] C. Evangeli, M. Matt, L. Rincón-García, F. Pauly, P. Nielaba, G. Rubio-Bollinger, J. C. Cuevas, and N. Agraït, “Quantum thermopower of metallic atomic-size contacts at room temperature,” *Nano Letters*, vol. 15, no. 2, pp. 1006–1011, 2015.

[125] N. W. Ashcroft and N. Mermin, *Solid State Physics.* Saunders College, 1976.

[126] A. Principi and G. Vignale, “Violation of the Wiedemann-Franz Law in Hydrodynamic Electron Liquids,” *Physical Review Letters*, vol. 115, no. 5, pp. 1–5, 2015.

[127] C. Kittel, *Introduction to Solid State Physics.* New York: Wiley, 7th ed., 1976.

[128] Q. G. Zhang, B. Y. Cao, X. Zhang, M. Fujii, and K. Takahashi, “Influence of grain boundary scattering on the electrical and thermal conductivities of polycrystalline gold nanofilms,” *Physical Review B*, vol. 74, no. 13, pp. 1–5, 2006.

[129] Z. Cheng, L. Liu, S. Xu, M. Lu, and X. Wang, “Temperature Dependence of Electrical and Thermal Conduction in Single Silver Nanowire,” *Scientific Reports*, vol. 5, p. 10718, 2015.

[130] A. D. Avery, S. J. Mason, D. Bassett, D. Wesenberg, and B. L. Zink, “Thermal and electrical conductivity of approximately 100-nm permalloy, Ni, Co, Al, and Cu films and examination of the Wiedemann-Franz Law,” *Physical Review B*, vol. 92, no. 214410, pp. 1–10, 2015.

[131] N. Wakeham, A. F. Bangura, X. Xu, J.-F. Mercure, M. Greenblatt, and N. E. Hussey, “Gross violation of the Wiedemann-Franz law in a quasi-one-dimensional conductor.,” *Nature communications*, vol. 2, p. 396, 2011.

[132] C. Blumenstein, J. Schäfer, S. Mietke, S. Meyer, A. Dollinger, M. Lochner, X. Y. Cui, L. Patthey, R. Matzdorf, and R. Claessen, “Atomically controlled quantum chains hosting a Tomonaga–Luttinger liquid,” *Nature Physics*, vol. 7, no. 10, pp. 776–780, 2011.

[133] O. Chiatti, J. T. Nicholls, Y. Y. Proskuryakov, N. Lumpkin, I. Farrer, and D. A. Ritchie, “Quantum thermal conductance of electrons in a one-dimensional wire,” *Physical Review Letters*, vol. 97, no. 5, pp. 11–14, 2006.

[134] L. W. Molenkamp, T. Gravier, H. van Houten, O. J. A. Buijk, and M. A. A. Mabesoone, “Peltier coefficient and thermal conductance of a quantum point contact,” *Physical Review Letters*, vol. 68, no. 25, pp. 3765–3768, 1992.

[135] S. Jezouin, F. D. Parmentier, A. Anthore, U. Gennser, A. Cavanna, Y. Jin, and F. Pierre, “Quantum limit of heat flow across a single electronic channel,” *Science (New York, N.Y.)*, vol. 342, no. 6158, pp. 601–4, 2013.

[136] K. Kim, B. Song, V. Fernández-Hurtado, W. Lee, W. Jeong, L. Cui, D. Thompson, J. Feist, M. T. H. Reid, F. J. García-Vidal, J. C. Cuevas, E. Meyhofer, and P. Reddy, “Radiative heat transfer in the extreme near field,” *Nature*, vol. 528, no. 7582, pp. 387–391, 2015.

[137] A. Kittel, W. Müller-Hirsch, J. Parisi, S. A. Biehs, D. Reddig, and M. Holthaus, "Near-field heat transfer in a scanning thermal microscope," *Physical Review Letters*, vol. 95, no. 22, pp. 1–4, 2005.

[138] L. Cui, W. Jeong, V. Fernández-Hurtado, J. Feist, F. J. García-Vidal, J. C. Cuevas, E. Meyhofer, and P. Reddy, "Study of radiative heat transfer in Ångström- and nanometre-sized gaps," *Nature Communications*, vol. 8, p. 14479, 2017.

[139] D. E. Angelescu, M. C. Cross, and M. L. Roukes, "Heat transport in mesoscopic systems," *Superlattices and Microscrtuctures*, vol. 23, no. 3, 1998.

[140] C. Dames and G. Chen, "Thermoelectrics Handbook," in *Thermoelectrics Handbook*, ch. Thermal Co, 2005.

[141] X. Zhao, J. Li, T. C. Au Yeung, C. H. Kam, Q. H. Chen, and C. Q. Sun, "Phonon transport in atomic chains coupled by thermal contacts: The role of buffer layer," *Journal of Applied Physics*, vol. 107, no. 9, pp. 2–6, 2010.

[142] K. Schwab, J. L. Arlett, J. M. Worlock, and M. L. Roukes, "Thermal conductance through discrete quantum channels," *Physica E: Low-Dimensional Systems and Nanostructures*, vol. 9, no. 1, pp. 60–68, 2001.

[143] M. Dreher, F. Pauly, J. Heurich, J. C. Cuevas, E. Scheer, and P. Nielaba, "Structure and conductance histogram of atomic-sized Au contacts," *Physical Review B*, vol. 72, no. 075435, pp. 1–11, 2005.

[144] S. Datta, *Lessons from Nanoelectronics*, vol. Volume 1. WORLD SCIENTIFIC, nov 2011.

[145] G. Wexler, "The size effect and the non-local Boltzmann transport equation in orifice and disk geometry," *Proceedings of the Physical Society*, vol. 89, p. 927, 1966.

[146] D. Erts, H. Olin, L. Ryen, E. Olsson, and a. Thölén, "Maxwell and Sharvin conductance in gold point contacts investigated using TEM-STM," *Physical Review B*, vol. 61, no. 19, pp. 12725–12727, 2000.

[147] J. Torres and J. Sáenz, "Conductance and Mechanical Properties of Atomic-Size Metallic Contacts: A Simple Model.," *Physical review letters*, vol. 77, no. 11, pp. 2245–2248, 1996.

[148] D. Den Boer, M. J. J. Coenen, M. Van Der Maas, T. P. J. Peters, O. I. Shklyarevskii, J. A. A. W. Elemans, A. E. Rowan, and S. Speller, "Electron transport through CO studied by gold break-junctions in nonpolar liquids," *Journal of Physical Chemistry C*, vol. 113, no. 34, pp. 15412–15416, 2009.

[149] Z. Balogh, P. Makk, and A. Halbritter, "Alternative types of molecule-decorated atomic chains in Au-CO-Au single-molecule junctions.," *Beilstein journal of nanotechnology*, vol. 6, no. 1, pp. 1369–76, 2015.

[150] M. Kiguchi, D. Djukic, and J. M. van Ruitenbeek, "The effect of bonding of a CO molecule on the conductance of atomic metal wires.," *Nanotechnology*, vol. 18, no. 3, p. 035205, 2007.

[151] C. D. Bain, T. E. Barry, Y.-T. Tao, J. Evall, G. M. Whitesides, and R. G. Nuzzo, "Formation of Monolayer Films by the Spontaneous Assembly of Organic Thiols from Solution onto Gold," *Journal of the American Chemical Society*, vol. 111, pp. 321–335, 1989.

[152] V. Balachandran, R. Bosisio, and G. Benenti, "Validity of the Wiedemann-Franz law in small molecular wires," *Physical Review B*, vol. 86, no. 3, 2012.

[153] L. Cui, R. Miao, C. Jiang, E. Meyhofer, and P. Reddy, "Perspective: Thermal and thermoelectric transport in molecular junctions," *The Journal of Chemical Physics*, vol. 146, no. 9, p. 092201, 2017.

[154] M. Gotoh, K. D. Hill, and E. G. Murdock, "A gold / platinum thermocouple reference table," *Review of Scientific Instruments*, vol. 62, no. 11, pp. 2778–2791, 1991.

[155] B. Ludoph and J. M. van Ruitenbeek, "Thermopower of atomic-size metallic contacts," *Physical Review B*, vol. 59, no. 19, pp. 12290–12293, 1999.

[156] B. Ludoph, M. H. Devoret, D. Esteve, C. Urbina, and J. M. Ruitenbeek, "Evidence for saturation of channel transmission from conductance fluctuations in atomic-size point contacts," *Physical Review Letters*, vol. 82, no. 7, pp. 1530–1533, 1999.

[157] R. H. M. Smit, Y. Noat, C. Untiedt, N. D. Lang, M. C. van Hemert, and J. M. van Ruitenbeek, "Measurement of the conductance of a hydrogen molecule," *Nature*, vol. 419, no. 6910, pp. 906–909, 2002.

[158] R. H. Smit, C. Untiedt, A. I. Yanson, and J. M. Van Ruitenbeek, "Common origin for surface reconstruction and the formation of chains of metal atoms," *Physical Review Letters*, vol. 87, no. 26, pp. 266102–1–266102–4, 2001.

[159] P. Makk, Z. Balogh, S. Csonka, and A. Halbritter, "Pulling platinum atomic chains by carbon monoxide molecules," *Nanoscale*, vol. 4, no. 15, pp. 4739–4745, 2012.

[160] F. Pauly, M. Dreher, J. K. Viljas, M. Häfner, J. C. Cuevas, and P. Nielaba, "Theoretical analysis of the conductance histograms and structural properties of Ag, Pt, and Ni nanocontacts," *Physical Review B*, vol. 74, no. 23, pp. 1–21, 2006.

[161] F. Prins, T. Hayashi, B. J. A. De Vos Van Steenwijk, B. Gao, E. A. Osorio, K. Muraki, and H. S. J. Van Der Zant, "Roomerature stability of Pt nanogaps formed by self-breaking," *Applied Physics Letters*, vol. 94, no. 12, pp. 2007–2010, 2009.

[162] J. Costa-Krämer, "Conductance quantization at room temperature in magnetic and nonmagnetic metallic nanowires," *Physical Review B - Condensed Matter and Materials Physics*, vol. 55, no. 8, pp. R4875–R4878, 1997.

[163] J. C. Klöckner, M. Matt, P. Nielaba, F. Pauly, and J. C. Cuevas, "Thermal conductance of metallic atomic-size contacts: Phonon transport and Wiedemann-Franz law," *Physical Review B*, vol. 96, no. 20, pp. 1–15, 2017.

[164] C. Y. Ho, R. W. Powell, and P. E. Liley, "Thermal Conductivity of the Elements," 1972.

[165] U. Landman, W. D. Luedtie, N. A. Burnham, and R. J. Colton, "Atomistic Adhesion , Mechanisms and Dynamics of and Fracture," *Science (New York, N.Y.)*, vol. 248, no. 4954, pp. 454–461, 1990.

[166] J. I. Pascual, J. Mendez, J. Gomez-Herrero, A. M. Baro, N. Garcia, U. Landman, E. N. B. W. D. Luedtke, and H.-P. Cheng, "Electrical and mechanical properties of metallic nanowires: Conductance quantization and localization," *Journal of Vacuum Science & Technology B*, vol. 13, no. 3, p. 1280, 1995.

[167] X. S. Zhou, Y. M. Wei, L. Liu, Z. B. Chen, J. Tang, and B. W. Mao, "Extending the capability of STM break junction for conductance measurement of atomic-size nanowires: An electrochemical strategy," *Journal of the American Chemical Society*, vol. 130, no. 40, pp. 13228–13230, 2008.

[168] I. V. Pobelov, K. P. Lauritzen, K. Yoshida, A. Jensen, G. Meszaros, K. W. Jacobsen, M. Strange, T. Wandlowski, and G. C. Solomon, "Dynamic breaking of a single gold bond," *Nature Communications*, vol. 8, no. May, pp. 1–6, 2017.

[169] Z. Huang, B. Xu, Y. Chen, M. Di Ventra, and N. Tao, "Measurement of current-induced local heating in a single molecule junction," *Nano Letters*, vol. 6, no. 6, pp. 1240–1244, 2006.

[170] E. Evans, "Probing the relation between Force-Lifetime-and Chemistry in Single Molecular Bonds," *Annual Review of Biophysics and Biomolecular Structure*, vol. 30, pp. 105–128, 2001.

[171] "The PGM database."

[172] L. Hu, L. Zhang, M. Hu, J. S. Wang, B. Li, and P. Keblinski, "Phonon interference at self-assembled monolayer interfaces: Molecular dynamics simulations," *Physical Review B*, vol. 81, no. 235427, pp. 1–5, 2010.

[173] J. C. Klöckner, J. C. Cuevas, and F. Pauly, "Tuning the thermal conductance of molecular junctions with interference effects," *Physical Review B*, vol. 96, no. 24, pp. 1–10, 2017.

[174] J. C. Duda, C. B. Saltonstall, P. M. Norris, and P. E. Hopkins, "Assessment and prediction of thermal transport at solid-self-assembled monolayer junctions," *Journal of Chemical Physics*, vol. 134, p. 094704, 2011.

[175] S. Wu, M. T. González, R. Huber, S. Grunder, M. Mayor, C. Schönenberger, and M. Calame, "Molecular junctions based on aromatic coupling.," *Nature nanotechnology*, vol. 3, no. 9, pp. 569–74, 2008.

[176] M. Lemmer, M. S. Inkpen, K. Kornysheva, N. J. Long, and T. Albrecht, "Unsupervised vector-based classification of single-molecule charge transport data," *Nature Communications*, vol. 7, no. 12922, 2016.

[177] M. T. González, S. Wu, R. Huber, S. J. Van Der Molen, C. Schönenberger, and M. Calame, "Electrical conductance of molecular junctions by a robust statistical analysis," *Nano Letters*, vol. 6, no. 10, pp. 2238–2242, 2006.

[178] S. Y. Jang, P. Reddy, A. Majumdar, and R. A. Segalman, "Interpretation of stochastic events in single molecule conductance measurements," *Nano Letters*, vol. 6, no. 10, pp. 2362–2367, 2006.

[179] A. Magyarkuti, K. P. Lauritzen, Z. Balogh, A. Nyáry, G. Mészáros, P. Makk, G. C. Solomon, and A. Halbritter, "Temporal correlations and structural memory effects in break junction measurements," *Journal of Chemical Physics*, vol. 146, no. 9, 2017.

[180] R. Huber, M. T. Gonzalez, S. Wu, M. Langer, S. Grunder, V. Horhoiu, M. Mayor, M. R. Bryce, C. S. Wang, R. Jitchati, C. Schonenberger, and M. Calame, "Electrical conductance of conjugated oligorners at the single molecule level," *Journal of the American Chemical Society*, vol. 130, no. 3, pp. 1080–1084, 2008.

[181] K. Yoshida, I. V. Pobelov, D. Z. Manrique, T. Pope, G. Mészáros, M. Gulcur, M. R. Bryce, C. J. Lambert, and T. Wandlowski, "Correlation of breaking forces, conductances and geometries of molecular junctions," *Scientific Reports*, vol. 5, pp. 1–8, 2015.

[182] K. Wang, J. M. Hamill, J. Zhou, and B. Xu, "Mapping the details of contact effect of modulated Au-octanedithiol-Au break junction by force-conductance cross-correlation," *Journal of the American Chemical Society*, vol. 136, no. 50, pp. 17406–17409, 2014.

[183] W. Haiss, S. Martín, E. Leary, H. van Zalinge, S. J. Higgins, L. Bouffier, and R. J. Nichols, "Impact of Junction Formation Method and Surface Roughness on Single Molecule Conductance," *The Journal of Physical Chemistry C*, vol. 113, no. 14, pp. 5823–5833, 2009.

[184] M. Suzuki, S. Fujii, and M. Fujihira, "Measurements of currents through single molecules of alkanedithiols by repeated formation of break junction in scanning tunneling microscopy under ultrahigh vacuum," *Japanese Journal of Applied Physics*, vol. 45, no. 3 B, pp. 2041–2044, 2006.

[185] X. Li, J. He, J. Hihath, B. Xu, S. M. Lindsay, and N. Tao, "Conductance of single alkanedithiols: Conduction mechanism and effect of molecule-electrode contacts," *Journal of the American Chemical Society*, vol. 128, no. 6, pp. 2135–2141, 2006.

[186] W. Haiss, R. J. Nichols, H. van Zalinge, S. J. Higgins, D. Bethell, and D. Schiffrin, "Measurement of single molecule conductivity using the spntaneous formation of molecular wires," *Phys. Chem. Chem. Phys.*, vol. 6, pp. 4330–4337, 2004.

[187] W. Haiss, C. Wang, I. Grace, A. S. Batsanov, D. J. Schiffrin, S. J. Higgins, M. R. Bryce, C. J. Lambert, and R. J. Nichols, “Precision control of single-molecule electrical junctions,” *Nature Materials*, vol. 5, no. 12, pp. 995–1002, 2006.

[188] J. M. Tourr, J. I. LeRoy, D. L. Pearson, J. S. L. Jaydeep, P. T. Burgin, G. M. Whitesides, D. L. Allara, A. N. Parikh, and S. V. Atrer, “Self-Assembled Monolayers and Multilayers of Conjugated Thiols, α,ω-Dithiols, and Thioacetyl-Containing Adsorbates- Understanding Attachments between Potential Molecular Wires and Gold Surface,” *Journal of the American Chemical Society*, vol. 117, no. 3, pp. 9529–9534, 1995.

[189] H. Valkenier, E. H. Huisman, P. A. Van Hal, D. M. De Leeuw, R. C. Chiechi, and J. C. Hummelen, “Formation of high-quality self-assembled monolayers of conjugated dithiols on gold: Base matters,” *Journal of the American Chemical Society*, vol. 133, no. 13, pp. 4930–4939, 2011.

[190] A. Dhar, “Heat Transport in low-dimensional systems,” *Advances in Physics*, vol. 57, no. 5, pp. 457–537, 2008.

[191] S. Lepri, R. Livi, and A. Politi, “Thermal conduction in classical low-dimensional lattices,” *Physics Reports*, vol. 377, no. 1, pp. 1–80, 2003.

[192] A. Pecchia, G. Romano, and A. Di Carlo, “Theory of heat dissipation in molecular electronics,” *Physical Review B - Condensed Matter and Materials Physics*, vol. 75, no. 3, pp. 14–17, 2007.

[193] M. Galperin, M. A. Ratner, and A. Nitzan, “Molecular transport junctions: vibrational effects,” *J. Phys.:Condens. Matter*, vol. 19, no. 10, p. 103201, 2007.

[194] Z. Ge, D. G. Cahill, and P. V. Braun, “Thermal conductance of hydrophilic and hydrophobic interfaces,” *Physical Review Letters*, vol. 96, no. 18, pp. 1–4, 2006.

[195] T. Luo and J. R. Lloyd, “Equilibrium Molecular Dynamics Study of Lattice Thermal Conductivity/Conductance of Au-SAM-Au Junctions,” *Journal of Heat Transfer*, vol. 132, pp. 32401–32410, dec 2009.

[196] T. Luo and J. R. Lloyd, “Non-equilibrium molecular dynamics study of thermal energy transport in Au–SAM–Au junctions,” *International Journal of Heat and Mass Transfer*, vol. 53, pp. 1–11, jan 2010.

[197] Q. Li, M. Strange, I. Duchemin, D. Donadio, and G. C. Solomon, “A Strategy to Suppress Phonon Transport in Molecular Junctions Using π-Stacked Systems,” *Journal of Physical Chemistry C*, vol. 121, no. 13, pp. 7175–7182, 2017.

[198] J. C. Klöckner, M. Bürkle, J. C. Cuevas, and F. Pauly, “Length dependence of the thermal conductance of alkane-based single-molecule junctions: An ab initio study,” *Physical Review B*, vol. 94, no. 20, pp. 1–8, 2016.

[199] M. Galperin, A. Nitzan, and M. A. Ratner, “Heat conduction in molecular transport junctions,” *Physical Review B -*, vol. 75, no. 15, pp. 1–14, 2007.

[200] M. Bürkle, T. J. Hellmuth, F. Pauly, and Y. Asai, "First-principles calculation of the thermoelectric figure of merit for [2,2]paracyclophane-based single-molecule junctions," *Physical Review B*, vol. 91, no. 16, pp. 1–8, 2015.

[201] J. Ferrer, C. J. Lambert, V. M. García-Suárez, D. Z. Manrique, D. Visontai, L. Oroszlany, R. Rodríguez-Ferradás, I. Grace, S. W. Bailey, K. Gillemot, H. Sadeghi, and L. A. Algharagholy, "GOLLUM: A next-generation simulation tool for electron, thermal and spin transport," *New Journal of Physics*, vol. 16, p. 093029, 2014.

[202] Z. Wang, J. A. Carter, A. Lagutchev, K. K. Yee, N. H. Seong, D. G. Cahilll, and D. D. Dlott, "Ultrafast flash thermal conductance of molecular chains," *Science (New York, N.Y.)*, vol. 317, no. 5839, pp. 787–790, 2007.

[203] I. H. Musselman, P. A. Peterson, and P. E. Russell, "Fabrication of tips with controlled geometry for scanning tunnelling microscopy," *Precision Engineering*, vol. 12, no. 1, pp. 3–6, 1990.

[204] V. a. Valencia, A. a. Thaker, J. Derouin, D. N. Valencia, R. G. Farber, D. a. Gebel, and D. R. Killelea, "Preparation of scanning tunneling microscopy tips using pulsed alternating current etching," *Journal of Vacuum Science & Technology A: Vacuum, Surfaces, and Films*, vol. 33, no. 2, p. 023001, 2015.

[205] Y. Nakamura, Y. Mera, and K. Maeda, "A reproducible method to fabricate atomically sharp tips for scanning tunneling microscopy," *Review of Scientific Instruments*, vol. 70, no. 8, pp. 3373–3376, 1999.

[206] A. I. Oliva, A. Romero G., J. L. Peña, E. Anguiano, and M. Aguilar, "Electrochemical preparation of tungsten tips for a scanning tunneling microscope," *Review of Scientific Instruments*, vol. 67, no. 5, pp. 1917–1921, 1996.

[207] Andrew Collins, *Nanotechnology CookBook: practical, reliable and jargon-free experimental procedures.* Elsevier Science, 2012.

[208] I. Ekvall, E. Wahlstrom, D. Claesson, H. Olin, and E. Olsson, "Preparation and Characterization of electrochemically etching W tips for STM," *Meas. Sci. Technol*, vol. 10, p. 11, 1999.

[209] A. Vesel, A. Drenik, R. Zaplotnik, M. Mozetic, and M. Balat-Pichelin, "Reduction of thin oxide films on tungsten substrate with highly reactive cold hydrogen plasma," *Surface and Interface Analysis*, vol. 42, no. 6-7, pp. 1168–1171, 2010.

Author Contributions

Here, I would like to point out the main contributors to this work. A special thanks goes to Dr. Bernd Gotsmann for his continuous support and supervision throughout the PhD project and contributed in many ways to the different aspects of the experimental work.

Section 3.2.2 The MEMS samples were fabricated by Ute Drechsler.

Section 4.3 The measurements with different tip materials on gold were performed by Alissa Prasmusinto during her master thesis project.

Section 5.5 Andrea Gemma supported me by reproducing the measurements of thermal transport across ODT junctions.

Section 5.5 The ab-initio simulations of thermal transport across the molecular junctions were performed by our collaborators at Lancaster University: Dr. Hatef Sadeghi, Dr. Sara Sangtarash and Prof. Colin Lambert.

Section B The recipes for preparing Pt, Pt-Ir and W tips by electrochemical etching were developed by Alissa Prasmusinto during her master thesis project.

Acknowledgments

First of all, I would like to thank all the people who helped and assisted me during these fantastic years of PhD at IBM Research in Zürich. Without their generous contribution and continuous support, it would not have been possible to achieve these results. A special thanks goes to my supervisor at IBM Research, Dr. Bernd Gotsmann: it has been a great pleasure for me to do my PhD under his constant supervision and guidance and I feel I could not have done a better choice both from the personal and the career point of view. My sincere thanks go to Prof. Jascha Repp for supervising my thesis and having hosted me in his group and Prof. Cristoph Strunk for his willingness to co-referee this work. Among all the people that shared this experience with me I would like to thank:

- The ”thermal group” with all its members over the time spent at IBM, for the stimulating scientific discussions, the collaborations and the personal experience shared together. Thank to Andrea Gemma, Alyssa Prasmusinto, Fabian Koenemann, Fabian Menges, Johannes Gooth, Elisabetta Corti, Siegfried Karg, Morten Vollmann and Yannick Zemp.
- The MIND group for the discussions, collaborations and all the coffee and lunch breaks and after work activities spent together. A special thanks to my manager Kirsten Moselund for her constant support and availability.
- Ute Drechsler for her tireless efforts in fabricating perfect devices that made possible this experimental work and all the BRNC team for their kindness and support.
- Walter Riess and Heike Riel for their managerial support and constant willingness in helping young PhD students
- The Predoc community at IBM for all the activities, discussions and laughters shared in these years
- All the people in the Science and Technology Department for their contribution in creating such a nice working environment
- The IBM football team, for the tough matches fought together on the pitch, in Tenero and at Lili’s place

- The MOLESCO group of PhD students and experienced researchers for all the collaborations and after work experiences spent together at the ITN meetings. In particular, I would like to thank Valentina Sacchetti, Joseph Hamil and Kevin Weiland.
- Peter Nirmalraj and Giorgio Signorello for their help and support during the first years of the PhD project

I would like to thank all my friends in Zurich, Italy and around the world for having shared with me a piece of their lives. The warmest thanks go to my family for having allowed me to seize this wonderful opportunity and for their constant presence. Grazie mamma papa' e Luca! Finally, I would like to thank my girlfriend Helena for her patience, love and caring attentions given to me while writing this thesis.